

Fast Response Scintillator Based Detector for MHD Induced Energetic Ion Losses in ASDEX Upgrade

DISSERTATION

der Fakultät für Physik der Ludwig-Maximilians-Universität
München
zur Erlangung des Grades
Doktor der Naturwissenschaften
Dr. rer. nat.

vorgelegt von

Manuel García Muñoz
aus Sevilla, Spanien

München, den 12. Juni 2006

1. Gutachter: Prof. Dr. H. Zohm
2. Gutachter: Prof. Dr. H. Lesch

Tag der mündlichen Prüfung: 31. Juli 2006

Zusammenfassung

In Fusionsplasmen müssen schnelle Teilchen, d.h. durch Heizsysteme erzeugte suprathermische Ionen und α -Teilchen aus Fusionsreaktionen, gut eingeschlossen sein, damit sie ihre Energie ans Plasma abgeben können. Signifikante Verluste dieser Ionen können die Heizeffizienz erheblich erniedrigen und, wenn sie ausreichend stark und lokalisiert sind, auch dem Plasma ausgesetzte Komponenten im Vakuumgefäß beschädigen. Eine genaue Kenntnis der zugrunde liegenden Physik, insbesondere in der Gegenwart von magnetohydrodynamischen (MHD) Instabilitäten, ist von entscheidender Bedeutung, da diese Instabilitäten zu verstärkter Auswärtsdrift schneller Ionen führen können.

Das Ziel dieser Doktorarbeit war sowohl die Entwicklung einer neuen Diagnostik für Untersuchungen von Teilchen-Wellen-Wechselwirkungen im ASDEX Upgrade Tokamak als auch die Interpretation erster Messungen. Dem Aufbau liegen ähnliche Diagnostiken zugrunde, die am TFTR Tokamak und am W7-AS Stellarator betrieben wurden. Der Ionendetektor wirkt wie ein Magnetspektrometer. Er verteilt die schnellen Ionen auf eine Szintillatorfläche, wobei der Auftreffpunkt von Gyroradius (Energie) und Pitchwinkel (Winkel zwischen Ionengeschwindigkeit und Magnetfeldrichtung) abhängt. Das Muster des ausgesendeten Lichtes erlaubt die Identifizierung der Teilchen im Phasenraum mit hoher Zeitauflösung. Die wesentliche Neuheit dieser Diagnostik ist die Verwendung eines Szintillators mit einer Zeitkonstante von weniger als $1 \mu\text{s}$ und einer ebenso raschen Datenerfassung. Damit wird die zeitaufgelöste Untersuchung der Wechselwirkung von MHD-Moden und schnellen Teilchen möglich.

Es wurden Verluste schneller Ionen (Fast Ion Losses: FIL) während verschiedener MHD-Instabilitäten gefunden: FIL aufgrund von Rand-Instabilitäten (Edge Localized Modes: ELMs) wurden direkt beobachtet. Sie zeigen abhängig von der ELM Unterstruktur eine große Vielfalt und ein komplexes Verhalten. Der Einfluß der ELMs auf entweichende schnelle Teilchen ist im ganzen Phasenraum erheblich und unabhängig von ihrem Ursprung. Auch in Gegenwart von Toroidalen Alfvén Eigenmoden (TAEs) in ICRH geheizten Entladungen konnten FIL gemessen werden. Beide Isotope, Wasserstoff und Deuterium, werden in ähnlicher Weise von TAEs beeinflusst. Ein resonanter Prozeß, bei dem TAE- und Präzessionsfrequenz der schnellen Ionen übereinstimmen, konnte mit Hilfe von HAGIS Simulationen als Verlustmechanismus identifiziert werden. Außerdem wurde im Rahmen dieser Doktorarbeit eine neue MHD-Störung durch ihren starken Einfluss auf die suprathermische Deuterium Ionen Population entdeckt. Die Mode ist tief im Plasmainternen lokalisiert und dominiert in ICRH geheizten Entladungen die Verluste schneller Deuterium Ionen aus dem Plasma. Schließlich wurden in Plasmen mit unterschiedlicher Heizung Pulse von schnellen Deuterium Ionen registriert, die von Neoklassischen Tearing Moden ausgeworfen werden. In Plasmen mit reiner Neutralteilchenheizung liegt die Energie dieser Ionen etwa im Bereich der vollen Neutralstrahlenergie. Ihr Pitchwinkel entspricht etwa dem von frei umlaufenden Ionen. Der Vergleich der FIL-Signale mit den Mirnov-Spulen-Signalen ergab, dass diese Verluste auf einem diffusiven Prozess beruhen. Dies wird bestätigt durch Simulationen mit dem ORBIT Code, die zeigen, dass „Orbit Stochastizität“ ein guter Kandidat für den Verlustmechanismus dieser prinzipiell gut eingeschlossenen umlaufenden Ionen ist. Diese Ergebnisse haben das hohe diagnostische Potential der Methode aufgezeigt. Sie eröffnet neue Wege zu einem besseren Verständnis der Physik der schnellen Ionen und kann damit helfen, deren Verhalten in ITER unter dem Einfluss von MHD-Instabilitäten vorauszusagen.

Abstract

In fusion plasma devices, fast particles i.e. suprathermal ions generated by heating systems and fusion born α particles must be well confined, until they have transferred their energy to the plasma bulk. Significant loss of these ions may reduce drastically the heating efficiency and, in addition, may cause damage to plasma facing components in the vacuum vessel, if it is sufficiently intense and localized. A detailed knowledge of the underlying physics in particular in the presence of magnetohydrodynamic (MHD) instabilities is of crucial importance, since these instabilities can lead to an enhancement of the outwards fast ion radial drift.

The development of a new diagnostic for the study of fast particle-wave interactions in the ASDEX Upgrade tokamak as well as the interpretation of the first measurements have been the aim of this thesis. The design is based on similar diagnostics that have been operated in the TFTR tokamak and the W7-AS stellarator. The fast ion loss detector acts as a magnetic spectrometer, dispersing fast ions onto a scintillator, with the strike point depending on their gyroradius (energy) and pitch angle (angle between ion velocity and magnetic field line). The emitted light pattern allows particle identification in the phase space with a high time resolution. The major new development for the diagnostic used on ASDEX Upgrade is the use of a very fast scintillator material that allows sampling rates up to 1 MHz, adequate to study time resolved interactions between MHD modes and fast particles.

Fast Ion Losses (FIL) were found in the presence of different kinds of MHD instabilities: time resolved FIL due to Edge Localized Modes (ELMs) have been directly observed. They show a complex behavior of a great variety, depending on the ELM substructure. The influence of ELMs on escaping fast particles is appreciable in the whole lost particle phase space independent of the fast ion source. FIL could be measured in the presence of Toroidal Alfvén Eigenmodes (TAEs) in ICRH heated discharges. Both species, fast hydrogen and deuterium ions are affected in a similar way by TAEs. A resonant process between the TAE frequency and the precession frequency of the lost ions has been identified by comparisons with HAGIS simulations as the loss mechanism. A new MHD perturbation has been observed for the first time during this thesis by means of its strong influence on the energetic deuterium ion population. The mode is localized deeply in the plasma core and dominates the fluxes of lost fast deuterium ions in ICRH heated discharges. Finally, bursts of fast deuterium ions ejected by Neoclassical Tearing Modes have been detected in discharges with different heating systems. In pure NBI heated discharges, these ions have energies approximately equal to the full NBI injection energy and pitch angles corresponding to ions on passing orbits. A detailed study of the FIL signal together with Mirnov coil signals revealed that the losses are due to a diffusive process. According to this, simulations with the ORBIT code have proven that orbit stochasticity is a good candidate for the mechanism that causes the losses of these, in principle well confined, passing ions. These results revealed the high diagnostic potential of this method, opening new ways towards a better understanding of the fast ion physics and therefore will help to predict the behavior of fast ions in the presence of MHD instabilities for ITER.

Contents

1	Introduction	3
1.1	Thermonuclear Fusion	3
1.2	Tokamaks and the Role of Fast Ions	5
1.3	Motivation	9
1.4	Aim of the Work	12
1.5	Dissertation Outline	13
2	Theoretical Background	14
2.1	Charged Particle Motion in Tokamaks	14
2.1.1	Gyration and Drifts	14
2.1.2	Adiabatic Invariants and Particle Orbits in Tokamaks	18
2.2	MHD Activity in Tokamaks	24
2.2.1	Fishbone Modes	24
2.2.2	Alfvén Instabilities	26
2.2.3	Neoclassical Tearing Modes (NTMs)	29
2.2.4	Edge Localized Modes (ELMs)	30
2.3	Fast Particle Losses due to MHD Activities	31
2.3.1	Mode-Particle Resonance as a Particle Loss Mechanism	31
2.3.2	Orbit Stochasticity	33
3	Experimental Set-Up	35
3.1	The Fast Ion Loss Diagnostic	35
3.2	Detector Head Design	36
3.3	The Choice of the Scintillator	40
3.3.1	Scintillation Basics	42
3.3.2	Characterization of the Scintillator Candidates	43
3.3.3	Results and Conclusions	45
3.4	Light Detection and Data Acquisition System	46

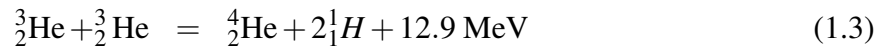
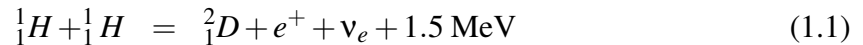
4	Fast Particles in ASDEX Upgrade	49
4.1	Neutral Beam Injection NBI System	49
4.1.1	The NBI scheme in ASDEX Upgrade	49
4.1.2	NBI Fast Particle Population in ASDEX Upgrade.	50
4.2	Electromagnetic Wave Heating	53
4.2.1	Ion Cyclotron Resonance Heating Scheme in ASDEX Upgrade . . .	53
4.2.2	ICRH Fast Particle Population in ASDEX Upgrade	56
5	Experimental Results	57
5.1	Benchmarking of FILD by First Orbit Losses	57
5.2	ELM Induced Fast Ion Losses	59
5.3	NTM Induced Fast Ion Losses	62
5.3.1	(2,1) NTM Induced Fast Ion Losses	63
5.3.2	(3,2) NTM Induced Fast Ion Losses	66
5.4	Fast Ion Losses due to High Frequency MHD Activities	73
5.4.1	Fast Particle Driven MHD Modes; TAEs and Others	73
5.4.2	Beat Waves Driven TAEs	81
6	Discussion	87
6.1	ELM Induced Fast Ion Losses	87
6.2	NTM Induced Fast Ion Losses in NBI Heated H-Modes	88
6.2.1	Fast Ion Loss Rate due to NTMs	89
6.2.2	Numerical Simulations with ORBIT	90
6.2.3	Island Overlap Estimation	96
6.3	TAE and Sierpes Induced Fast Ion Losses	97
6.3.1	Identification of Fast Hydrogen and Deuterium Ion Losses	97
6.3.2	Fast Ion Loss Rate due to TAEs and Sierpes	101
6.3.3	The Sierpes Mode	104
6.3.4	Loss Mechanisms and HAGIS Numerical Simulations	105
7	Summary	112

Chapter 1

Introduction

1.1 Thermonuclear Fusion

Fusion, the way in which the Sun obtains its energy, has the potential of providing an essentially unlimited source of energy. Human beings have been searching a long time for a way to reproduce such a source of energy on Earth. The Sun generates its energy by means of the following reactions [1]:



The cross-section for this whole cycle due to the weak interaction involved in reaction (1.1) is too low to be reproduced on Earth (the Sun overcomes this problem by its huge mass). As a result, the fusion reactions of most practical interest for terrestrial fusion power production are



For the D-T reaction 1.4, the cross section is substantially larger than for the other possible reactions of interest as shown in Fig.1.1. Therefore, a D-T reactor is the promising since a self-sustaining plasma can be reached with the lowest ion temperature ($T > 5 \text{ keV}$)¹ and lowest

¹Following the convention accepted in Fusion, temperatures are written in eV. Thus, in place of conventional kT^0 (where k is Boltzmann's constant and T^0 is in degrees Kelvin) we write $T(\text{eV})$, so that $T^0 = T(\text{joules})/1.381 \cdot 10^{-23}$, where $T(\text{eV}) = T(\text{joules})/1.602 \cdot 10^{-19}$.

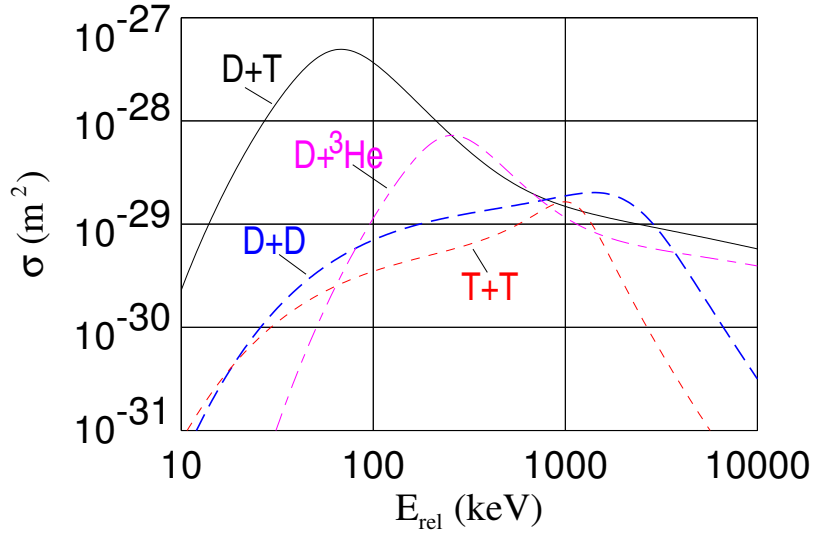


Figure 1.1: Cross-section, σ , of different fusion reactions. The reaction D-T has by far the largest cross-section at relatively low energies.

requirement for the product $n_i \tau_E^* T_i$, where T_i is the ion temperature, n_i the ion density, and τ_E^* the energy confinement time defined by the power balance equation

$$\frac{dW_{tot}}{dt} = P_{heat} - P_{rad} - \frac{W_{tot}}{\tau_E} = P_{heat} - \frac{W_{tot}}{\tau_E^*}. \quad (1.8)$$

Here, W_{tot} is the plasma stored energy, P_{rad} is the power loss due to radiation mainly through bremsstrahlung, P_{heat} is the heating power. τ_E and τ_E^* are different definitions for the energy stored time, the time in which the plasma, due to all losses including radiation (τ_E^*), loses the same amount of energy as it presently contains. In current experiments, radiation loss from bremsstrahlung is typically very small in the power balance and can be ignored, but it will be significant when alpha heating becomes the dominant heating mechanism. For thermal D-T reactions, $\langle \sigma(v)v \rangle \propto T_i^2$ for $9 < T_i < 19 \text{keV}$, and a value of $n_i \tau_E^* T_i > 6 \times 10^{21}$ [2] is required for ignition when the power balance is sustained by fusion reactions. From this condition, it is easy to understand the importance of a long confinement time. The cross-section for the elastic Coulomb scattering is higher than the cross-section for a fusion process by a factor of $\approx 10^4$ at 10 keV and even higher at lower temperatures. This makes the use of cross particle beams not suitable for the generation of fusion energy.

Nowadays, two methods of confinement are investigated in fusion research to reach an ignited plasma.

Inertial confinement High density and short confinement time. A solid pellet is heated by a laser or a heavy ion beam in order to achieve a density of 10^{30}m^{-3} in a volume of a fraction of mm^3 . Thus, for a very short time (μs), a dense hot plasma is produced and confined by its inertia. During this time, fusion can take place. Problems arise due to

the low efficiency of the driver beams and the need for a high symmetric irradiation, asymmetries lead to instabilities during the compression process.

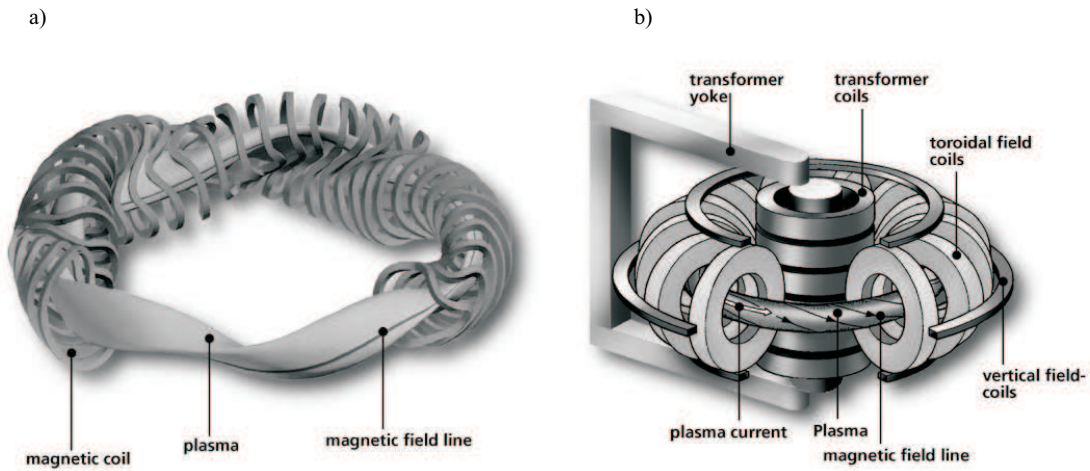


Figure 1.2: Schematic drawing of a tokamak and a stellarator

Magnetic confinement Low density and long confinement time. Since charged particles gyrate around magnetic field lines, a plasma may be confined in a magnetic cage. A typical gyroradius of a deuteron in a magnetic field of $B = 3T$ with an energy of $T = 10\text{keV}$ is $\rho_D \simeq 6.8\text{mm}$. Therefore, the particles are tied to the field lines. There are different magnetic topologies, being stellarators Fig.1.2.a and tokamaks Fig.1.2.b the most common. The one that is most advanced at present is the tokamak configuration.

In present experiments, D is the most common used fuel in order to avoid the T-handling and the large neutron fluxes produced in the reaction(1.4), despite the fact that the cross section in reactions (1.6) and (1.7) is lower by a factor of 10-100 than in the D-T reaction.

It is important to note that to be a candidate for an energy-producing system, the fuel has to be sufficiently abundant. Deuterium, one of the fusion fuel, exists as a fraction of $3.3 \cdot 10^{-5}$ in water. Given the water of the oceans, the static energy range is larger than the time the Sun will continue to burn (a few billion years). The other reactant for fusion, namely tritium, is an unstable radioactive isotope of hydrogen, with a half-life time of 12.3 years. Due to the unstable nature of tritium, a significant amount does not exist in nature. However, tritium can be produced easily by means of nuclear reactions of neutrons generated in D-T reactions with lithium. In this way, the only fusion fuels will be deuterium and lithium. Lithium is also very abundant in the Earth's crust and even in the ocean's water. Table 1.1 summarizes the estimated world energy resources [1].

1.2 Tokamaks and the Role of Fast Ions

As a first attempt to confine particles by magnetic fields, a cylindrical configuration could be taken into account. Because charged particles move freely along field lines, such devices suffer

Present world annual primary energy consumption	$3 \cdot 10^{11}$ gigajoules	Time
Resources		
Coal	10^{14}	300 years
Oil	$1.2 \cdot 10^{13}$	40 years
Natural Gas	$1.4 \cdot 10^{13}$	50 years
^{235}U (fission reactors)	10^{13}	30 years
^{238}U and ^{232}Th (breeder reactors)	10^{16}	30000 years
Lithium (D-T fusion reactors):		
Land	10^{16}	30000 years
Oceans	10^{19}	$3 \cdot 10^7$ years

Table 1.1: Estimated world energy resources. Data are only indicative, being dependent on prices [1].

from end losses. To overcome this problem, the cylinder can be bent into a torus, generally allowing particles to be confined in all directions. A tokamak consists of magnetic field coils wound around the torus poloidally to generate a toroidal field whose radial variation goes like $1/R$ (R stands for the major radius of the tokamak). A transformer coil in the center of the torus induces a current within the plasma, I_{plasma} , that produces a poloidal magnetic field. Its spatial dependence is therefore determined by the current profile. Together, these two magnetic field components bend the field lines into a helical shape, see Fig.1.2.b, that suppresses undesirable particle radial drifts as well as MagnetoHydroDynamic (MHD) instabilities connected with a pure poloidal or a pure toroidal field. The geometry of the magnetic field lines can be described by the safety factor q

$$q = \frac{m}{n} = \frac{\text{number of toroidal circulations}}{\text{number of poloidal circulations}}. \quad (1.9)$$

A $q = 2/1$ magnetic surface has closed field lines after two toroidal and one poloidal circulations. Plasma instabilities, as will be introduced in Chapter 2, usually coincide with this magnetic surfaces of low order of rational q values. The safety factor is used to label the instability. The efficiency of the plasma confinement is represented by a factor called β . β is defined as the ration of plasma pressure over the magnetic field pressure:

$$\beta = \frac{p}{B^2/2\mu_0} \quad (1.10)$$

with B , the main toroidal magnetic field.

Nowadays tokamak plasmas have particle densities of around $10^{19} - 10^{20} m^{-3}$. This is a factor 10^6 lower than in the atmosphere. Impurities in the plasma give rise to radiation losses and also dilute the fuel. Limiting the amount of impurities in the plasma plays a fundamental role in the successful operation of tokamaks. In order to reduce impurities, the plasma has to be separated from the vessel wall. There are two techniques to achieve this, both leading to different plasma

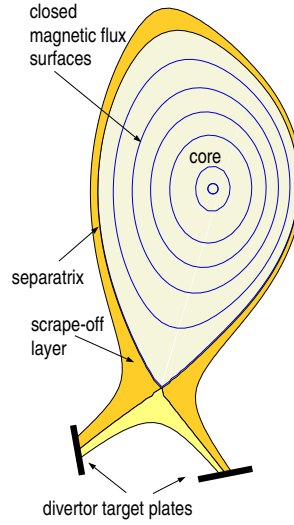


Figure 1.3: Poloidal cross-section of a typical divertor magnetic configuration.

shapes. The first one is to define an outer boundary of the plasma with a material limiter. The second one is to keep the particles away from the vacuum vessel by means of a modification of the magnetic field to produce a magnetic divertor as shown in Fig.1.3. Plasmas in a tokamak are heated to temperatures of a few keV by the ohmic heating created by the plasma current. The required temperatures around 10 keV are then achieved by additional heating systems e.g. neutral beam injection (NBI), ion and electron cyclotron resonance heating (ICRH, ECRH). This basic need of fusion research leads to an increase of the energetic particle population i.e. creation of a non-Maxwellian part of the ion distribution with $E \gg E_{thermal}$. Since the pressure of fast particles will be $\approx 30\%$ (which can already be achieved by heating systems in present experiments), substantial changes in the overall plasma behavior are expected. These changes can be mainly attributed to three different physical properties of fast ions:

- The gyroradius for an energetic particle is larger than that of a thermal particle. For a particle with mass m and charge Ze in a magnetic field B , its gyroradius is given by

$$\rho = \frac{v_{\perp}}{\omega_c} \quad \text{with} \quad \omega_c = \frac{ZeB}{m}. \quad (1.11)$$

As Table 1.2 shows, the gyroradius (Larmor radius) of energetic particles can be an order of magnitude larger than that of a thermal particle. Although a gyroradius of a few centimeters is still small compared to background plasma quantities with length scales of the minor plasma radius (for ITER 2m), it can become equal to the length scales of MHD modes. As a result, new interactions between particles and waves traveling in plasma may lead to new sources of MHD instabilities. Typical trajectories of a thermal particle (5 keV) and an energetic particle (93 keV) in the ASDEX Upgrade tokamak are plotted in Fig.1.4.

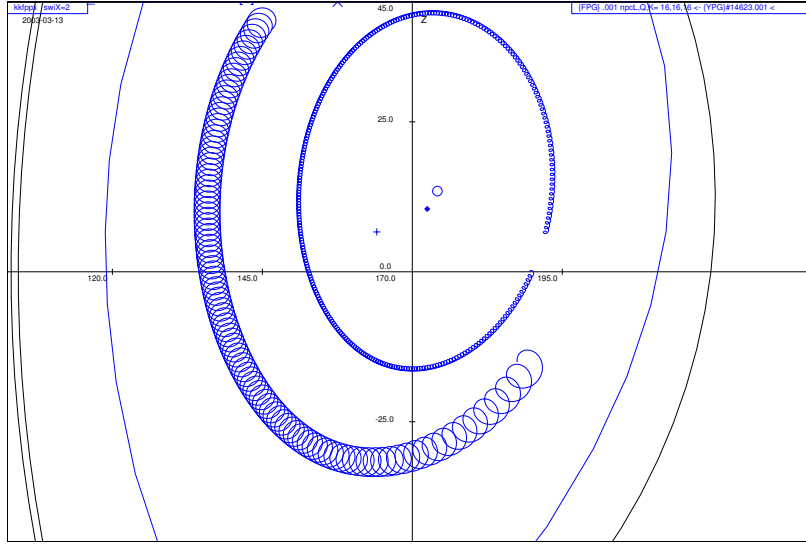


Figure 1.4: Typical orbits of a deuterium ion with 93 keV and 5 keV respectively.

Larmor Radius	Energy				
	1 keV	10 keV	100 keV	500 keV	1000 keV
ρ_e	0.07 mm	0.22 mm	0.71 mm	1.6 mm	2.2 mm
ρ_H	3 mm	9.6 mm	30.4 mm	67.9 mm	96 mm
ρ_D	4 mm	13.6 mm	42.9 mm	96 mm	135.8 mm
ρ_T	5.3 mm	16.6 mm	52.6 mm	117.6 mm	166.3 mm

Table 1.2: Typical Larmor Radius of different particles for $B=1.5T$. Ions have a Larmor radius a few orders of magnitude larger than electrons due to their mass while energetic ions have a gyroradius one order of magnitude larger than thermal ones.

- Compared to the simple cylindrical case, the toroidal curvature breaks the rotational symmetry of the poloidal coordinate and thus adds more intrinsic frequencies to the system, where an effective transfer of energy between plasma waves and particles can occur. In addition to the total kinetic energy of a particle, also the magnetic moment $\mu = mv_{\perp}^2/2B$ is an adiabatic invariant of motion as will be described more in detail in the following chapter. Therefore, v_{\parallel} has to be smaller in regions where B becomes larger according to

$$E = \frac{1}{2}mv_{\parallel}^2 + \mu B = const. \quad (1.12)$$

Consequently, there will be mainly two types of motions: a particle, whose parallel energy is high enough to keep its magnetic moment constant while traveling over the top of the magnetic hill, is called a *passing* or *transit* particle. In contrast, a particle with too low parallel energy compared to its μ cannot cross the magnetic hill and is

therefore trapped in the low B-field region, these are on the so-called *trapped* or *banana* orbits. The bounce/precession frequency for thermal ions is often too low to interact with modes on any of the MHD time scales e.g. Alfvén frequency. Of course, this situation changes when highly energetic particles are present. Furthermore, the particle orbits in a tokamak are also governed by ∇B and curvature drifts, which cause the particle to leave its field line in the poloidal and the radial direction. This leads to radial excursion that can become very large for energetic ions. Additionally, the banana width turns out to be comparable to the spatial dimensions of large-scale MHD modes.

- Finally, differences in the velocity distribution functions are discussed. If the plasma is considered to be in a thermal equilibrium state, the distribution function of the thermal particles in velocity space is assumed to be Maxwellian. But for any kind of fast particle population this is not true anymore. Depending on the source, there can be various forms of energy and pitch angles ($\arccos(v_{\parallel}/v)$) dependencies: for fusion born α -particles the pitch angle is assumed to be isotropic. For fast ions produced by external heating there is no pitch angle isotropy. Each heating scheme possesses its own distribution in the velocity space, see Chapter 4, and thus causes different physical interactions with MHD modes.

1.3 Motivation

The framework connected to fast ion physics is growing in importance during the recent years, becoming a major subject at several fusion plasma devices like ASDEX Upgrade, TFTR, DIII-D or JET. Numerical studies as well as experimental works have shown the importance of a better fast ion confinement for improved plasma performance. In general, the operation of fusion plasma devices is affected by fast ions in different ways [3]:

- Fusion born α -particles as well as externally heated fast ions may be lost right after their birth, which means before they transfer their energy to the plasma bulk through collisions. These so-called prompt losses may deteriorate the efficiency of the heating systems and in some cases even dramatically. They have different lost patterns depending on the fast ion source, being for example for the case of NBI generated fast ions, toroidally as well as poloidally localized [4]. Several works have already observed the deleterious influence of these losses on the heating efficiency at different tokamaks like ASDEX [5], JET [6], DIII-D [7], TFTR [8] or TEXTOR [9].
- If fast ion fluxes encounter the first wall, excessive heat loads and additional impurity sources are generated by sputtering or desorption processes. In discharges with good impurity confinement this may endanger stationary plasma operation as envisaged for fusion reactors. This effect has been studied in detail recently in ASDEX Upgrade by A. Kallenbach et al. [10].
- On the other hand, fast ions can also affect the plasma stability, introducing additional operation limits like the well known β -limit for NTMs or destabilizing for example

Alfvén shear eigenmodes like Toroidal Alfvén Eigenmodes (TAEs). Due to their global structure (low m and n numbers) the equilibrium can be dramatically perturbed with disruptions as a possible consequence [11].

Furthermore, several studies with additional heating systems and α -particles on different Tokamaks have been carried out toward a better understanding of the fast particle loss mechanisms specially related with MHD events. Recently, measurements using different scintillator based detectors for charged particles have revealed a valuable information on the lost ion distribution function in phase space, [12], [13] and [14]. This is the main motivation of the present work since such information together with a well known topology and time dependence of the MHD perturbation should be enough to identify the loss mechanisms.

The general conclusion from previous work is that fast ions and α -particles are classically well confined unless there is large MHD activity in the plasma. Here classical confinement refers to the combined influence of the externally imposed magnetic fields and classical coulomb collisions on fast particle transport, including the effect of the toroidal field ripple. The main exceptions to this good confinement occur during any large scale global MHD perturbation generated by either the background plasma or the fast ion population itself, e.g. tearing modes or toroidal Alfvén eigenmodes (TAEs). A number of fast particle transport mechanisms already observed in different machines [15] are summarized here.

First orbit fast ion loss The simplest mechanism of fast particle loss is first orbit loss, which occurs when fast particles are born on an orbit which becomes immediately lost from the plasma. The theory for first orbit fast ion loss is well known. This kind of losses has been observed in TFTR [16], large at low plasma currents ($> 50\%$) and small at high plasma currents ($< 5\%$).

Coulomb Collisions Classical Coulomb collisions thermalize gradually the fast ions as they heat the plasma. The effect of the collisions with electrons is to produce a friction which results in a velocity decay time. This decay time for Neutral Beam Injected fast ions in ASDEX Upgrade with energies of $93keV$ is $\tau \approx 70ms$ for typical plasma parameters (n and T), [4]. However, the time required to reach thermal energy for fast ions with energies bellow a critical energy is dominated by collisions with thermal ions. They cause additional pitch angle scattering, which changes the fast ion magnetic moment producing extra fast ion losses, mainly by converting passing particles to trapped particles whose orbits intersect the wall.

Toroidal field ripple induced fast ion loss The most common type of deviation from magnetic axisymmetry is due to the TF ripple associated with the finite number of TF coils. In ASDEX Upgrade with 16 TF coils, this produces a maximum TF ripple (i.e. peak to average $\delta B_{tor}/B_{tor}$ along a field line) of $\delta \approx 2\%$ at the outer limiter but more typically $\delta \approx 1\%$ at the plasma edge, see Fig.1.5. This ripple can cause the radial location of the banana tips of trapped particle orbits to become decorrelated above a TF stochastic ripple loss threshold [17].

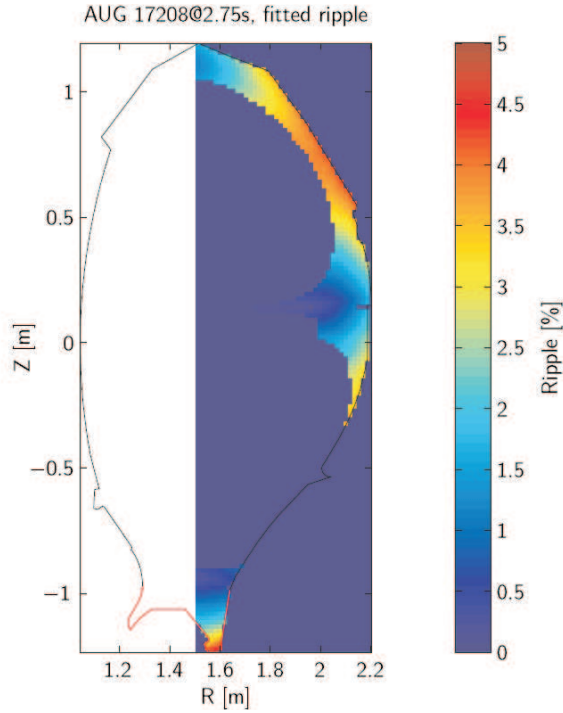


Figure 1.5: Typical toroidal field ripple in ASDEX Upgrade [18].

MHD induced fast ion loss Losses may also be induced by magnetohydrodynamic (MHD) perturbations of various types, such as coherent low m/n (poloidal/toroidal mode number) tearing modes, high- n ballooning modes, sawteeth, disruptions or TAEs. In this section we distinguish between two mechanisms for MHD induced fast ion losses; mode-particle resonance between a characteristic frequency of the particle trajectory and the intrinsic frequency of the coherent MHD perturbation, and orbit stochasticity which occur only above a threshold in the perturbation amplitude being the finite gyroradius the responsible for the additional radial transport.

The strongest mode-particle resonance interaction has been observed in plasmas with fast ion driven instabilities. Experiments with neutral beam injection (NBI) and α -particles on the DIII-D [19] and the TFTR [20] tokamaks in D-T plasmas have shown that under certain conditions Alfvén instabilities can cause a significant loss of those particles. Due to their relatively high phase velocity, $v_A \sim 5 \cdot 10^6 m/s$, Alfvén waves mainly resonate [21] with these energetic particles. Different fast ion loss mechanisms in the presence of high frequency coherent MHD perturbation have been suggested. Sigmar et al. propose a general loss mechanism associated with a change in the parallel velocity of fast ions, mainly α particles, due to a resonant interaction with Alfvén waves through Landau damping [22]. Energetic particles on passing orbits can become resonant by means of their v_{\parallel} with the phase velocity of the waves, transferring parallel kinetic energy to the waves. With the loss of parallel velocity, these initially passing particles can become trapped in the inner leg of their orbit and move onto a large, unconfined

banana orbit. A later study on the DIII-D tokamak [23] with NBI excited TAE modes, coincides with Sigmar in the absence of a threshold amplitude and in the linear scaling of fast ion losses with mode amplitude. Experiments with NBI heated fast ions and α -particles, [24], [25], [26] and [19], on TFTR and on DIII-D have shown that under certain conditions such as Alfvén instabilities may cause significant losses even damaging the vessel walls. Energetic particles on trapped orbits can also become resonant through their bounce and/or precession frequency with low frequency MHD perturbations. This resonant loss mechanism was studied for the first time on the PDX tokamak during "fish-bones" activity [27]. These losses have been observed concentrated near the mid plane and only when the beam has a particular phase with respect to the instabilities.

Another possible loss mechanism suggested for the first time by H. E. Mynick [28] is orbit stochasticity. This process does not depend on a resonant interaction with the mode; rather the helical distortion of the field beats with harmonics of the orbital motion causing island overlap in the particle phase space. Once island overlap occurs, the particles diffuse rapidly. Transport associated with orbit stochasticity only occurs above a threshold in the mode amplitude. It is important to understand that even fast particles on passing drift orbits, which are normally thought of as well confined, can be affected by orbit stochasticity. A more recent study of beam ion transport during coherent MHD activity [29] suggests that these losses scale approximately as \tilde{B}^2 . In that work, Tearing Modes were observed to reduce the neutral beam current drive efficiency by a factor of 40 % through orbit stochasticity. On a positive side, orbit stochasticity has been connected with a technique of removing intermediate energy α -particles in a reactor through the external application of helical perturbations [28].

ICRH enhanced fast ion loss The Ion Cyclotron Resonance Heating system may accelerate in general all kinds of ions, from plasma bulk ions or NBI heated ions up to α -particles, preferentially in the perpendicular component of the motion. The fundamental interaction in this case usually occurs in a narrow range of minor radii for particles of given energy. This interaction can increase the energy or magnetic moment of for example, fusion born α - particles, causing some of them to be lost across the passing-trapped boundaries. RF induced loss of fast ions has been observed in several tokamaks: TFTR [30] , JT-60U [31] and TEXTOR [32]. The wave fields produce a change in particle velocity given by $\delta v \propto E_{RF} \propto P_{RF}^{0.5}$, [30].

1.4 Aim of the Work

It is the aim of this work to study in depth the losses of fast ions generated by additional heating systems in ASDEX Upgrade, especially in the presence of MHD perturbations. Although α particles have a higher energy and a more isotropic distribution function than either the NBI or ICRH fast ions, their low density in ASDEX Upgrade D-D plasmas makes them not appropriate for the study of wave-particle interactions. Considering the distribution function of the background ions in the velocity space as a Maxwellian distribution, this work concerns

particles which have a much higher energy than the thermal energy of the background plasma and their density is much higher than that in the tail of the Maxwellian. Expected velocities of such ions are very high compared with velocities of thermal ions, but not high enough for considering the relativistic correction. The given values for ions with an energy of several 10s of keV (40-1000 keV) are around 10^6 m/s. Thus, the relativistic correction is small and the non relativistic mechanic is accurate enough.

In order to identify the lost ion population during each MHD event in ASDEX Upgrade plasmas it is necessary to have a very flexible diagnostic capable of covering the whole pitch angle and energy ranges existing, from NBI up to ICRH heated ions. Characteristic frequencies of most importance Alfvén instabilities in ASDEX Upgrade can be up to 500 kHz, making very fast measurements necessary to clarify each loss mechanism.

1.5 Dissertation Outline

The development of a new diagnostic for the study of fast particle-wave interactions in ASDEX Upgrade as well as the interpretation of the first measurements have been the aim of this thesis which is outlined here.

A brief introduction to Thermonuclear Fusion is given within the first pages. The definition of a tokamak and the importance of good fast ion confinement are described in this chapter. The aim of this work together with a motivation based on previous works are presented in the previous sections. In Chapter 2, the different charged particle trajectories in a tokamak are presented together with the underlying physics. A second section in Chapter 2 is dedicated to an introduction of the main MHD perturbations existing in a tokamak to make possible a theoretical analysis of the interaction between fast ions and MHD activities. The whole diagnostic set-up is described in Chapter 3, placing special emphasis on the most challenging issues, the geometry of the detector head and the choice of the scintillator material. Chapter 4 gives an overview of the fast ion sources available in the ASDEX Upgrade tokamak as well as of the particle distribution anisotropies in phase space introduced by each fast particle source. In Chapter 5, the most relevant MHD induced fast ion loss measurements obtained during the first operation campaigns are presented. A detailed explanation of the first conclusions derived from these measurements is given in Chapter 6. Finally, a last chapter is dedicated to a summary.

Chapter 2

Theoretical Background

2.1 Charged Particle Motion in Tokamaks

As is well-known, a charged particle in a homogeneous magnetic field is tied to field lines by the Lorentz force as long as there is no other interaction. In this section, the motion of charged particles in a weak spatial varying magnetic field is analyzed. The strength of the magnetic field is taken such that the gyro-period and the gyroradius of the particle motion around field lines are the shortest time and length scales of the system. The particle motion is usually described as the sum of a fast gyro-motion and a slow drift velocity. In order to confine the particles in a bounded volume like a tokamak, the magnetic field must be curved and inhomogeneous.

2.1.1 Gyration and Drifts

Motion in a Constant Magnetic Field

The motion of charged particles in the presence of a constant magnetic field \mathbf{B} is governed by the Lorentz force,

$$m\dot{\mathbf{v}} = q(\mathbf{v} \times \mathbf{B}). \quad (2.1)$$

The kinetic particle energy remains constant because the Lorentz force is always perpendicular to the velocity and can therefore change only its direction, but not its magnitude. The particle velocity can be then decomposed into components parallel and perpendicular to the magnetic field, $\mathbf{v} = v_{\parallel} \mathbf{b} + \mathbf{v}_{\perp}$, where $\mathbf{b} \equiv \mathbf{B}/B$ is the unit vector in the direction of \mathbf{B} . The Lorentz force does not affect the parallel motion: $v_{\parallel} = \text{constant}$. Only v_{\perp} interacts with \mathbf{B} , leading to a circular motion perpendicular to \mathbf{B} .

The centrifugal force mv_{\perp}^2/r balances the Lorentz force $qv_{\perp}B$ for a gyroradius ρ equal to

$$\rho = \frac{mv_{\perp}}{qB}. \quad (2.2)$$

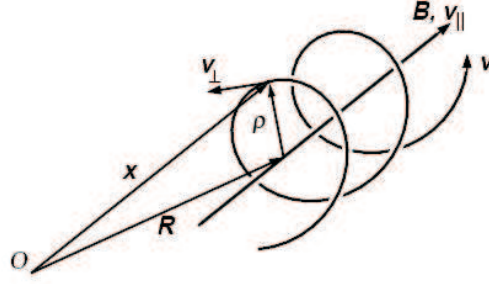


Figure 2.1: Definition of guiding center coordinates.

The frequency of the gyration, called cyclotron frequency ω_c , follows from $v_{\perp} = \omega_c \rho$,

$$\omega_c = \frac{qB}{m}. \quad (2.3)$$

As illustrated in Fig.2.1, the particle position \mathbf{x} can be decomposed into a guiding center position \mathbf{R} that moves with velocity $v_{\parallel} \mathbf{b}$, and a rotating radius vector ρ ,

$$\mathbf{x} = \mathbf{R} + \rho, \quad (2.4)$$

$$\rho = -\frac{m}{qB^2} \mathbf{v} \times \mathbf{B}. \quad (2.5)$$

The particle trajectory is a helix around the guiding center magnetic field line, see Fig.2.2.

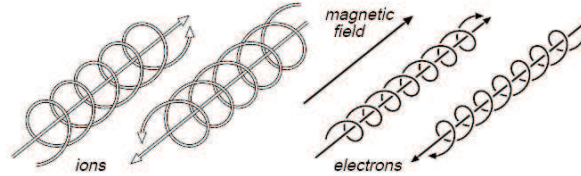


Figure 2.2: Orientation of the gyration orbits of electrons and ions in magnetic field. The guiding center is also shown.

Drift due to Additional Force

If, in addition to the Lorentz force, a constant force \mathbf{F} acts on the charged particle, the equation of motion is

$$m\dot{\mathbf{v}} = q(\mathbf{v} \times \mathbf{B}) + \mathbf{F}. \quad (2.6)$$

The motion of the particle due to \mathbf{F} can be separated from the gyration due to \mathbf{B} by using the guiding center as reference frame. From Eq.(2.4), the velocity of the guiding center can be obtained, leading to,

$$\mathbf{v} \equiv \dot{\mathbf{R}} = \dot{\mathbf{x}} - \dot{\boldsymbol{\rho}} \quad (2.7)$$

$$= \mathbf{v} + \frac{m}{qB^2} \dot{\mathbf{v}} \times \mathbf{B} \quad (2.8)$$

$$= \mathbf{v} + \frac{1}{qB^2} (q\mathbf{v} \times \mathbf{B} + \mathbf{F}) \times \mathbf{B}. \quad (2.9)$$

Using $(\mathbf{v} \times \mathbf{B}) \times \mathbf{B} = -v_{\perp} B^2 \hat{\mathbf{b}}$ and $\mathbf{v} - v_{\perp} \hat{\mathbf{b}} = v_{\parallel} \hat{\mathbf{b}}$ we obtain

$$\mathbf{v} = v_{\parallel} \hat{\mathbf{b}} + \frac{\mathbf{F} \times \mathbf{B}}{qB^2}. \quad (2.10)$$

Therefore, any force with a component perpendicular to \mathbf{B} causes a particle to drift perpendicular to both \mathbf{F} and \mathbf{B} . The basic mechanism for a drift in this direction is a periodic variation of the gyroradius. When a particle accelerates in a force field, the gyroradius increases and when it slows down its gyroradius decreases, leading to the non-closed trajectories shown in Fig. 2.3. The net effect is a drift perpendicular to the force and the magnetic field. A force parallel to \mathbf{B} does not lead to a drift, but simply causes a parallel acceleration as can be seen from Eq.(2.6). Summarizing,

$$\mathbf{v}_D = \frac{\mathbf{F}_{\perp} \times \mathbf{B}}{qB^2}, \quad \frac{dv_{\parallel}}{dt} = \frac{\mathbf{F}_{\parallel}}{m}. \quad (2.11)$$

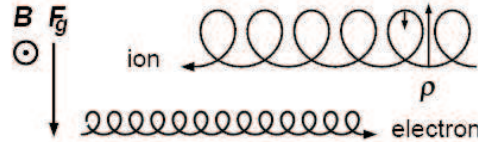


Figure 2.3: Ion and electron drift due to an additional force, F_g .

$\mathbf{E} \times \mathbf{B}$ Drift

A different situation arises in the presence of a constant electric force $q\mathbf{E}$. Since the electric force is in opposite directions for electrons and ions, the resulting drift velocity,

$$\mathbf{v}_E = \frac{\mathbf{E} \times \mathbf{B}}{B^2}, \quad (2.12)$$

does not depend on the sign of the particle charge. It is also independent of the particle mass and therefore identical for ions and electrons. Hence, this drift leads to a net flow of the plasma, rather than to a current (see Fig.2.4).

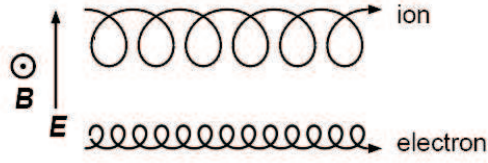


Figure 2.4: $\mathbf{E} \times \mathbf{B}$ ion and electron drift.

Particle Drift in Inhomogeneous Magnetic Fields

For spatially weakly varying magnetic fields, Eq.(2.11) can still be applied if the relative variation of \mathbf{B} along one particle gyration is small. A curvature of the magnetic field lines gives rise to a such field inhomogeneity. For a particle that moves along a curved magnetic field line the separation of its velocity into v_{\perp} and v_{\parallel} changes with its position. The curvature is given by $\nabla_{\parallel} \mathbf{b} = -\mathbf{R}_c/R_c^2$, a vector $\perp \mathbf{B}$. Here $\nabla_{\parallel} \equiv \mathbf{b} \cdot \nabla$ is the gradient along \mathbf{B} and \mathbf{R}_c is the curvature radius shown in Fig. (2.5). A particle following the curved field line with velocity v_{\parallel} experiences a centrifugal force $\mathbf{F}_c = mv_{\parallel}^2 \mathbf{R}_c/R_c^2$, which is responsible for the drift velocity

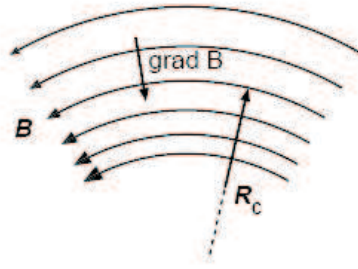


Figure 2.5: Inhomogeneous magnetic field. Relation between the curvature radius and the field gradient.

$$\mathbf{v}_c = \frac{mv_{\parallel}^2}{qB^2} \mathbf{B} \times \nabla_{\parallel} \mathbf{b}. \quad (2.13)$$

The other inhomogeneity that results in a drift is the transverse gradient of the magnetic field strength. The particle orbit has a smaller radius of curvature on that part of its orbit located in the stronger magnetic field. This leads to a drift perpendicular to both the magnetic field and its gradient. We discuss the averaged effect of ∇B on the gyro-orbit by considering the current $I = q\omega_c/2\pi$ associated with the gyro-motion of a charged particle. The magnetic moment is defined as the product of the current and the area which is surrounded by the current. Since the area encompassed by the gyro-orbit equals $\pi\rho^2$, the magnetic moment per unit particle mass is

$$\mu = \pi\rho^2 \frac{I}{m} = \pi\rho^2 \frac{q^2 B}{2\pi m^2} = \frac{v_{\perp}^2}{2B}. \quad (2.14)$$

The gyro-averaged force equals the force on a magnetic dipole in a magnetic field gradient,

$$\mathbf{F}_{\nabla B} = -m\mu\nabla B. \quad (2.15)$$

Application of Eq.(2.11) to this force yields the ∇B -drift,

$$\mathbf{v}_{\nabla B} = \frac{mv_{\perp}^2}{2qB^3}\mathbf{B} \times \nabla B. \quad (2.16)$$

In a tokamak, the curvature and ∇B drifts are often comparable. In a plasma in equilibrium one has approximately $\nabla \times \mathbf{B} \parallel \mathbf{B}$. For a pressure gradient $\nabla p = 0$ this relation is exact. It implies a relation between the curvature vector and ∇B , illustrated in Fig.(2.5),

$$\nabla_{\parallel} \mathbf{b} = \frac{\nabla_{\perp} B}{B}. \quad (2.17)$$

Using this relation, the ∇B and curvature drifts, (2.13) and (2.16) can be combined to

$$\mathbf{v}_c + \mathbf{v}_{\nabla B} = \frac{m}{qB^3}(v_{\parallel}^2 + \frac{1}{2}v_{\perp}^2)\mathbf{B} \times \nabla B. \quad (2.18)$$

Averaged over a thermal velocity distribution, this drift velocity equals $2T/qBR_c$.

2.1.2 Adiabatic Invariants and Particle Orbits in Tokamaks

When a system performs a periodic motion, the action integral $I = \oint PdQ$, taken over one period, is a constant of motion, where P is a generalized momentum and Q the corresponding coordinate. For slow changes of the system (compared with the characteristic time of the periodic motion) the integral I remains constant and is called an *adiabatic invariant*. More precisely: if the system changes on a time scale τ , and the frequency of the periodic motion is ω , then changes to I of the order $\Delta I \approx e^{-\omega\tau}$ can be expected.

The first adiabatic invariant is the magnetic moment $\mu = v_{\perp}^2/2B$ defined in Eq.(2.14), which is proportional to the magnetic flux $\pi\rho^2B$ enclosed by the gyro-orbit. The periodic motion is the Larmor gyration, P is the angular momentum $mv_{\perp}\rho$ and the coordinate Q is the angle ϕ . We get

$$\oint PdQ = \oint mv_{\perp}\rho d\phi = 2\pi\rho mv_{\perp} = 4\pi\frac{m^2}{q}\mu. \quad (2.19)$$

A second adiabatic invariant, the longitudinal invariant $J = \oint mv_{\parallel}dl$, is defined as the integral over the periodic orbit for trapped particles in mirror geometries. Defining the length L between two turning points and the average longitudinal velocity $\langle v_{\parallel} \rangle$, the constant of motion is $J = 2m \langle v_{\parallel} \rangle L$. If L decreases, $\langle v_{\parallel} \rangle$ increases.

Trapped Orbits

The invariance of μ plays a crucial role in particle trajectories in magnetically confined plasmas. Charged particles can get trapped, changing their velocity direction due to magnetic mirrors. The mirror effect occurs when a particle guiding center moves toward a region with a stronger magnetic field. As Fig. 2.6 shows, the particle experiences a magnetic field change $\dot{B} = v_{\parallel} \nabla_{\parallel} B$ which together with the constants of motion, μ and $\epsilon = \frac{1}{2}v_{\perp}^2 + \frac{1}{2}v_{\parallel}^2 = \mu B + \frac{1}{2}v_{\parallel}^2$, leads to a variation of the parallel velocity.

In general, the change of parallel velocity of a particle in a (spatially or temporally) varying magnetic field can be determined from the constancy of μ and ϵ in

$$v_{\parallel}(B) = \pm \sqrt{2(\epsilon - \mu B)}. \quad (2.20)$$

Fig.2.6 shows the principle of particle confinement in a magnetic mirror. The criterion for particle reflection ($v_{\parallel} = 0$) at the high field ends of the magnetic mirror is

$$\epsilon = \frac{1}{2}v_{\parallel,0}^2 + \mu B_{min} \leq \mu B_{max}, \quad (2.21)$$

where $v_{\parallel,0}$ is the parallel velocity in the low field region. If we divide Eq.(2.21) by $\mu B_{min} = \frac{1}{2}v_{\perp,0}^2$, we obtain

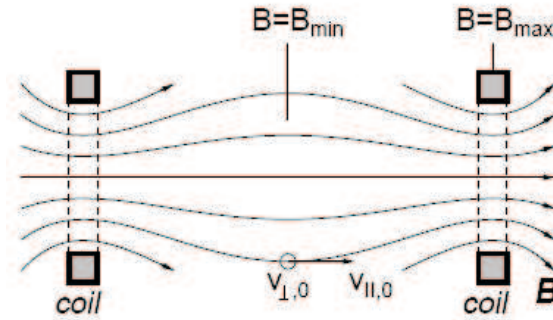


Figure 2.6: Reflected particle in a magnetic bottle.

$$\frac{v_{\parallel,0}}{v_{\perp,0}} < \sqrt{B_{max}/B_{min} - 1} \quad (2.22)$$

as the criterion for particle trapping.

Applying the magnetic mirror to a tokamak with circular cross section, we obtain that the particle is reflected as usual if $\epsilon < \mu B_{max}$ at the point where $\epsilon = \mu B_{tp}$, see Fig.2.7. The particle is then trapped between magnetic mirrors and bounces between turning points. The particle trajectory can be calculated from the equation of a force applied on a magnetic dipole in a parallel magnetic field gradient $F = -m\mu \nabla_{\parallel} B$. Using the major radius coordinate $R = R_0 + r \cos(\theta)$, the parallel gradient of the magnetic field, dB/ds , may be obtained using

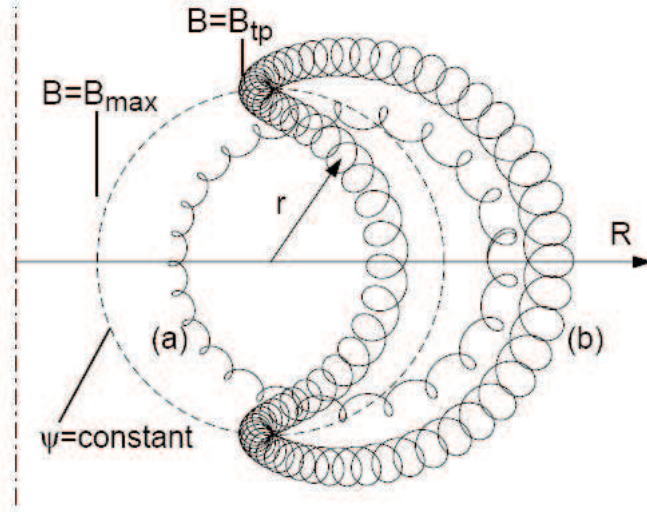


Figure 2.7: Projection of a passing (a) and a trapped (b) particle on a poloidal plane.

$$B = B_0 \frac{R_0}{R} = \frac{B_0}{1 + (r/R_0)\cos\theta} \quad (2.23)$$

which for strongly trapped particles and large aspect-ratio gives

$$\frac{dB}{ds} = \frac{rB_0}{R_0} \frac{d(\theta^2/2)}{ds}. \quad (2.24)$$

Taking the parallel gradient of the magnetic field, dB/ds , and the equation of a field line $r d\theta/ds = B_\theta/B$, the equation of motion for *deeply trapped* particles ($\theta = \frac{v_{\parallel}}{v_{\perp}} \ll 1$) is given by [1]

$$\frac{d^2s}{dt^2} = -\omega_b^2 s \quad (2.25)$$

where ω_b is the bounce frequency defined as

$$\omega_b = \frac{v_{\perp}}{qR_0} \left(\frac{r}{2R_0} \right)^{\frac{1}{2}} \quad (2.26)$$

Here, $q = rB_0/R_0B_\theta$ with subscript zero denoting the center of the poloidal cross section.

The drift surface on which the trapped particle lies is now obtained by including the r component of the vertical drift due to the toroidal magnetic field. Taking $v_{\perp} \gg v_{\parallel}$, this drift is almost constant $v_D = \frac{1}{2}mv_{\perp}^2/qRB_\phi$.

Following [1], the previous assumptions lead to a drift surface

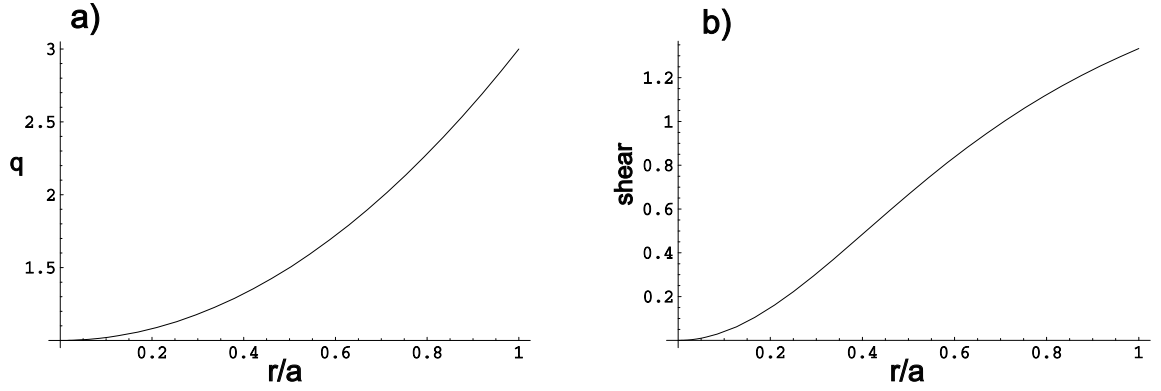


Figure 2.8: Analytical profiles in cylindric approach; safety factor $q(r) = 1 + 2(r/a)^2$ and magnetic shear $\hat{s}(r) = 4r^2/q(r)$ normalized to the minor plasma radius.

$$(r - r_0)^2 = \left(\frac{\theta_b v_D}{\omega_b} \right)^2 \left(1 - \left(\frac{\theta}{\theta_b} \right)^2 \right), \quad (2.27)$$

where $\theta_b = \frac{v_{\parallel 0}}{v_{\perp 0}} \left(\frac{2R_0}{r} \right)^{1/2}$ is the bounce angle. This equation represents a curve with the shape of a banana as shown in Fig.2.7. The half-width, Δr , of the orbit is

$$\Delta r = \frac{\theta_b v_D}{\omega_b} = \frac{v_{\parallel 0}}{\omega_\theta} \quad (2.28)$$

where $\omega_\theta = eB_\theta/m$, therefore Δr is equal to the Larmor radius calculated for a particle of velocity $v_{\parallel 0}$ using the poloidal magnetic field B_θ .

Assuming in the cylindrical approach, a safety factor $q(r) = 1 + 2(r/a)^2$, shown in Fig.2.8.a, the dependence of the bounce frequency on the minor radius, r , for a typical deeply trapped deuterium ion with an energy $E=100\text{keV}$ and a pitch angle of $\frac{v_{\parallel}}{v_{tot}} = 0.17$ in a toroidal magnetic field $B_t = 1.95\text{T}$ at the magnetic axis with a minor plasma radius $a = 0.5\text{m}$ may be calculated and is shown in Fig.2.9. The banana width of this particle trajectory is, using Eq.(2.28), of $2 \cdot \Delta r = 251.5\text{mm}$ near the center of the poloidal cross section.

The gyrocenter motion of a charged particle consists of a motion in the direction of the magnetic field, and a slow motion across the magnetic field due to the inhomogeneity of the magnetic field. This motion across the magnetic field leads to a slow toroidal motion of this orbit. Analytic expressions for the orbit drift are obtained in the approximation of the magnetic geometry by concentric circular flux surfaces, following [33]. The derived expressions are accurate only in lowest order in the inverse aspect ratio $\epsilon = r/R$. The drift of the orbit has two contributions that are both due to the inhomogeneity of the magnetic field. The first contribution is due to the poloidal component of the vertical ion drift Eq.(2.18). Actually, the drift of trapped particles is mostly due to the grad B drift of the inhomogeneous magnetic field, being the curvature drift of minor importance because of the low parallel velocity compared with the perpendicular velocity. The second effect that causes a toroidal drift of the orbit is

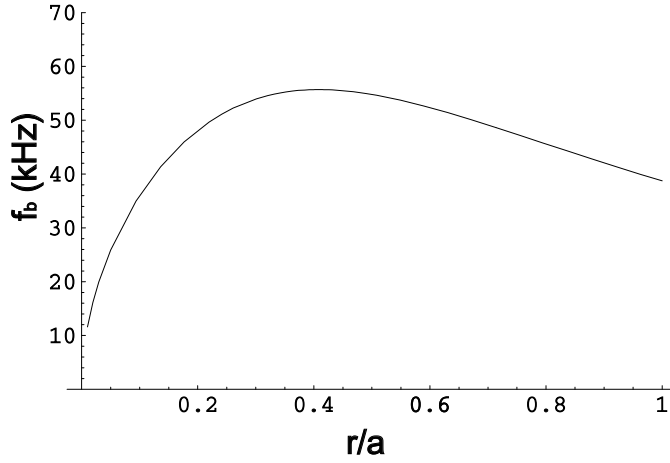


Figure 2.9: Dependence of the bounce frequency on the minor plasma radius for a deeply trapped deuterium ion with an energy $E = 100keV$ and $\frac{v_{\parallel}}{v_{tot}} = 0.17$.

the dependence of the magnetic winding number q on the minor radius. This dependence in combination with the previously introduced excursion of the trapped particle from the surface leads to a difference in toroidal distance between the bounce points for the inner and the outer leg of the trapped particle orbit. The orbit is then shifted slightly after a bounce period. Because the motion in toroidal and poloidal direction are related through the helicity of the field line, the toroidal motion of trapped particle orbit due to the poloidal component $\dot{\theta}_{drift}$ of the vertical ion drift is

$$\dot{\phi}_0 = q\dot{\theta}_{drift} + \vartheta(\varepsilon), \quad (2.29)$$

where ϕ_0 is the initial toroidal position of the particle. The combination of these two effects bounce averaged over the orbit to the lowest order in the aspect ratio gives for the precession frequency [33],

$$\omega_{prec} = \langle \dot{\phi}_0 \rangle_B = \frac{qv^2}{2\omega_c R^2 \varepsilon} H(\kappa^*, \hat{s}) \{1 + O(\varepsilon)\}, \quad (2.30)$$

with

$$H(\kappa^*, \hat{s}) = 4\hat{s}(\kappa^{*2} - 1) - 1 + 2(1 + 2\hat{s}) \frac{E(\kappa^{*2})}{K(\kappa^{*2})}, \quad (2.31)$$

and

$$\kappa^* = \sqrt{\frac{1 + \varepsilon}{2\varepsilon} \cos \theta_0}. \quad (2.32)$$

where \hat{s} is the shear, $\hat{s}(r) = (r/q)dq/dr$, which for normal current profiles varies between zero on the magnetic axis and two at the plasma edge. Taking the q -profile introduced previously

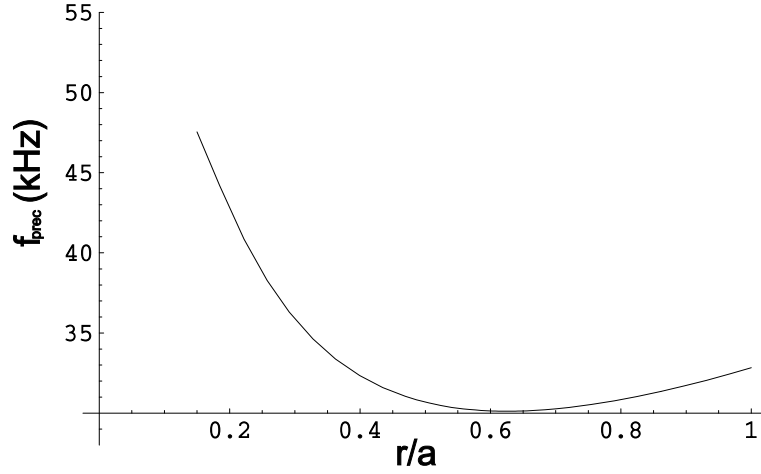


Figure 2.10: Dependence of the precession frequency on the minor plasma radius for a deeply trapped deuterium ion with an energy $E = 100keV$ and $\frac{v_{\parallel}}{v_{tot}} = 0.17$.

and a shear, $\hat{s}(r) = \frac{4(r/a)^2}{q(r)}$, see Fig. 2.8.b, the dependence of the precession frequency on the minor plasma radius r for a deuterium ion with an energy $E = 100keV$ and a pitch angle of $\frac{v_{\parallel}}{v_{tot}} = 0.17$ in a toroidal magnetic field $B_t = 1.95T$ at the magnetic axis is shown in Fig.2.10.

Passing Orbits

In a tokamak, the field strength has its maximum value at the inside of the torus. A particle traveling along a field line feels a periodic mirror force. If the energy and magnetic moment of this particle have values such that $\epsilon > \mu B_{max}$, the particle is not reflected and continues its course and encircles the torus. These passing particle orbits lie as well as the trapped ones on toroidally symmetric drift surfaces. The distance, d , between the drift surface and the magnetic surface can be calculated directly from the expression for the drift velocity. The drift surfaces of passing particles can be determined by the two components of the particle motion. The first one will be the motion parallel to the magnetic field, which gives rise to a poloidal rotation. For particles which are strongly passing, this rotation has a frequency $\omega = (B_{\theta}/B)v_{\parallel}/r$ [1], see Fig.2.11. The second component is the vertical drift due to the gradient and curvature of the toroidal field. Combining these motions, the equations for the drift orbit become

$$\frac{dr}{dt} = \omega z, \quad \frac{dz}{dt} = -\omega(r - r_0) + v_D \quad (2.33)$$

where z is the vertical coordinate and r_0 is the r coordinate of the center of the cross-section of the magnetic surface.

The resulting equation for the drift surface is

$$\left(r - r_0 - \frac{v_D}{\omega}\right)^2 + z^2 = constant. \quad (2.34)$$

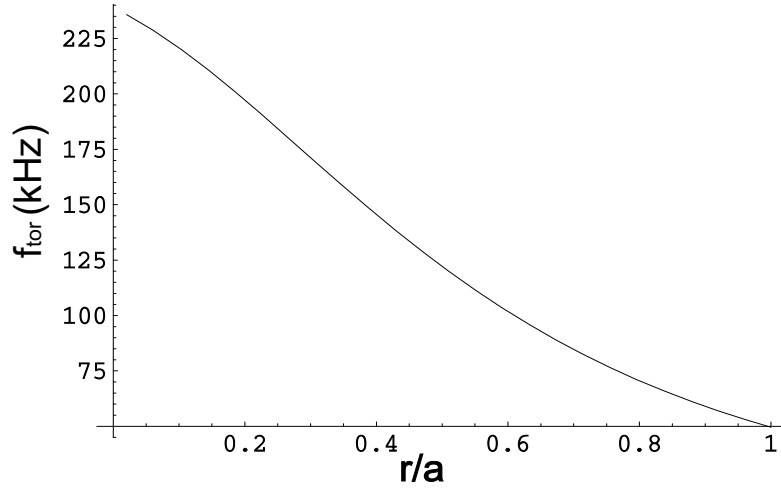


Figure 2.11: Dependence of the toroidal rotation frequency on the minor plasma radius of a circulating deuterium ion with an energy $E = 100keV$ and a pitch angle $\frac{v_{\parallel}}{v_{tot}} = 0.8$.

As Fig. 2.7 shows, it represents a circular surface displaced from the magnetic surface by a distance

$$d = \frac{-v_D}{\omega} \simeq -\frac{r v_{\parallel}}{R \omega_{\theta}} \quad (2.35)$$

where $\omega_{\theta} = \frac{qB_{\theta}}{m}$.

2.2 MHD Activity in Tokamaks

A large variety of magnetohydrodynamic (MHD) instabilities may occur in typical fusion plasmas, depending on the main plasma parameters and the applied heating schemes. One can distinguish between three main groups of MHD perturbations; MHD instabilities which appear due to current density gradients, due to thermal pressure gradients and due to fast particle pressure gradients. In this section the main MHD instabilities are briefly presented connecting them with fast ion behavior.

2.2.1 Fishbone Modes

Historically, fishbones are the first fast ion driven MHD instability identified in a fusion plasma device [34] and therefore their origin, topology and behavior are well known. It has been found that under certain conditions the injection of high energy neutral beams to heat the plasma can lead to an instability associated with a significant loss of fast ions. The fishbone instability is an ideal instability localized on the $q=1$ surface, although it has been recently discovered that

it also has a resistive character [35]. This perturbation owes its name to the characteristic signature on the magnetic pick-up (Mirnov) coils, see Fig.2.12.a. Another characteristic feature is the decrease of the oscillation frequency of the ($m=1, n=1$) mode within a single fishbone burst, Fig.2.12.b.

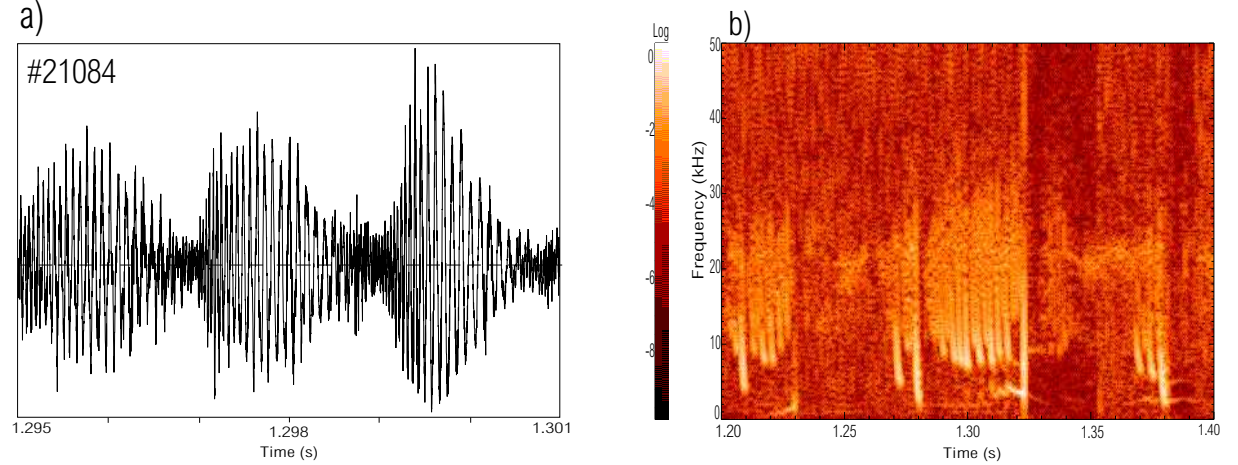


Figure 2.12: Typical signature of fishbones in the magnetic pick up coils.

The most severe effect of the fishbone instability is the ejection of the resonant fast ions driving the instability during the bursts, [36]. Two different models for the underlying destabilization mechanisms of the fishbone instability have been proposed [37], [38]. The first suggests that injected fast beam particles trapped within the $q = 1$ surface can kinetically destabilize a mode ($m = 1, n = 1$) becoming resonant by means of their toroidal precession frequency Eq.(2.30). This theory predicts that the (1, 1) fishbone mode occurs if the pressure of the fast trapped ions is sufficiently high. The other model extends this theory by including the effect of the finite diamagnetic frequency,

$$\omega_{di} = \frac{1}{eBn} \nabla p_i \quad (2.36)$$

evaluated at the $q = 1$ surface (here, ∇p_i denotes the ion pressure gradient of the plasma bulk and n the plasma density).

Kass et al [36] have proved experimentally that the destabilization mechanism of the fishbone instability depends strongly on the trapped fraction of the fast particles at and within the $q=1$ surface. The fishbone instability occurs in ASDEX Upgrade only above a certain threshold in the fast particle pressure ($\beta_{fast} = \beta_{tor}/(1 + \tau_E/\tau_{sd})$), where τ_{sd} is the fast ion slowing down time. The initial frequency of the fishbone mode scales with the toroidal precession frequency of the trapped ions. The mode structure is dominated by an ($m = 1, n = 1$) mode, but higher poloidal harmonics with $m > 1$ are also observed. The rotation direction is in the ion diamagnetic drift direction. The fishbone instability is enhanced on the low field side.

2.2.2 Alfvén Instabilities

As described before in magnetic confined plasmas, charged particles have to follow due to the Lorentz Force, the magnetic field lines. On the other hand, magnetic fields are tied to charged particles. The motion of a charged particle in a magnetic field generates an electric field $\vec{E} = -\vec{v} \times \vec{B}$, which produces following the Faraday law a time variable magnetic field $\vec{\nabla} \times \vec{E} = -\partial\vec{B}/\partial t$. The total magnetic field is then the result of both, the original magnetic field, and the magnetic field generated by the charged particle motion. This coupled system of magnetic fields and charged particles may be excited forming characteristic waves in the plasma. One can distinguished three types of these waves. Firstly, the shear Alfvén waves which are incompressible waves and therefore unaffected by the plasma pressure. The other two involve compression and their wave velocities are given by both the Alfvén speed and the sound speed. As a consequence, these are called magnetosonic waves. The dispersion relation of these waves may be obtained from the 'ideal MHD' equations:

$$\frac{\partial \rho}{\partial t} + \nabla \cdot (\rho \mathbf{v}) = 0 \quad (\text{Mass continuity}) \quad (2.37)$$

$$\rho \frac{\partial \mathbf{v}}{\partial t} + \rho \mathbf{v} \cdot \nabla \mathbf{v} + \nabla P - \mathbf{j} \times \mathbf{B} = 0 \quad (\text{Momentum balance}) \quad (2.38)$$

$$\frac{\partial P}{\partial t} + \mathbf{v} \cdot \nabla P + \gamma P \nabla \cdot \mathbf{v} = 0 \quad (\text{Adiabatic equation of state}) \quad (2.39)$$

$$\mathbf{E} + \mathbf{v} \times \mathbf{B} = 0 \quad (\text{Ohm's Law}) \quad (2.40)$$

$$\nabla \cdot \mathbf{B} = 0 \quad (\text{No magnetic monopoles}) \quad (2.41)$$

$$\nabla \times \mathbf{B} - \mu_0 \mathbf{j} = 0 \quad (\text{Ampere's Law}) \quad (2.42)$$

$$\frac{\partial \mathbf{B}}{\partial t} + \nabla \times \mathbf{E} = 0 \quad (\text{Faraday's Law}) \quad (2.43)$$

where ρ is the mass density of the plasma, \mathbf{j} is the current density, \mathbf{v} is the plasma velocity, P is the plasma pressure and γ is the adiabaticity index. The electric and magnetic fields, \mathbf{E} and \mathbf{B} , that appear in these expressions consist of the externally applied fields and the averaged internal fields. To identify the classes of waves and instabilities in a plasma, these non-linear equations can be linearized rewriting all quantities as the sum of an equilibrium time-independent term and a small first-order time-dependent perturbation, $Q(r, t) = Q_0(r) + \tilde{Q}_1(r, t)$. Following the procedure shown in [39] in a homogeneous and stationary slab of plasma the wave equation obtained from this MHD model leads to the dispersion relation

$$(\omega^2 - k_{\parallel}^2 v_A^2)[\omega^4 - (v_S^2 + v_A^2)k^2 \omega^2 + (kk_{\parallel} v_S v_A)^2] = 0, \quad (2.44)$$

where ω is the frequency, k the wave vector, $v_A = \sqrt{B_0^2 / \mu_0 \rho_0}$ is the Alfvén speed and $v_S = \sqrt{\gamma P_0 / \rho_0}$ is the sound speed.

Each solution of this equation represents a mode of oscillation of the plasma and since it is a cubic polynomial in ω^2 three modes are expected. The first solution,

$$\omega^2 = k_{\parallel}^2 v_A^2, \quad (2.45)$$

corresponds to the Alfvén branch and it is independent of k_{\perp} , even when $k_{\perp} \gg k_{\parallel}$. These are incompressible ($\rho_1 = P_1 = 0$) transverse waves with both v_1 and B_1 perpendicular to B_0 .

The quadratic term for ω^2 in Eq.(2.44) gives rise to two further branches, the fast and slow magnetosonic waves, which arise from the coupling between magnetic compression (Alfvénic) and fluid compression (sonic). The solutions are

$$\omega^2 = \frac{1}{2}k^2(v_S^2 + v_A^2) \left[1 \pm \sqrt{1 - 4 \frac{k_{\parallel}^2}{k^2} \frac{v_A^2 v_S^2}{(v_A^2 + v_S^2)^2}} \right]. \quad (2.46)$$

The positive sign in Eq.(2.46) corresponds to the fast magnetosonic or magnetoacoustic wave and always oscillates at frequencies greater than the Alfvén wave. This is a compressional wave, and so $\nabla \cdot v_1$ and P_1 are non-zero, with B_1 having components both parallel and perpendicular to the equilibrium field B_0 .

The negative sign in Eq.(2.46) corresponds to the slow magnetosonic wave which always oscillates at frequencies below that of the Alfvén wave. As for the fast branch, the wave is polarized so that the plasma pressure and the magnetic field are compressed.

Toroidicity induced shear Alfvén Eigenmodes (TAE)

In this section, emphasis is placed on the understanding of shear Alfvén continuous spectra in axisymmetric toroidal plasmas [40], since it has been found that Alfvén waves can be destabilized through resonant interactions with certain populations of fast ions via inverse Landau damping [41].

In order to examine the Alfvén frequency continuum in toroidal geometries, one can start with a first approach, a torus with infinite large aspect ratio $A = R/a \rightarrow \infty$, where R is the major radius and a is the plasma radius and periodic boundary conditions. In a torus due to the periodic boundary conditions only discrete values of \mathbf{k} are allowed. Only waves which after a finite number of circulations are in phase with itself can remain in the plasma, waves not in phase with itself interfere destructively and disappear. The perturbation described by an Alfvén wave has then to fulfill the periodic boundary conditions: $f(\phi = 0) = f(\phi = 2\pi n)$ and $f(\theta = 0) = f(\theta = 2\theta n)$. The unique possible solution for such a perturbation is then given by $f \approx e^{i(m\theta + n\phi - \omega_{n,m}t)}$. The possible Alfvén waves are then restricted to those with discrete m and n mode numbers. This means, at each flux surface ($q = m/n$), a wave appears which does not propagate, describing an oscillation. At the other flux surfaces, exciting a shear Alfvén wave appear a wave with a frequency and a phase velocity along the field lines given by the Eq.(2.45):

$$\omega_{A,\parallel}^2 = k_{\parallel,m}^2 v_A^2 \quad (2.47)$$

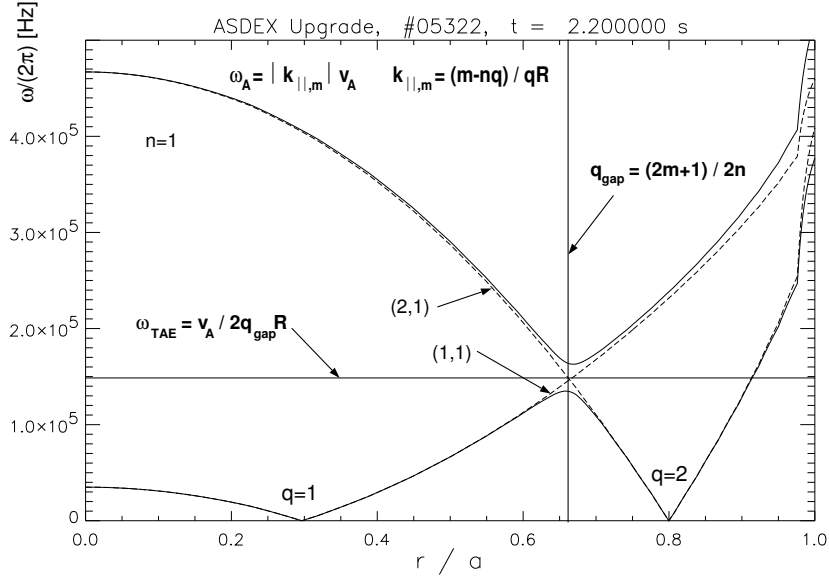


Figure 2.13: Degeneracy of the Alfvén continuum.

Decomposing the wave vector in a flux surface into its toroidal and poloidal components, one obtains for $k_{||,m,n}$

$$k_{||,m,n} = \frac{m/q - n}{R} \Rightarrow \omega_{A,||} = \left| \frac{m - nq}{qR} \right| v_A. \quad (2.48)$$

In Fig.2.13, the dispersion relation for the modes $n=1$ and $m=1,2$ in a typical discharge of ASDEX Upgrade in the cylindrical approach (dashed line) is illustrated. The q -value at the intersection radius between the adjacent Fourier components is then given by $\omega_A(m) = -\omega_A(m')$

$$q_{intersection} = \frac{m + m'}{2n} \quad (2.49)$$

The Alfvén frequency of the intersection can be then obtained substituting $q_{intersection}$ in the dispersion relation for two adjacent Fourier components, $\Delta m = m' - m = 1$, giving

$$\omega_{intersection} = \frac{v_A(q_{intersection})}{2q_{intersection}R} = \frac{2n}{2m+1} \frac{v_A(q_{intersection})}{2R}. \quad (2.50)$$

For a given n , the curves $\omega(r)$ break and join at their intersections due to the toroidicity, leaving gaps in $\omega(r)$. In addition, the toroidal coupling effects not only break up the shear Alfvén continuous spectrum, but also result in a discrete, global toroidicity-induced shear Alfvén eigenmodes (TAEs) with frequencies inside the continuum gaps,

$$\omega_{TAE} = \frac{v_A(q_{TAE})}{2q_{TAE}R} \quad (2.51)$$

Whereas the shear Alfvén waves of the continuum are strongly damped, the weaker damping of the TAE can be overcome by a destabilizing interaction with fast particles or external launched waves like the ICRF Beat Waves.

2.2.3 Neoclassical Tearing Modes (NTMs)

Up to now, we have studied only ideal instabilities for which dissipative effects are negligible and magnetic field lines stay frozen in the plasma. However, in a tokamak one of the main dissipative processes is related to the presence of resistivity. Taking into account a finite resistivity in the linearization of the ideal MHD Eqs.(2.37)-(2.43) and combining 2.43 and 2.40 with a local current perturbation \mathbf{j}_1 , one obtains

$$\frac{\partial B_1}{\partial t} = \nabla \times (v_1 \times B_0) - \frac{1}{\sigma} j_1. \quad (2.52)$$

This current perturbation \mathbf{j}_1 is not perpendicular to the main magnetic field, in contrast to the ideal equations. By applying the curl to Ampere's law, a diffusion equation $\Delta B = D \frac{\partial B}{\partial t}$ can be derived to

$$\nabla \times (\nabla \times B) = -\Delta B = \nabla \times (\mu_0 j) = \mu_0 \sigma \nabla \times E = -\mu_0 \sigma \frac{\partial B}{\partial t} \quad (2.53)$$

with $\nabla \times B = \mu_0 j$ and $E = \frac{1}{\sigma} j$, being σ the conductivity. Processes dominated by resistivity have long time scales compared to ideal effects with flux conservation. In typical fusion plasmas, the ideal time scale $\tau_{Alfvén} \propto \frac{a}{v_A} \approx 10 \mu\text{sec}$ (v_A , the Alfvén velocity defined in the previous section) is by far shorter than the resistive time $\tau_{Res} = \mu_0 \sigma a^2 = a^2 / D_{mag} \approx 10 \text{ms}$ with σ the conductivity and D_{mag} the diffusion coefficient. The presence of finite resistivity enables the reconnection of magnetic field lines, leading to the formation of the magnetic islands, see Fig.2.14. The center of the island is called the O-point and the point where the field lines cross is called the X-point. The island width is defined as the maximum radial distance within the last closed flux surface, the island separatrix.

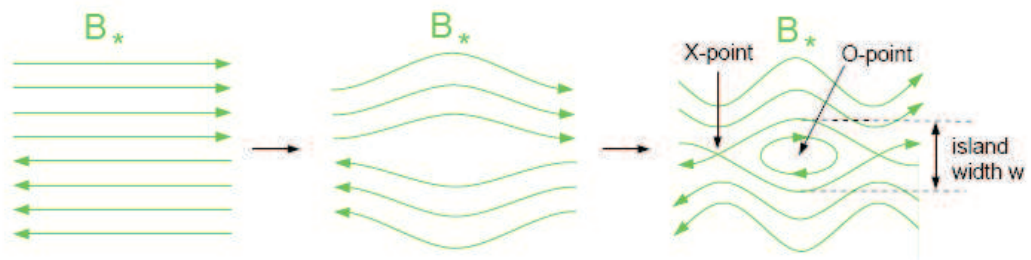


Figure 2.14: Formation of a magnetic island due to field line reconnection of a perturbed magnetic field B_* with the O-point, the X-point and w the width of the island

In a toroidally confined plasma because of the density gradient, more trapped particles exist in the inner part than in the outer part of the banana. In a poloidal cross section this results in a net current in the positive poloidal (counter-clockwise) direction. However the trapped particles have their main velocity component in the toroidal direction resulting in a nearly toroidal current, the so-called bootstrap current which is directly proportional to the total pressure gradient [1].

The most common types of resistive instabilities in high β tokamak plasmas are the Neoclassical Tearing Modes (NTMs). They are responsible for confinement degradation of the plasma since they enhance the radial outwards transport. For these, the magnetic reconnection process allows a local flattening of the pressure profile which leads to a helical hole in the bootstrap current. As already mentioned, NTMs take the form of magnetic islands which occur at surfaces of rational values of $q = m/n$. Their mode structure is conventionally defined in terms of the dominant Fourier component of the island, where m is the poloidal mode number and n is the toroidal mode number. The most common NTM instabilities are found at q -values of 1.5 and 2 for $(m,n)=(3,2)$ and $(m,n)=(2,1)$ respectively. Fig.2.15 shows a $(3,2)$ NTM mode forming three islands in a poloidal cross section. If an island is formed at a rational surface with high pressure gradient, this flattens inside the island.

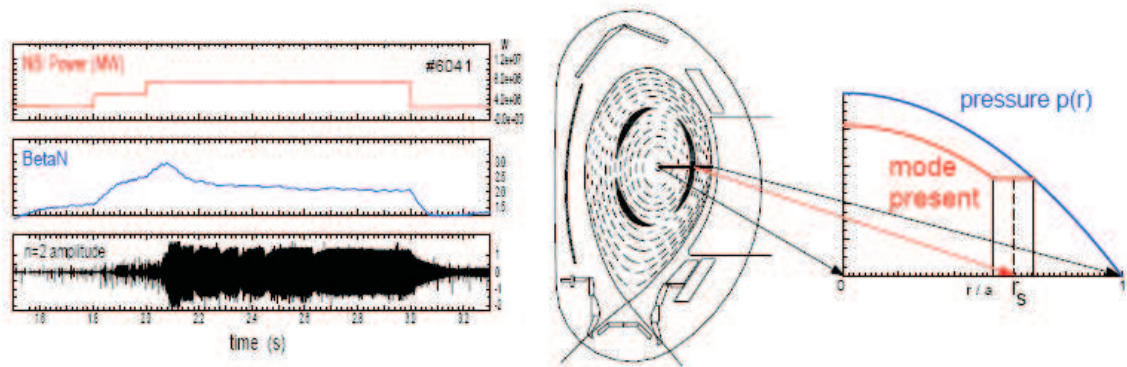


Figure 2.15: Limit in β and pressure degradation due to NTM

$(3,2)$ NTMs can lead to a confinement degradation of 10-30%, while $(2,1)$ NTMs can lead to a confinement degradation of 40-50% and often even to disruptive termination of the discharge at low q_{95} [42].

2.2.4 Edge Localized Modes (ELMs)

In the early 1980s a new regime of high confinement was discovered in the ASDEX tokamak [43]. The improved confinement in this so-called H-mode regime (high as opposed to low in L-mode) is due to a reduced level of heat and particle transport in a narrow region, a transport barrier, at the edge of the plasma. In the H-mode regime a new instability was observed which has its largest amplitude at the plasma boundary. The instability was named edge localized

mode or ELM by Keilhacker et al [44]. ELMs, as they are now commonly known, are characterized by repetitive spikes in the D_α emission indicating a loss of particles from the main plasma arriving at the divertor. The loss of particles is accompanied by a loss of energy at each ELM, of the order of 1 – 10% of the energy stored in the transport barrier (itself about half the total plasma energy). An ELM lowers the density and temperature gradients in a very short time, typically of the order of $200\mu s$. The losses are not limited to the edge pedestal but can be extended up to as much as 20% of the plasma radius from the edge inwards. After this, the ELM disappears, the plasma recovers and the density and temperature gradients build up until the next ELM is triggered. The length of this recovery phase determines the frequency of the ELMs [45]. This depends on how much energy/particle content was lost and the heating power/particle into the transport barrier. The occurrence of ELMs is not necessarily negative. Although ELMs do decrease the energy confinement time, they are beneficial for the control of density and impurities. The electromagnetic perturbations associated with ELMs have been investigated in several experiments (e.g. TCV [46], ASDEX Upgrade [47] and JFT-2M [48]). Generally, a broad turbulent spectrum is seen during the phase of enhanced transport. Often an ELM precursor is observed, mainly as magnetic oscillations with growing amplitude at low or medium mode numbers. The growth time of the precursor oscillations varies and is reported to range from about $50\mu s$ in TCV [46] up to about a millisecond in ASDEX Upgrade [47]. Although low toroidal mode numbers $n = 1, 2$ have been reported for ELM precursors, medium mode numbers in the range of $n \geq 4$ seem to be more typical. From ECE measurements in ASDEX Upgrade, ELM precursors have been found to be radially localized within 10 to 20mm from the separatrix [47], while during an ELM crash a radial range of typically 50mm width is affected on a time scale of less than $100\mu s$. A cold wave is launched by this fast edge temperature drop which typically propagates up to mid-radius.

2.3 Fast Particle Losses due to MHD Activities

2.3.1 Mode-Particle Resonance as a Particle Loss Mechanism

One of the most accepted theories for fast ion losses induced by mode-particle resonance was reported by R. B. White [27] in the early 80's. He carried out the study in a toroidal plasma with a magnetic perturbation rotating toroidally in synchronization with the toroidal precession of trapped particles. The internal kink mode in a fishbone, in particular, is destabilized by trapped particles and so its frequency automatically matches the precession rate of the trapped particles, giving rise to the so-called fishbone instability. The MHD mode produces perturbations of these particle orbits which can have periodic and secular contributions. The second one will be presented in detail here.

Perturbations of the equilibrium magnetic field due to MHD modes can be represented through $\delta\mathbf{B} = \nabla \times \alpha\mathbf{B}$, with α a general function of position. This single scalar function is sufficient to represent exactly the radial field perturbation, δB_r , which dominates the structure of the perturbed magnetic surfaces and is the most important component for the modification of particle orbits. The total electric field in the plasma is given by

$$\mathbf{E} = \frac{\partial}{\partial t} \alpha \mathbf{B} - \nabla \Phi \quad (2.54)$$

with Φ the electrostatic potential. This is, due to the large value of the electron parallel conductivity, perpendicular to the magnetic field. Particles moving in phase with the perturbation experience a secular radial drift:

$$\mathbf{v}_D = \frac{\mathbf{E} \times \mathbf{B}}{B^2}. \quad (2.55)$$

Depending on the phase between the magnetic perturbation and the particle trajectory, the radial drift can be outwards or inwards as Fig.2.16 shows.

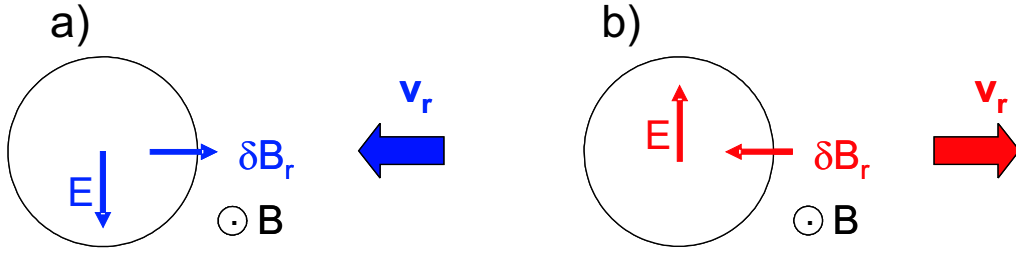


Figure 2.16: Radial drift due to particle-mode resonance interaction. a) Inward radial drift due to $E \times B$ product. b) Outward radial drift due to $E \times B$ product.

This radial drift becomes effective ejecting ions only if both ion and mode stay in resonance long enough and with the right phase. The resonance condition proposed by R. B. White [27] for deeply trapped particles is fulfilled when

$$f_{n,m} = n f_{prec} + N f_b + \Omega \quad (2.56)$$

where $f_{n,m}$ is the mode frequency, f_{prec} the particle precession frequency, f_b the bounce frequency and Ω the plasma rotation frequency, with N an integer and n and m the mode numbers. Since typically $f_b > \Omega + n f_{prec}$, the resonance of lowest frequency is the precession frequency resonance, $f_{n,m} = \Omega + n f_{prec}$.

Now consider passing particles. The resonance condition is given by

$$f_{n,m} = \frac{f_{tor}}{q} (q - m + N) + \Omega \quad (2.57)$$

for all integers $N \neq 0$, where f_{tor} is the toroidal frequency of the passing ions. Since $\frac{f_{tor}}{q}$ is a decreasing function of radius and $q - m - N$ increasing, a resonance can extend over a wide range of r .

The existence of a radial electric field given by Eq.(2.54) modifies the particle behavior thus, the total energy is decreased during outward motion but the kinetic energy may in fact be increased. The total motion can lead to a particle total energy loss which implies an extra amount of free energy available to drive MHD modes.

2.3.2 Orbit Stochasticity

In the early 90's, a non resonant loss mechanism for energetic ions was described in detail for the first time by H. E. Mynick [49]. Fast ions suffer from an stochastic transport induced by low- n magnetic perturbations which lead to their loss. It was shown numerically and analytically that the stochastic threshold of energetic particles is considerably lower than that of the magnetic field. This means that magnetic perturbations could cause appreciable loss of energetic ions without destroying the bulk confinement. Orbit stochasticity is produced by an overlap of islands in the particle phase space. In principle, in a tokamak, a particle confined in an unperturbed magnetic field with low energy will follow the magnetic field lines. However, a particle with high energy ($E \gg 10$ keV) will follow an orbit which is drifted from the magnetic surface due to the drifts present in a tokamak magnetic field. This drift orbit can be illustrated as a drift magnetic surface with symmetry $(m,n)=(1,0)$.

Considering a single harmonic perturbation model of a low-frequency MHD perturbation, e.g. an NTM mode with $(2,1)$ helical symmetry, low energetic passing ions will follow the perturbed magnetic field lines reproducing in a Poincaré puncture plot the structure of the magnetic perturbation. Fast ions will follow as well the perturbed magnetic field lines showing a similar magnetic structure in phase space. However, and of crucial importance to understand the origin of orbit stochasticity is the appearance of two additional rings of islands of symmetry $m=1$ and $m=3$ around the $q=1$ and $q=3$ magnetic surfaces respectively. As the magnetic perturbation increases, the width of these three island rings in phase space increase toward each other, until at a threshold, the islands overlap, and the stochastic loss of the orbits ensues. At the same time, the magnetic plot continues to show the single primary ring of islands of $(2,1)$ symmetry. The combination of the energetic particle drift orbit of symmetry $(1,0)$ with the magnetic island structure, symmetry $(2,1)$, has given raise to a new set of rings of islands with symmetries $(3,1)$ and $(1,1)$ in phase space. The same procedure can be applied to calculate the symmetry of these additional structures for other types of magnetic perturbations. The rules which govern the generation of these new set of islands in phase space were illustrated by Carolipio et al[29]. Fig.2.17.a shows the structure of a $(2,1)$ magnetic island formed by a low passing energetic ion ($E=0.0001$ keV) in a Poincaré plot. The same simulation performed with a deuterium ion of $E=100$ keV gives raise to the additional ring of islands previously mentioned, Fig.2.17.b. As the magnetic perturbation increases, both rings of islands overlap producing the stochastic area in phase space and consequently the fast ion losses.

This loss mechanism is insensitive to the relative mode-particle phase and to the particle pitch angle, but sensitive to particle energies. Moreover, the radial motion is not coherent in nature, as occurs, for example during the trapped particle expulsion by fishbone modes described in the previous section. Rather than resonant, the stochastic radial transport is a diffusive process.

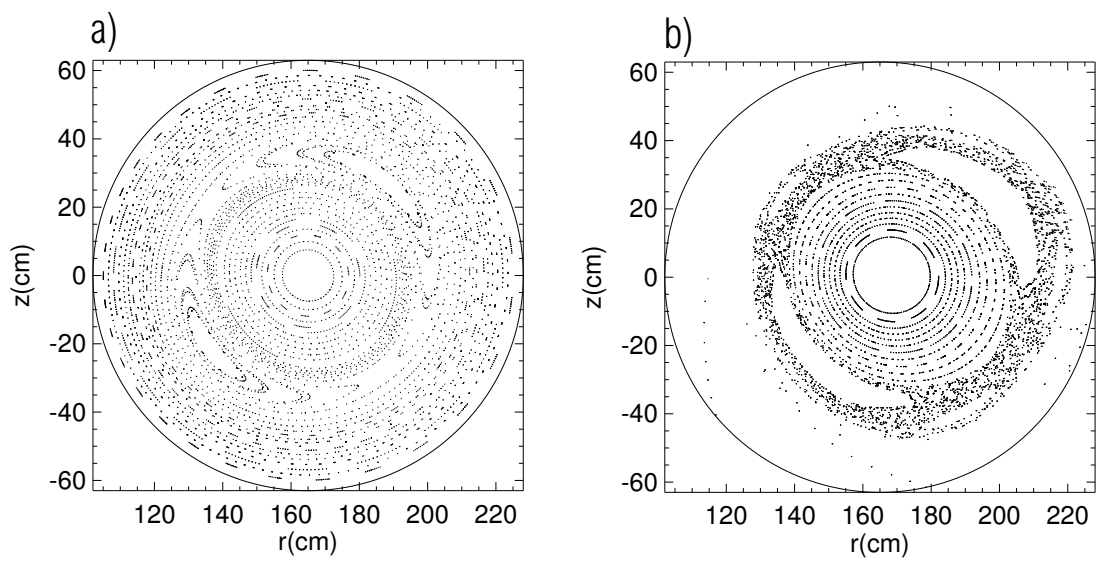


Figure 2.17: Stochasticity theory. a) (2,1) NTM Poincaré plot for passing ions with $E=0.0001$ keV. $R=165\text{cm}$, $a=63\text{cm}$, $\delta B_r/B = 6 \times 10^{-4}$ and $B_0 = 2T$. b) Same plot but for a 100 keV deuterium ion. Additional structures are visible around $q=3$ magnetic surface.

Chapter 3

Experimental Set-Up

3.1 The Fast Ion Loss Diagnostic

The Fast Ion Loss Detector (FILD) developed during this thesis acts as a magnetic spectrometer, dispersing fast ions onto a scintillator, with the strike point depending on their gyroradius and pitch angle. The design is based on the concept of the α -particle detector used for the first time at TFTR [50] and more recently at W7-AS [3]. The detector head consists basically of a 3-dimensional ion collimator, a stainless steel plate coated with the scintillator powder and a graphite cap. The geometry of the collimator has been optimized by simulating typical particle trajectories of interest using the GOURDON code and afterward benchmarked using the Monte Carlo code EfpDesign [51].

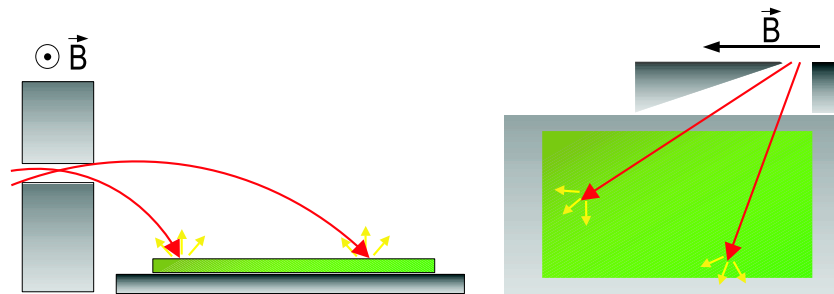


Figure 3.1: A schematic of the top and side view of collimator operation principle, including two fast ion orbits. The gyroradius (energy) of the particle determines how far from the aperture it will strike the scintillator. The pitch angle determines where the ions will strike the scintillator along the orthogonal dimension.

A schematic view of the detector principle is shown in Fig.3.1. The gyroradius of the particle orbit determines how far from the aperture the particle will strike the scintillator. The pitch angle determines where the particle will strike along the orthogonal dimension of the scintillator. The chosen final geometry enables the detection of particles with gyroradius of up to 120 mm and pitch angles ($\arccos(v_{\parallel}/v)$) between 87° (deeply trapped particles) and 30° (passing

ions). The graphite cap shape was calculated by following fast ions backwards in time from the aperture. The final shape was optimized to prevent interferences with the selected fast ion trajectories. One of the crucial decisions concerning the development of a scintillator based detector is the choice of the scintillator itself. It has to fulfill basically three conditions: efficiency, temperature stability and a very short decay time ($< 1\mu s$) to enable the investigation of fast ion losses due to high frequency MHD phenomena. A novel scintillator was found whose optical and physical features are presented in detail in a later section. The temperature of the graphite cap is measured to avoid possible undesirable overheating of the probe. The temperature measurement of the detector head is also necessary since the ionoluminescence of the scintillator depends on its temperature and thus is not constant at temperatures above 400°C . The total particle flux to the isolated scintillator plate is determined by measuring the electric current into it. To exclude artifacts, a hidden second plate, not exposed to ions and isolated from the first one by a ceramic layer, was used as reference.

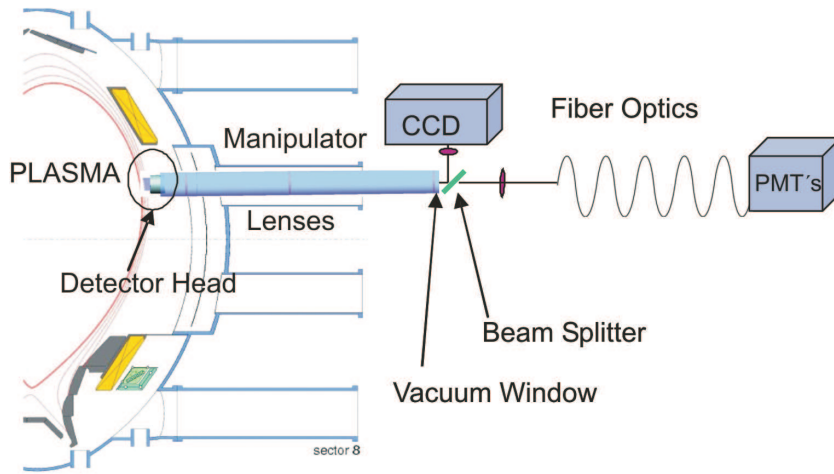


Figure 3.2: An overview of the Fast Ion Loss Diagnostic with a cross-section of ASDEX Upgrade including detector head, lenses relay, CCD camera, optical fibers and PMTs.

In the following sections, the set-up of the lost fast ion scintillator probe will be described in detail. Furthermore, the envisaged performance, the design of the collimator set-up, the choice of the scintillator and the optic system used to transfer the light emitted by the scintillator to the light acquisition systems will be addressed.

3.2 Detector Head Design

The current design of the probe head starts with the study of the best probe positioning inside ASDEX Upgrade. Simulations of particle orbits in non-perturbed magnetic fields as well as in the presence of island-like magnetic perturbations were undertaken in this direction using the HAGIS [39] code for the plasma region inside the last closed magnetic surface and the GOURDON [52] code for the outer region. The ASDEX Upgrade vessel was also implemented. In

this previous work it was concluded that the mid plane manipulator, actually located 300mm above the mid plane, was a favorable poloidal position for the location of the probe since the main losses in the presence of magnetic perturbations appear in this region [4]. The mid plane manipulator allows to vary the distance to the plasma and to find experimentally the most suitable radial position. Actually this is a search for the right balance between high ion fluxes and low heat loads. Fig.3.3 shows a view into the ASDEX Upgrade vacuum vessel, sectors 8-10, with the Fast Ion Loss Detector Head at the mid plane manipulator. Other components important for the operation of the diagnostic are also depicted.

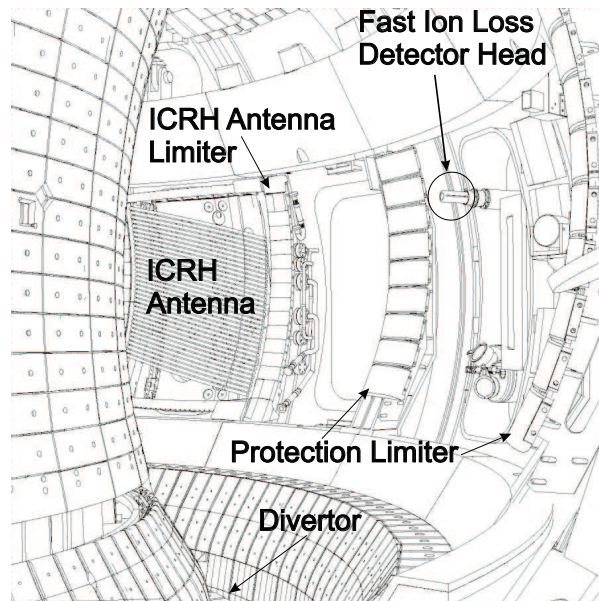


Figure 3.3: CAD view of sectors 8-10 of the ASDEX Upgrade vessel. The manipulator with FILD detector head, ICRH antenna, ICRH antenna limiter and protection limiters are indicated.

The next step was the calculation of the probe head boundary surfaces which allow the detection of ions with velocities almost perpendicular to the magnetic field lines and energies in the desired range. A Monte Carlo simulation code which has been used recently for the design of the escaping ion probe of the Wendelstein 7-AS stellarator and the JET tokamak, EfpDesign [3], was taken to benchmark the detector head geometry calculated using the full orbit code GOURDON. With these codes, the graphite cap boundary shapes and the shape and position of the scintillator have been derived as well as the expected resolution of the system. The latter depends on the combination of the entrance collimator and the scintillator alignment relative to it. After several iterations an optimum collimator set-up has been found, which allows the realization of the desired range and resolution for the selected ions. In Fig.3.4, one can see the simulated trajectories of deeply trapped particles (pitch angle $\approx 88^\circ$) with three different gyroradii, 3, 6 and 9 cm. The particles were started with a random gyrophase within the appropriate cone and with the starting point distributed randomly at the first aperture slit. For this graphite cap geometry one can see that some ions (red trajectories) with a gyroradius of 3

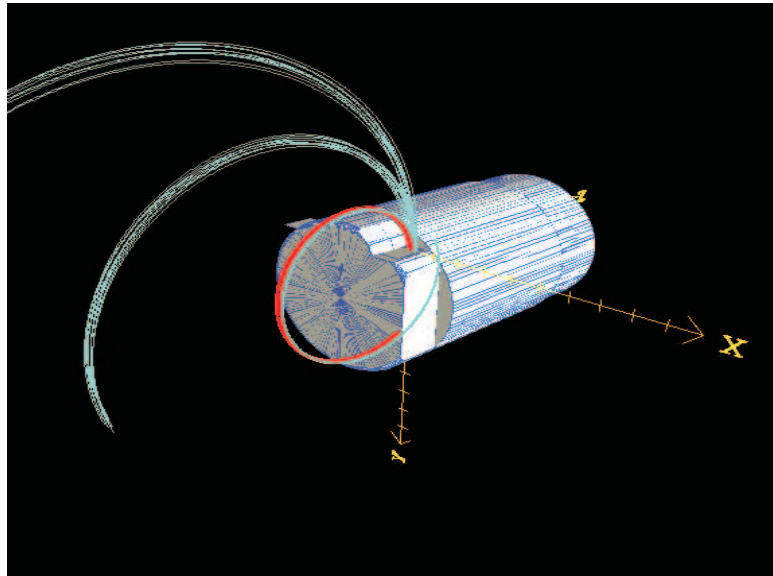


Figure 3.4: Particle trajectories calculated forwards and backwards from the first aperture slit to shape the graphite cap. The start points of the particles were taken randomly distributed over the whole slit. In the same way the particles were started with a random gyrophase within the appropriate cone.

cm and pitch angle of 88° are stopped by the graphite wall before they reach the aperture. The geometry of the 3D-collimator (aperture) was calculated by taking into account the lowest energies (gyroradius) to be measured, the required pitch angles and a reasonable gyroradius and pitch angle resolution. Two different aperture geometries have been used. The first one was optimized to obtain high ion fluxes starting with particle energies around 10 keV. As a consequence, the resolution specially at energies above 50 keV was very poor. The second one was optimized, having in mind a high energy resolution for very energetic ions (ICRH heated ions). The alignment between scintillator plate and aperture was also considered for the calculation of the optimal resolution. In Fig. 3.5 the final detector head is shown without graphite protection. Fig.3.5.a shows a side view of the detector head with the trajectories of particles with three different pitch angles, 87° , 70° and 50° and two different gyroradii, 3 and 6 cm entering through the collimator and hitting the scintillator plate. Fig.3.5.b shows the strike points of these trajectories on the scintillator plate.

The detector response has been modeled numerically using both codes previously mentioned allowing the generation of a mapping between locations on the scintillator and the gyroradius and pitch angles of particles that can hit there. Fig.3.6 depicts the results of such a numerical simulation, showing the resulting grid of centroids in gyroradius and pitch angles at the scintillator. As shown before, the aperture geometry can be optimized for detecting particles in certain pitch angle and energy ranges. The grid shown in Fig. 3.6 was optimized for detecting ICRH heated fast hydrogen and deuterium ions with energies above 200 keV. In order to map quickly energies and gyroradius at a typical magnetic field at the probe, the relation between

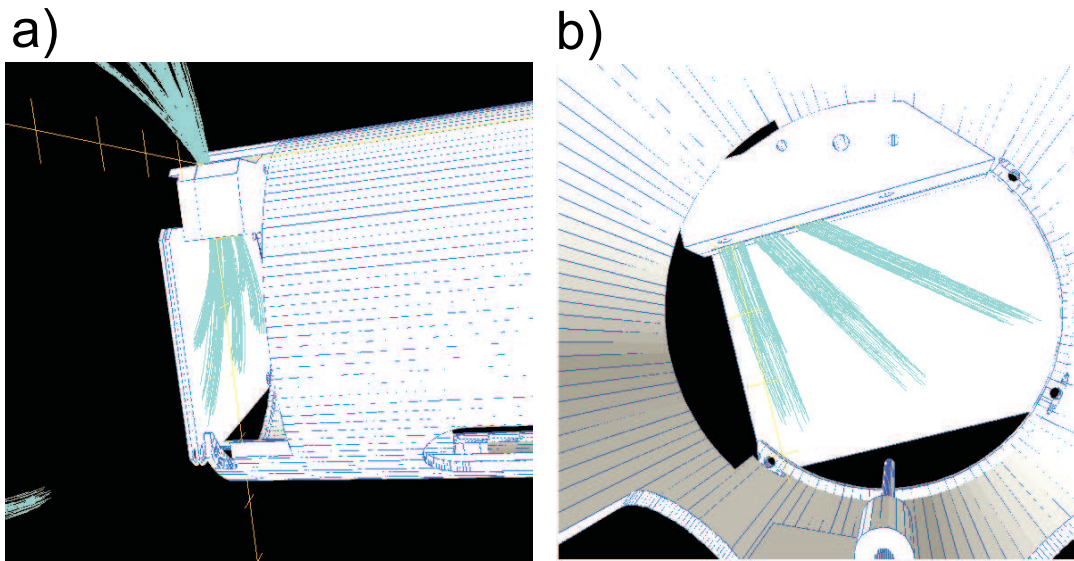


Figure 3.5: (a) Side view of the detector head without graphite cap. Trajectories of particles with three different pitch angles, 87° , 70° and 50° , and two different gyroradii, 3 and 6 cm, entering through the collimator and hitting the scintillator plate are also shown. (b) Inside view of the detector head with the simulated trajectories of particles with pitch angles 87° , 70° and 50° , entering through the collimator and striking the scintillator plate. On the bottom the thermo element is indicated. The particle trajectories were calculated forwards and backwards from the first aperture slit with the starting point randomly distributed over the whole slit.

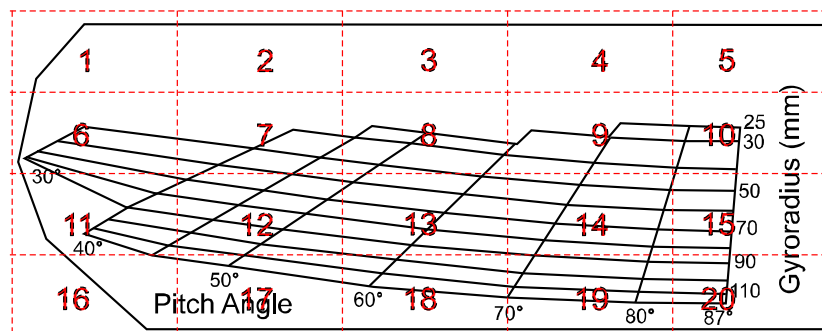


Figure 3.6: The pitch angle and gyroradius centroid grid optimized for very high energetic ions (ICRH). Values of the pitch angles and gyroradii are indicated. The red grid shows the regions on the scintillator to which the corresponding PMTs are sensitive.

both parameters is shown in Fig.3.7.

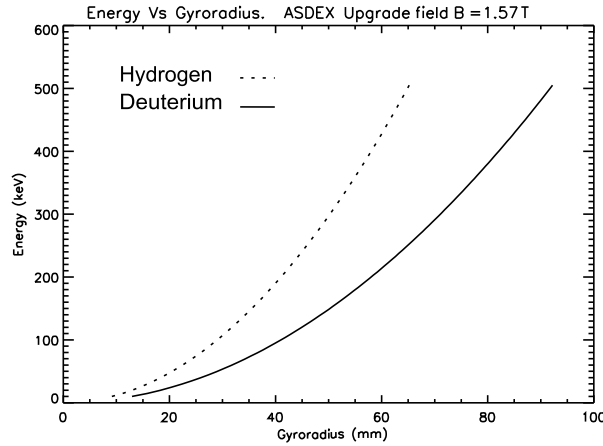


Figure 3.7: Dependence of gyroradius on energy assuming the whole energy as perpendicular kinetic energy, $\rho = \frac{(2E/m)^{1/2}}{\omega_c}$. The curves are calculated for hydrogen and deuterium ions, using a typical magnetic field at the probe $B=1.57T$.

The distributions that arise on the scintillator, as computed by the detector model, for ions at a 70° pitch angle and gyroradii of 30, 40, 50, 60, 70, 80, 90, 100, 110 and 120 mm are shown in Fig.3.8.a. These distributions show the significant broadening that is introduced by the finite size of the aperture. Fig. 3.8.b shows the distributions in pitch angles for particles of a gyroradius of 50 mm.

3.3 The Choice of the Scintillator

The performance of the fast ion loss detector is highly dependent on the scintillator properties. The requirements of a scintillator material to be used in the harsh environments encountered in fusion devices are:

- High sensitivity to the desired particles; in the case of fast ion loss detectors, high sensitivity to α particles and NBI and ICRH heated deuterium and hydrogen ions.
- To exclude measurement distortions, a low sensitivity to other ions, neutrons, electrons and gamma rays is desired.
- It is well known that the sensitivity of scintillator materials depends strongly on the temperature, therefore a stable and linear emission in the desired temperature range (300 – 700K) is required.
- A fast response i.e. short afterglow is strongly recommended to be able to identify the fastest processes which are causing the loss of fast ions.

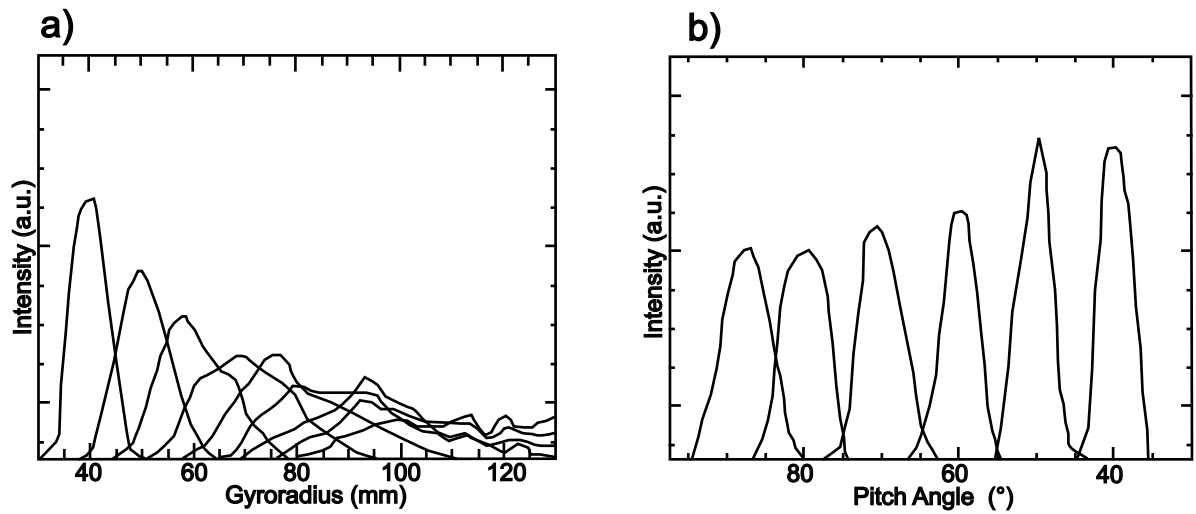


Figure 3.8: (a) The modeled gyroradius centroid distributions for 30, 40, 50, 60, 70, 80, 90, 100, 110 and 120 mm at a pitch angle of 70° . The distributions get broader at large gyroradius because the particles strike the scintillator progressively further from normal incidence, in which case the apertures have less and less collimating effect. The curves represent the result from a numerical simulation of the detector with equal numbers of ions at each gyroradius. (b) The modeled pitch angle distributions for 87° , 80° , 70° , 60° , and 50° at a gyroradius of 50 mm. The curves represent the result from a numerical simulation of the detector with equal numbers of ions at each pitch angle.

- And finally but not less important especially under the extreme conditions expected in a fusion reactor, a minimal mechanical endurance under high temperature and radiation exposure is required.

The choice of scintillator is based on the physical and optical properties supplied by literature and manufacturers i.e. decay time, emission spectrum or excitation spectrum and the results of experiments carried out in an accelerator facility to compare the absolute luminosity of similar material layers. Moreover, in order to quantify the fast ion flux intercepted by a fast ion loss diagnostic, it was found necessary to determine the absolute luminosity of each scintillator screen for high-energy ions ($E > 5keV$).

3.3.1 Scintillation Basics

Luminescence is the non-thermal emission of light by matter, which was excited by an energy absorption process. According to the decay time of the light emission τ after the excitation source has been removed, the luminescence can be subdivided in fluorescence ($\tau \approx 10^{-8}$ s) and phosphorescence ($\tau \gg 10^{-8}$ s). The interactions between the ions penetrating the sample and the sample atoms lead to an energy deposition within the sample with a subsequent generation of luminescence, the so-called ionoluminescence (IL). The main light production process in matter is the ionization of sample atoms due to the energy deposition in the sample. The luminescence can be caused by the sample material itself (intrinsic) or by impurities in the sample (extrinsic), which then acts as a host material for the impurities [53].

Intrinsic Luminescence

The electronic structure of crystalline solids can be described by energy bands, which provide delocalized excited states for electrons. Defect centers (e.g. imperfections in the crystal lattice, impurities) can locally modify the electronic structure of the solid, leading to the presence of localized excited states (e.g. creation of energy levels in the band gap of semiconductor materials by doping). The transitions resulting in intrinsic luminescence can happen from delocalized excited states as well as from localized excited states involving in both cases different processes. The shape and the Full Width at Half Maximum (FWHM) of the peaks and bands in the luminescence spectrum depend on thermal effects (e.g. energy distribution of free charge carriers) and the strength of the interaction between the electrons and phonons, which participate in the optical transition. Assuming low temperatures and weak electron-phonon-interactions the luminescence spectra consist of sharp peaks and narrow bands. Strong electron-phonon-interactions result in a broadening of the peaks and bands in the spectra.

Extrinsic Luminescence

Pure minerals often show no luminescence at all, but impurities even at very low concentrations can cause a remarkable luminescence, when the host mineral is excited. Different types of impurities can be present in the host mineral interacting with each other. Depending

on their behavior in the mineral, the impurities can be subdivided in activators, co-activators (sensitizers) and quenchers [54].

- Activator; an impurity, which causes the luminescence of the host mineral, acts as an activator. It is also called luminescence center (e.g. Mn^{2+} in willemite, Eu^{3+} in apatite).
- Co-activator; sometimes an impurity can only activate luminescence, if another certain impurity is present in the mineral. The latter one is called co-activator or sensitizers (e.g. Pb^{2+} is a co-activator for Mn^{2+} in calcite). The process of co-activation can be explained by an energy transfer from the co-activator to the activator.
- Quencher; sometimes the luminescence of an activator is suppressed (quenched), if another certain impurity is present in the mineral. This impurity is called a quencher (e.g. Fe^{2+} is a quencher for Mn^{2+} in carbonates). The quenching process can be explained by a modification of the energy levels in the host mineral, which makes the luminescence activation very inefficient. In case an activator quenches the luminescence of its co-activator, the activator also behaves like a quencher. At higher activator concentrations the luminescence can be quenched by the activator itself due to resonant absorption processes. This quenching process is called self-quenching.

3.3.2 Characterization of the Scintillator Candidates

The ionoluminescence of several scintillator materials has been quantified by irradiating them with hydrogen ions, deuterium ions and α particles accelerated up to 3 MeV and under various beam currents. In particular we have determined the absolute luminosity in terms of the number of photons emitted per incident ion on thin screens of P43, P46, P56 and TG-Green. The candidate materials have been selected because of their availability, radiation hardness, fast response, prior use in fusion diagnostics or spectral matching to the light detectors (CCDs, and PMTs).

	TG-Green	P46	P43	P56
Composition	$SrGa_2S_4 : Eu^{2+}$	$Y_3Al_5O_{12} : Ce^{3+}$	$Gd_2O_2S : Tb^{3+}$	$Y_2O_3 : Eu^{3+}$
Emission Peak	540 nm	550 nm	545 nm	610 nm
Decay Time	490 ns	70-100 ns	1 ms	2 ms
Density	3.65 g/cm ³	4.57 g/cm ³	7.3 g/cm ³	5 g/cm ³
Particle Size	3-10 μm	3-10 μm	2.5-25 μm	4-10 μm
Manufacturer	Sarnoff Co.	Proxitronic	Proxitronic	AST

Table 3.1: Main features of the scintillator candidates for the Fast Ion Loss Diagnostic for ASDEX Upgrade

The physical and optical properties of the TG-Green (Sarnoff Corporation, USA) scintillator have been studied by Yang [55] for low-voltage cathodoluminescent applications, reporting in

the conclusions a very short decay time, high saturation levels and a high efficiency compared to P43. P43 and P46 coatings were supplied by Proxitronic, Germany. The main features of the P46 scintillator have been reported in previous works, [56] and [57]. The P56 scintillator (AST, England) candidate is already installed in the Fast Ion Loss Detector for the JET tokamak. A detailed study of its internal structure, operating temperature dependence and saturation levels has been reported by Kajiwara [58]. A summary of the main features of these four candidates is presented in Table 3.1.

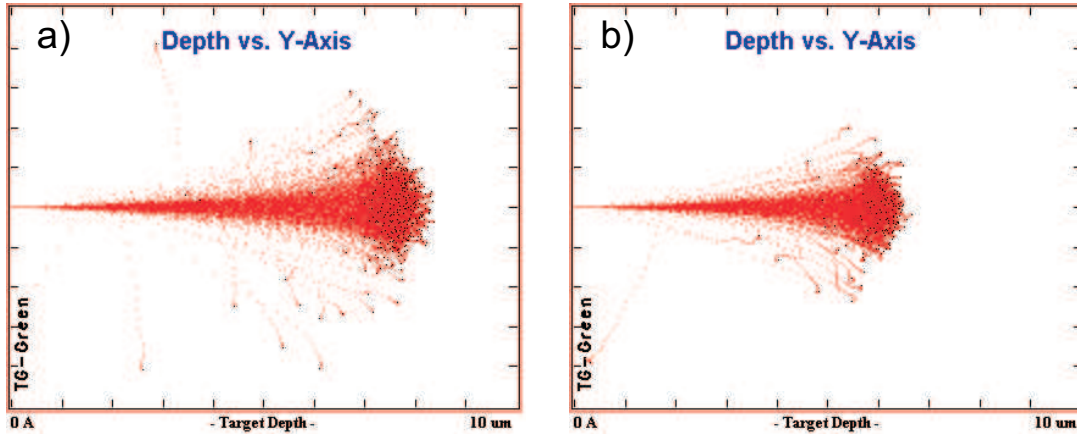


Figure 3.9: Stopping range of a) hydrogen ion and b) deuterium ion beam with 600 keV in a TG-Green scintillator layer with a density of 3.65g/cm^3

The samples were deposited using different processes directly by the manufacturers. The most suitable layer thickness for the densities indicated in Table 3.1 and the desired ions and energy ranges was studied using the SRIM code, [59], which calculates the stopping range of ions (up to 2 GeV/amu) into matter taking into account ion-atom collisions. A too thin layer gives rise to a loss of ionization processes within the phosphor coating and subsequently a loss of light output. On the other hand, a too thick coating leads to a loss of light inside the layer and in addition degrades the saturation levels, charging the phosphor layer and producing consequently arc discharges. Fig.3.9 shows the stopping range of typical ICRH heated hydrogen ions (on the left) and deuterium ions (on the right) with energies of $E=600\text{keV}$ into one of the samples (TG-Green phosphor). As expected, taking into account only kinetic effects, the averaged penetration depth of hydrogen ions ($\approx 7.5\mu\text{m}$) is shorter than those for deuterium ions ($\approx 6\mu\text{m}$) due to the lower mass. Since in ASDEX Upgrade ions with energies over 1 MeV are not expected, a thickness of 20-30 μm , depending on the particle size of the material, was selected.

The measurements were performed at the accelerator facility of the Centro Nacional de Aceleradores (Spanish National Accelerator Center), Seville, Spain [60]. This facility is based around a 3 MeV tandem accelerator (model 9SDH-2 by National Electrostatic Corp., Middleton, WI). The ions generated by their different sources were accelerated towards a 90° analysing magnet before they pass to a general purpose ion beam analysis (IBA) scattering chamber located at the end of the beam line. The entrance to this chamber was equipped with

collimation slits while an insulated chopper was positioned behind them to collect part of the ion beam current. The incident ion flux was determined by integrating this current for 120 s (to improve the statistics). In this way beam currents from 10 nA up to 60 nA for hydrogen ions were produced on the samples, exploiting the capabilities of the accelerator facility. Finally, in order to degrade the ion energy, an aluminised mylar film ($10\mu\text{m}$) fixed on a vacuum indexible holder located inside the IBA chamber was translated into the beam when required. The samples were held on the end of a combined rotary and linear motion feedthrough (model VF-180-3 by Huntington) that was mounted on a second vacuum chamber designed for this purpose [61]. This system permits measurements at different positions across each sample (to check for any variation in light output across the sample) as well as at different screen/incident beam angles. The luminescence light output was measured by PMTs with integrated signal amplifiers (model H5784-04 by Hamamatsu).

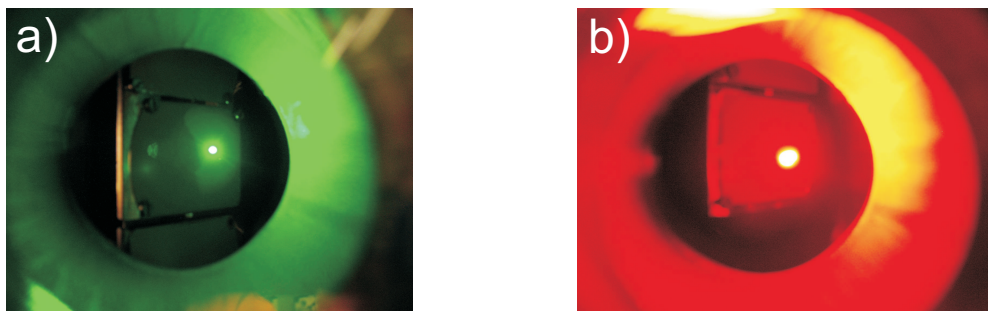


Figure 3.10: View through the vacuum window onto the TG-Green and the P56 scintillator samples irradiated with a deuterium beam with 1100 keV.

3.3.3 Results and Conclusions

The absolute IL of the four scintillator candidates has been studied in order to quantify the fast ion flux intercepted by the fast ion loss diagnostic. In addition, the obtained absolute ionoluminescences together with the main physical and optical features of the scintillator materials have been used to decide which material is the most suitable for the ASDEX Upgrade Fast Ion Loss Diagnostic. In Fig.3.10, a view of the IL produced by the TG-Green and the P56 scintillator coating irradiated with deuterium beam of $E=1100$ keV and recorded by a CCD camera is shown.

The absolute IL and its dependence on the energy of the incident ions and beam currents at various energies are shown in Fig.3.11. Although P46 has a very short decay time, its low absolute IL relative to the other ones excludes it from being the selected scintillator material for the fast ion loss diagnostic. P43 and P56 are known to have a very high efficiency as shown in Fig.3.11, but their extremely long afterglow make them not appropriate for our purpose. Finally, the TG-Green scintillator shows an IL comparable to the most efficient ones, having in addition, as reported in previous works, a very short decay time. As a result, the TG-Green

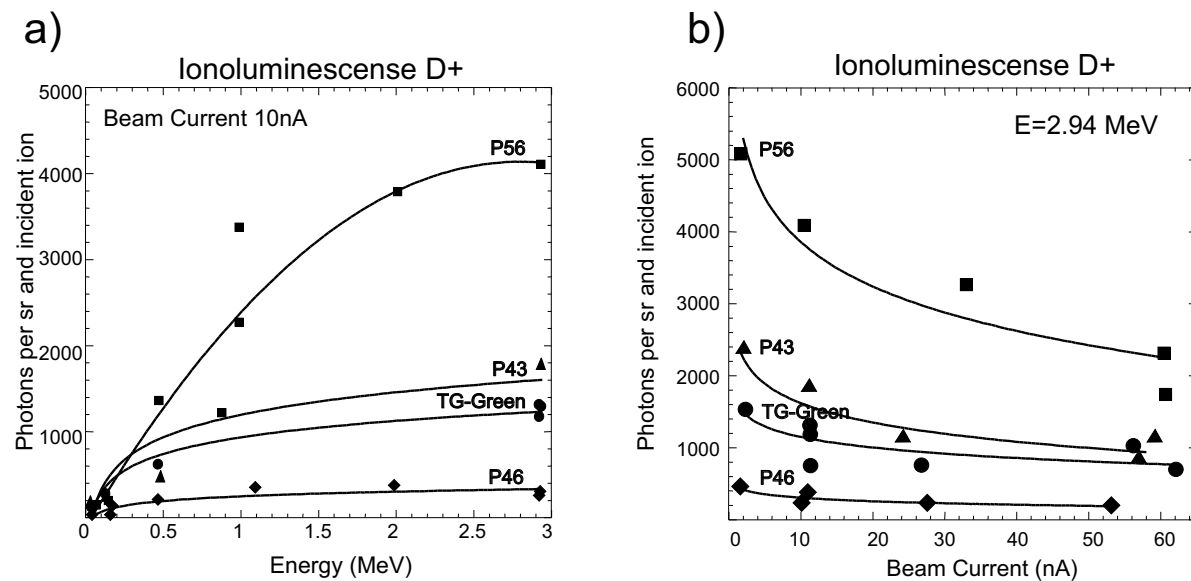


Figure 3.11: Absolute ionoluminescence (IL). (a) Dependence of the absolute IL on the energy of the incident ions with a beam current of 10 nA. The P56 curve was fitted using a second order polynomial while the other curves were fitted with a logarithmic function. (b) Dependence of the absolute IL on the beam current at beam energy of 2.94 MeV. All materials reach the saturation levels following a logarithmic behavior.

scintillator is the most appropriate for our purposes. The study was carried out using various ion beam species e.g. hydrogen ions, deuterium ions and α particles concluding that the total light output depends only slightly on the ion species, probably because the corresponding penetration depths are very similar as shown in Fig.3.9 for deuterium and hydrogen ions. Nevertheless, further experiments are needed to study the IL dependence on temperature environment as well as the degradation of the scintillator efficiency due to neutron fluxes and γ radiation.

3.4 Light Detection and Data Acquisition System

The detector head with the the scintillator is mounted in the front end of a 3000m long and 80mm diameter stainless steel tube, which is a part of the mid plane manipulator (MEM) 3.3. The MEM allows radial movement in the AUG vacuum and close to the plasma edge with a positioning accuracy of ≈ 1 mm, but sets hard constraints to the size of the scintillator and observation possibilities of the emission pattern. A system of optical lenses, described below in more detail, was developed. The lenses relay projects a scintillator image as bright as possible to a suitable place outside the vacuum. A 50/50 beam splitter splits the light into two branches with light detector systems, which complement one another: a CCD camera with a high spatial resolution and a set of 20 photomultiplier tubes (PMTs) with very fast time response ($< \mu$ s), sufficient to follow very fast MHD events. The CCD camera, supplied by Theta System GmbH

has 752 x 290 pixels, binning facilities and a frame rate up to ≈ 100 Hz. It is controlled by a PC and connected to the AFS System and AUG Timing System. The PMTs (Hamamatsu R4220) are located at some distance outside the torus hall, because their response is degraded by the AUG magnetic fields. A 90m fiber optic bundle transfers the light from the image behind the beam splitter to the PMTs. The signal delivered by the PMTs is amplified with 1 MHz bandwidth and digitized with a 14 bit 2 MHz ADC. The data are via a Multichannel High Speed Serial Link transferred to the workstation during the whole discharge, resulting in 800 Mb per shot.

The basic demands for the lens system are the size of the scintillator (50mm x 40mm), the active area and the acceptance angle ($\alpha/2 \approx 12^\circ$) of the selected camera (6.4mm x 4.8mm) and the optical fiber bundle (5mm x 4mm). Accounting for some margin to allow alignment of the system a magnification of $\beta = 1/8.4$ and $\beta = 1/10$, respectively, was chosen. Naturally a solid angle as large as possible, a reasonable number of lenses and a adequate image quality is desired. Since the emission patterns were expected to be rather smooth and wide, no special demands to avoid distortion were considered. Finally, a system with consecutive image diminution by 5 achromatic lenses was regarded as a good compromise Fig.3.12. In fact, lens Nr.5 is double (named Nr.5 and Nr.6), as it is located behind the beam splitter and therefore is present in both branches, providing the necessary individual magnification for CCD-Camera and fiber bundle. The positions and properties of the lenses are given in Table 3.2

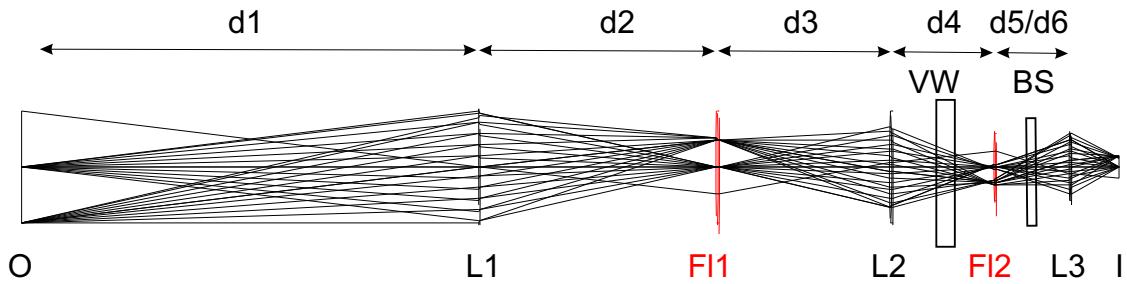


Figure 3.12: Schematic of the full ray tracing of the optical system in the Fast Ion Loss Diagnostic. The main lenses (L1, L2, L3), field lenses (F11, F12), vacuum window (VW), beam splitter location (BS) and the distances between lenses for both systems, CCD camera (d1-d5) and optic fiber system (d1-d4+d6) are depicted, where O is the scintillator plate and I the final image.

	$d1/f(L1)$	$d2/f(F11)$	$d3/f(L2)$	$d4/f(F12)$	$d5/f(L3)$	$d6/f(L3)$
Distance (mm)	1520/500	785/300	565/200	334/120	208/60	241/60

Table 3.2: Distance and focal length of the lenses. $d5, f5$ and $d6, f6$ refer to the last lens in the CCD camera branch and fiber bundle respectively, providing the difference in magnification (β).

The temperature of the graphite cap is measured by a thermo element, see Fig.3.5.b. The

thermo voltage is amplified and digitized with a sampling rate of 250 Hz during the discharge and 5 minutes afterward so that the heating and cooling of the probe is documented. To prevent overheating of the detector head, the thermal emission of the detector head surface is recorded by a camera which views the vessel interior as shown in Fig.3.3. When the emission exceeds a certain level, the additional plasma heating is switched off and the plasma ramped down.

Chapter 4

Fast Particles in ASDEX Upgrade

4.1 Neutral Beam Injection NBI System

A brief introduction to the NBI heating scheme and the underlying physics is presented here. The neutral beam injection heating consists of injecting a beam of neutral fuel atoms at high energy into the plasma. In plasma the beam atoms are ionized through ionization by electrons (dominant only at low electron temperatures of 1 keV), charge exchange (dominant process below 90 keV for deuterium beam), and ionization by ions (dominant process above 90 keV for deuterium beam). In total, these different processes lead to an approximately exponential decay of the beam neutral density along its path.

The energetic neutral atoms are created by extracting positive ions from suitable ion sources, accelerating the ions to high energies, and finally neutralizing the energetic ions by collisions with a gas target in the so-called neutralizer. However, not only hydrogen or deuterium ions are created in the ion source, but also the hydrogen or deuterium molecular ions H_2^+ and H_3^+ or D_2^+ and D_3^+ respectively. These molecular ions are also extracted, accelerated and dissociated in the neutralizer. Hence, the final neutral beam consists not only of neutral atoms with the full acceleration energy, but also of neutral atoms with one half and one third of the acceleration energy. After passing through a magnet, which reflects the non-neutralized ions, the neutral atoms are injected into the plasma through the duct between the beam lines and the torus vessel.

4.1.1 The NBI scheme in ASDEX Upgrade

The NBI system of ASDEX Upgrade consists of two beam lines. Each beam line is equipped with four ion sources. The sources of the first beam line is routinely operated at 55 kV for hydrogen (H^0) and 60 kV for deuterium (D^0), respectively. The sources of the second beam line are upgraded for operation at 70 kV for hydrogen and 100 kV for deuterium respectively. A total power of 14 MW H^0 and 20 MW D^0 can be injected in the ASDEX Upgrade torus.

The species and power distributions of these species depend on the special conditions in the ion source. Different plasma generating methods lead to different electron temperatures and den-

sity profiles in the ion source which influence the species distribution. Typical mean electron energies in a RF source are about 10 eV.

A top view of ASDEX Upgrade is shown in Fig. 4.1, where both injectors are depicted with the corresponding injection geometry of both the radial and the tangential beam lines.

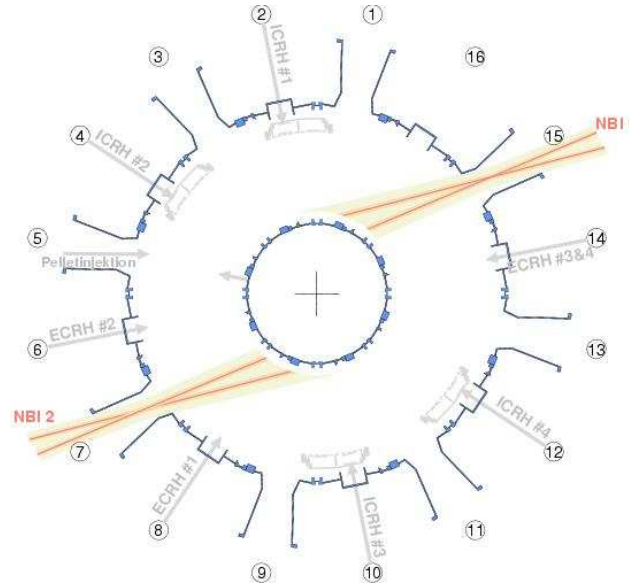


Figure 4.1: Top view of ASDEX Upgrade showing all the heating systems and their toroidal locations. Both NBI injectors, sector 7 and sector 15, are depicted with the two different beam lines, the radial one and the tangential one. Note that the second injection box is located in sector 7 close to the mid plane manipulator as shown in the previous chapter in sector 8.

4.1.2 NBI Fast Particle Population in ASDEX Upgrade.

In order to study the fast particle distribution introduced into ASDEX Upgrade by the NBI system, the ionization pattern of the four beam lines of the second NBI box was simulated using the FAFNER code [62], taking into account the main plasma parameters of a typical discharge. Only one discharge, i.e. magnetic configuration, has been considered, corresponding to NBI co-injection, because it is the most common in a typical ASDEX Upgrade discharge.

The ionization profiles were calculated for 10.000 ions with the three energy components and the real geometry of the different beam lines. The deposition patterns as a function of the major radius R for the four beam lines of the second injector are shown in Fig. 4.2. Most of the particles get ionized just after they enter into the plasma following an e-fold decay with the R coordinate:

$$I = I_0 e^{-R/\lambda}, \quad (4.1)$$

where I_0 is the initial intensity of the neutral beam and λ the mean free path length for ionizing collisions.

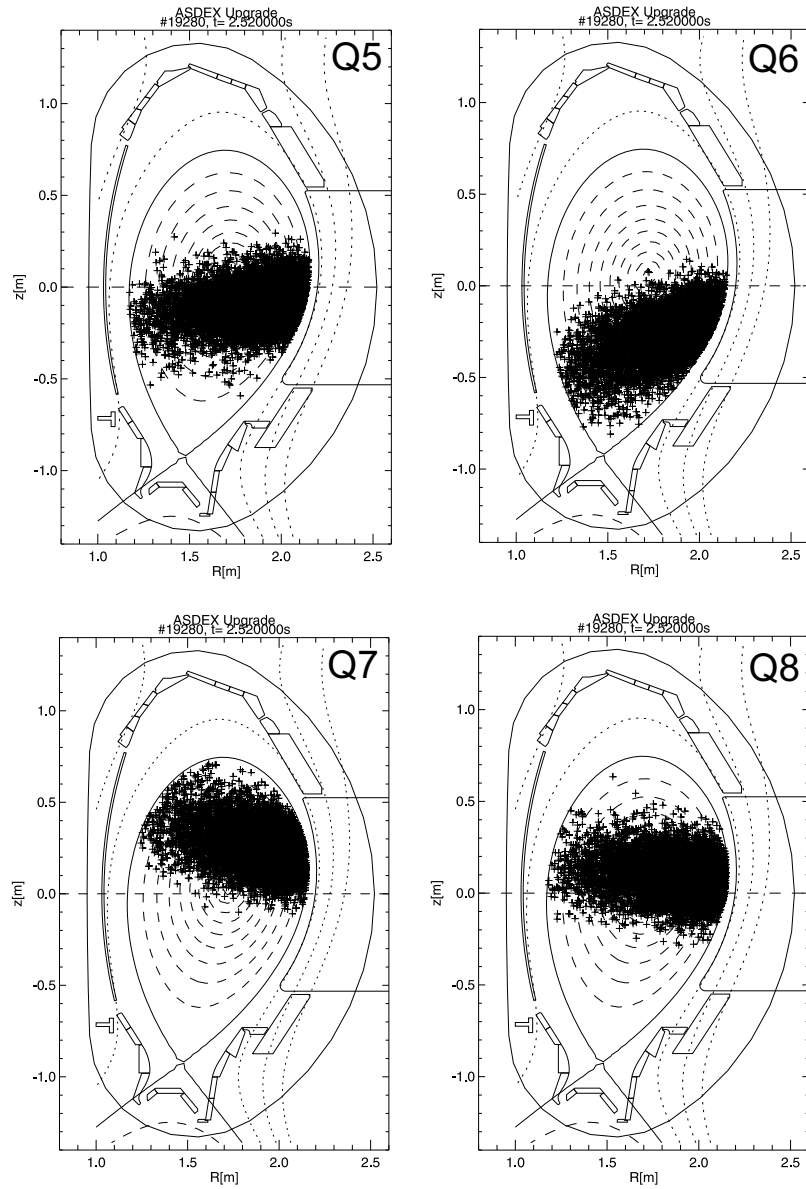


Figure 4.2: Ionization pattern on an ASDEX Upgrade cross section for the four beams of the second injector. Calculations were done with the FAFNER code using a background plasma density of $n=8.4 \cdot 10^{19} m^{-3}$ and the magnetic equilibrium of the discharge 19280 at $t=2.52s$.

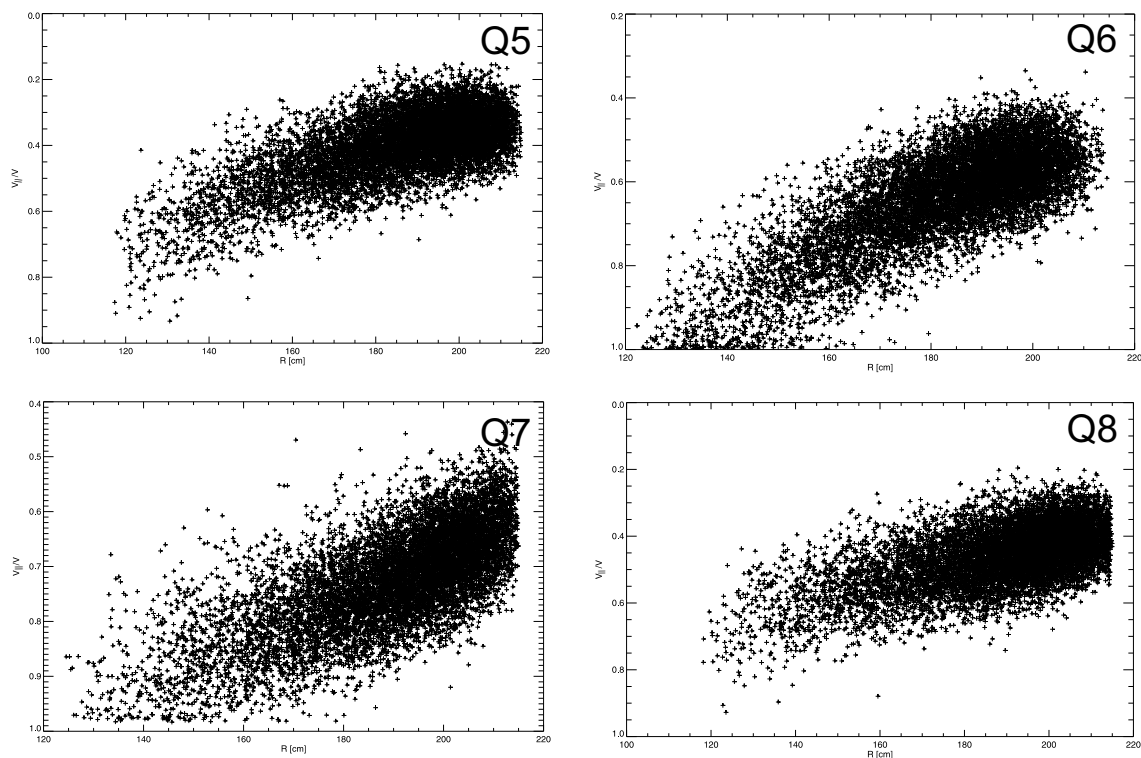


Figure 4.3: Pitch angle distribution of the ionization pattern as a function of the major radius, R . Calculations done with the FAFNER code using a background plasma density of $n=8.4 \cdot 10^{19} m^{-3}$ and the ASDEX Upgrade magnetic equilibrium of the discharge 19280 at $t=2.52s$.

It is important to point out that Q7 and Q8 inject the neutrals above the mid plane while Q5 and Q6 do it below the mid plane. This fact influences directly the escaping toroidal and poloidal location of the prompt losses. As mentioned in Chapter 2, all external heating systems introduce a strongly anisotropic pitch angle distribution of fast ions in the plasma. The NBI heating system generates an anisotropy in the pitch angle distribution which depends on the beam line geometry and injection direction. As Fig.4.3 shows, the more radial sources, Q5 and Q8, deposit neutrals which get ionized with a higher perpendicular component of the velocity than the parallel sources, Q6 and Q7. This leads to a broader population of fast ions on trapped orbits due to the radial sources Q5 and Q8 than due to the tangential ones Q6 and Q7. Nevertheless, there is also a certain amount of neutrals injected by the radial sources which get ionized at the high field side (HFS) crossing the whole plasma with a high parallel component of the velocity. In this case due to the curvature of the field lines at the HFS also the radial sources can be a source of passing ions.

This resulting pitch angle anisotropy and (R,z) deposition pattern will be crucial to understand some of the results presented in the following chapters.

4.2 Electromagnetic Wave Heating

As an auxiliary heating system, radio frequency (rf) electromagnetic waves have been used successfully in several fusion devices. Since the rf heating feasibility and efficiency substantially depend on the capability of the wave to propagate inside the plasma and on the wave-particle interaction mechanism, not all rf frequencies are viable. In general, there are three main ranges of frequencies: ion cyclotron frequency (30-80MHz), lower hybrid frequency (several GHz) and electron cyclotron frequency (several tens of GHz). The rf power is transferred from the generator to the plasma chamber through specially dimensioned low loss transmission lines and is coupled to the plasma by means of antennas, the dimensions and design of which depend on the frequency and on the polarization of the wave to be launched. The antenna couples to a wave that can propagate in the plasma such that all the incoming wave power is launched into the plasma. There are two mechanisms through which the externally launched waves loose energy inside the plasma. The first is by energy transfer to another propagative wave, this process is called mode-conversion. The second one is through direct energy absorption by particles in resonance (either Cherenkov or Cyclotron) with the waves. In the latter case, as a consequence of the interaction with the waves the particle distribution function deviates from a Maxwellian.

4.2.1 Ion Cyclotron Resonance Heating Scheme in ASDEX Upgrade

The Ion Cyclotron Resonance Heating (ICRH) system in ASDEX Upgrade consists of a set of 2 generators, equipped both with two antennas designed to provide waves in the frequency range of approximately $\omega \in [30, 40]$ MHz, matching the fundamental ion cyclotron resonance for Hydrogen ions in a typical ASDEX Upgrade magnetic field.

A particle is in resonance with the wave when in the particle frame of reference the left component of the wave electric fields rotate at the ion gyro-frequency or at its harmonics:

$$\omega - k_{\parallel} v_{\parallel} \approx n\omega_c, \quad (4.2)$$

where v_{\parallel} is the component of the particle velocity parallel to the confining magnetic field, ω_c is the angular cyclotron frequency, ω gives the wave frequency, f , through $\omega = 2\pi f$ and k_{\parallel} is the parallel component of the wave vector. There can be a net energy transfer from waves to particles also at the first harmonics ($n=2$), if the Larmor radius of the particle orbit ($\rho = v_{\perp}/\omega_c$) is comparable with the perpendicular component of the gradient of the wave electric field ($\rho k_{\perp} \gg 1$). In fact, as shown in Fig. 4.4 in the case of $\rho k_{\perp} \ll 1$ the energy gained by the particle in the first half turn is lost in the second half. This is not the case when the magnitude of the wave field varies in the space scale of the Larmor radius.

Since the toroidal field falls off as R^{-1} , the ion cyclotron resonance is localized at a value of R for which the wave frequency, ω , satisfies $\omega = \omega_c(R)$. The resonance width is subject to Doppler broadening, resulting in a resonance width

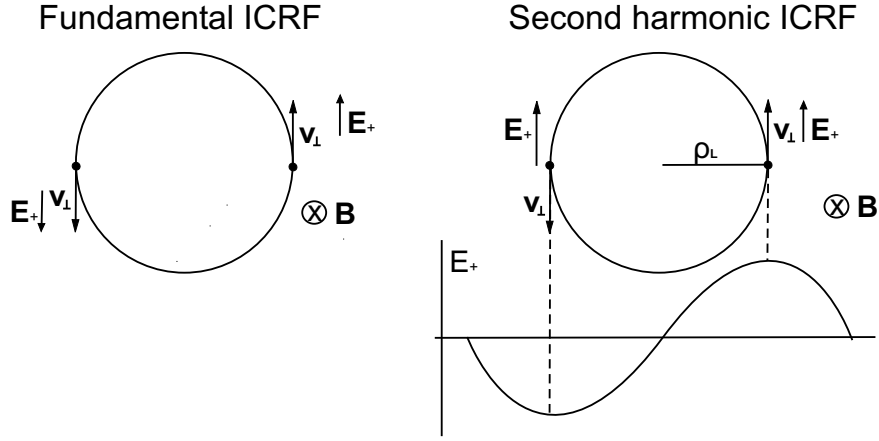


Figure 4.4: Schematic of the ICRH operation principle. At the fundamental, left, a wave acceleration takes place over the whole ion orbit. At the second harmonic, right, both acceleration and deceleration by the wave take place along the ion orbit. A net acceleration occurs only if the wave amplitude is not constant, a gradient is necessary.

$$\delta x = \frac{k_{\parallel} v_{Ti}}{\omega_c} R, \quad (4.3)$$

small compared to the minor plasma radius. For heating at the n -th cyclotron harmonic, the energy increase averaged to the time spent by a not too fast particle in the resonance layer is of the form:

$$\langle \delta W \rangle \propto \left| J_{n-1} \left(\frac{k_{\perp} v_{\perp}}{\omega_c} \right) \right|^2 |E_+|^2 \quad (4.4)$$

where E_+ and E_- are, respectively, the left-hand and right-hand components of the electric field and J_n the Bessel functions. In particular one gets for the

$$\textit{Fundamental} : \quad \langle \delta W \rangle \propto |E_+|^2 \quad (4.5)$$

$$\textit{Second Harmonic} : \quad \langle \delta W \rangle \propto \left| \frac{k_{\perp} v_{\perp}}{\omega_c} \right|^2 |E_+|^2 \quad (4.6)$$

$$\textit{n-th Harmonic} : \quad \langle \delta W \rangle \propto \left| \frac{k_{\perp} v_{\perp}}{\omega_c} \right|^{2(n-1)} |E_+|^2. \quad (4.7)$$

A first conclusion to be drawn from these expressions is that, as $k_{\perp} \rho_L$ is a small quantity, the averaged energy increase decreases strongly with the harmonic number. Second, at the fundamental resonance the interaction with the waves involves mainly the ions of the thermal bulk. On the contrary, harmonic heating tends to accelerate more the faster particles, i.e. particles with $k_{\perp} \rho \gg 1$. As a consequence, harmonic heating tends to create tails at higher

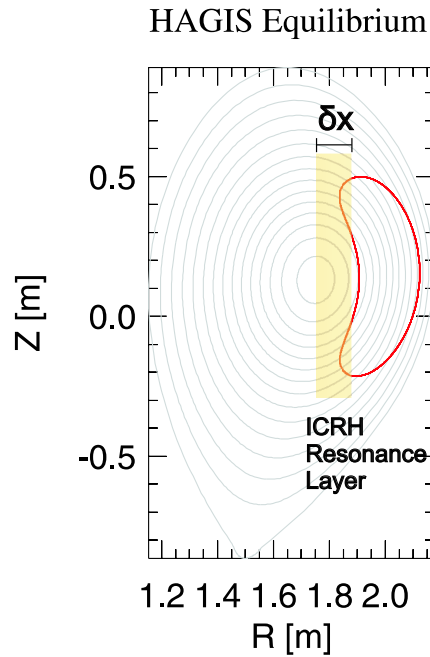


Figure 4.5: ICRH Resonance Layer Width and a typical banana orbit being heated by the ICRH heating system.

energy than fundamental heating. Consequently, the harmonic heating can be enhanced in presence of fast ions produced by NBI.

The Minority Heating Scheme

To determine the strength of the cyclotron damping also the polarization of the wave in the vicinity of the resonance has to be included. Usually in a plasma, the damping at the fundamental resonance is small due to the unfavorable polarization which is determined by the bulk of the plasma. The damping has, therefore, its maximum at the second harmonic and decreases to higher harmonics. However, if the plasma consists of another species i.e. with different Z/A , of low concentration, say the omnipresent hydrogen in a deuterium plasma, absorption at the hydrogen resonance becomes very strong. This is possible because in the vicinity of hydrogen resonance a considerable fraction of the wave power is left circularly polarized because the polarization is determined by the deuterium majority. This scheme is called minority heating. Since all the power is absorbed by the minority ions, a strong tail in the distribution function is created. The energies are quite higher than the critical energy, E_c , so that the tail relaxes mostly due to collisions with electrons and therefore without pitch angle scattering. For higher concentration of the second species the beneficial effect on the polarization in the vicinity of the resonance of the second species decreases and so does the damping.

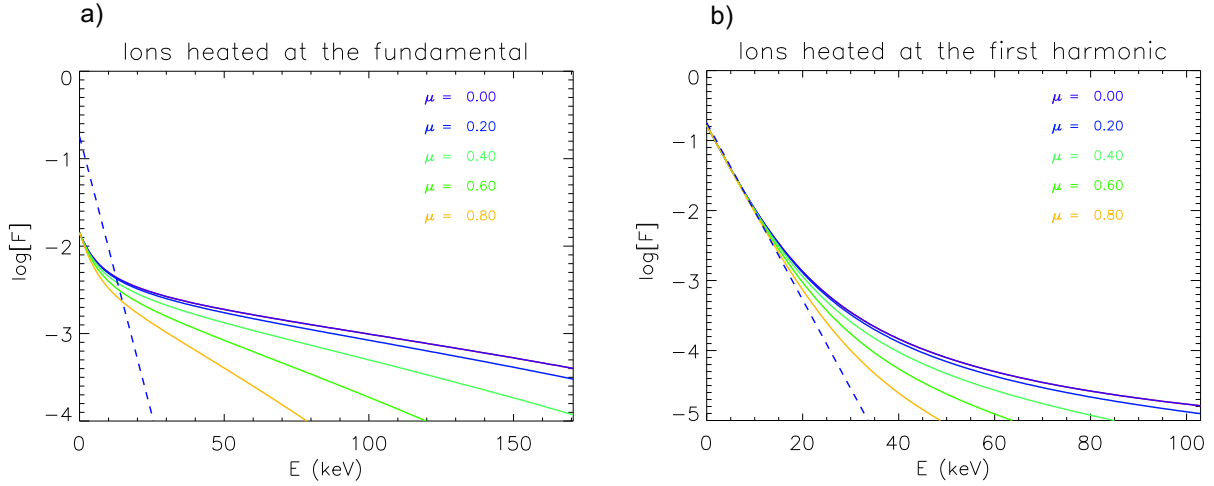


Figure 4.6: Fast Ion Distribution Function for various pitch angles, $\mu = \frac{v_{\parallel}}{v}$, created by the ICRH system for discharge 21011 at Fundamental (Hydrogen) and First (Deuterium) Harmonic heating. The Maxwellian distribution is depicted by the dashed line

4.2.2 ICRH Fast Particle Population in ASDEX Upgrade

The wave propagation and absorption in ASDEX Upgrade is estimated with the full-wave TORIC code [63] while the collision relaxation of the rf generated ion population is calculated with the SSFPQL code. The latter code solves the Fokker-Planck equation in presence of the wave terms, in particular it looks for the steady state resulting from the balance between the wave terms which try to create a plateau at high energies and collisions which try to re-establish the thermal equilibrium represented by the Maxwellian.

The calculations for one discharge relevant for the explanation of the results in a later chapter are shown here, placing emphasis on the pitch angle anisotropies introduced by this heating technique and the covered energy ranges. The contribution of the fundamental harmonic and the first harmonic heating to the fast ion distribution at different pitch angles are shown in Fig.4.6 compared to a typical Maxwellian distribution (dashed line). The calculations have been done for a typical discharge with central ICRH heating to optimize the heating efficiency. As described before the hydrogen ion heating at the fundamental is more efficient than the deuterium ion heating at the first harmonic without additional NBI heating. But in a discharge with additional NBI heating, this result changes completely so that the deuterium heating at the first harmonic can be significant and comparable with the heating of hydrogen ions at the fundamental. It is important to remark that the ICRH heating introduces not only an anisotropy in the pitch angle distribution, but also an inhomogeneous radial distribution of fast ions by means of the width of the ICRH resonance layer, leading to pressure gradients which can be the source of new MHD instabilities.

Chapter 5

Experimental Results

The energetic ion loss diagnostic for ASDEX Upgrade has been operated during one campaign with the full features described in Chapter 3. The results have revealed the high diagnostic potential of this method for a better understanding of wave-particle interactions. In general, the interpretation of the data is complicated due to ion orbit shadow effects of in-vessel components and the high variety of MHD events present in the studied plasmas. In this chapter, the most relevant results are presented, classified according to the MHD activity involved in the ion loss process together with a first section dedicated to a validation of the detector head geometry. The discussion of the physics mechanisms behind the observations will be presented in the following chapter.

5.1 Benchmarking of FILD by First Orbit Losses

First orbit losses, also called prompt losses, are a very suitable tool for checking the design and functionality of the detector head and measuring systems. Fluxes from prompt losses of NBI2 arise directly in front of FILD and yield very intense signals. The four sources of the NBI2 system have different injection energies and geometries (see Chapter 4) and therefore they produce ion losses with specific energies and pitch angles. They can be clearly identified in the emission patterns, allowing in situ calibrations of energies and pitch angle scales.

Neutrals injected more radially result in ion loss spots with the NBI source corresponding energy and higher perpendicular velocity component, than those injected more tangentially. In fact, all sources can be clearly identified in FILD by their prompt loss pattern. Fig.5.1 shows a CCD view of the light pattern generated by fast ion impacts on the scintillator plate due to first orbit losses from NBI source numbers 7 and 8. As expected, the more tangential source (number 7) produces a bright light spot in the phase space area corresponding to higher parallel components of the velocity than the more radial source (number 8). As described in Chapter 4, each NBI source injects neutrals with three energy components corresponding to the full, one half and one third of the acceleration energy. With the aperture geometry used during this campaign, the full energy component ($E=93$ keV, $\rho \approx 40$ mm at $B_{FILD} \approx 1.6$ T) of the second box NBI sources is separated from the second energy component (≈ 45 keV), which

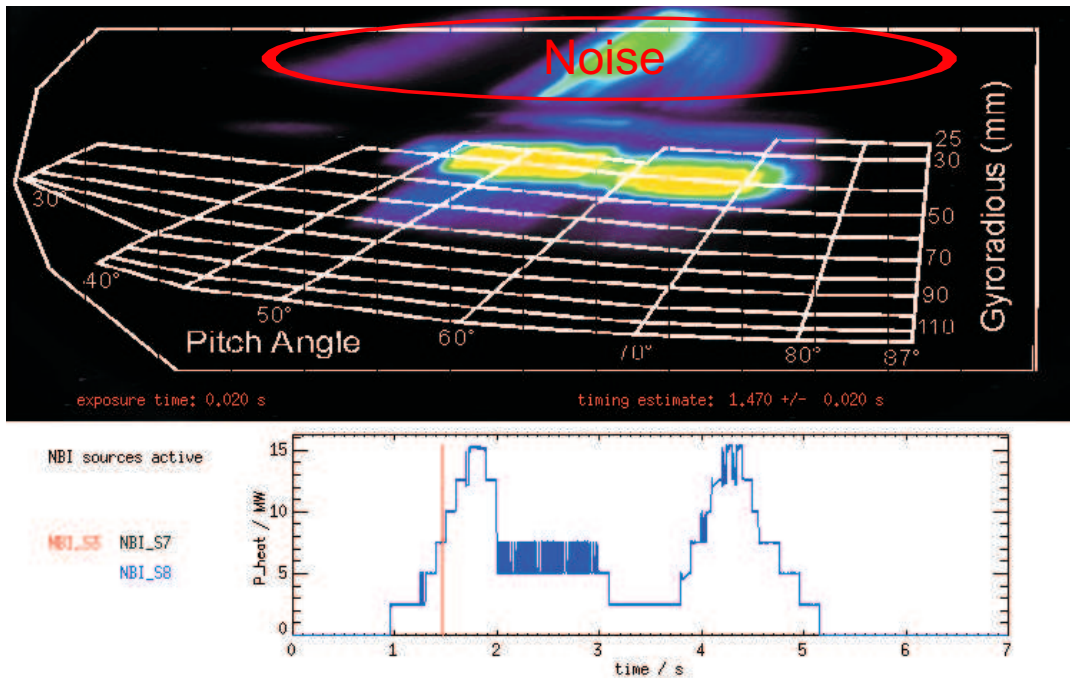


Figure 5.1: AUG Discharge 21168: CCD view of the light pattern produced by ion impacts on the scintillator plate due to first orbit losses together with the borders of the scintillator plate and the energy-pitch angle grid (in white). Two clear spots at a gyroradius of 40 mm and two different pitch angles, 50° (NBI 7) and 65° (NBI 8) are visible. On the bottom a time trace of the NBI heating is depicted, showing the NBI sources active at this time point. The exact time at which the frame was recorded is depicted in red as well as the exposure time of the camera.

is only marginally allowed as the narrow light spots outside the energy-pitch grid shows. The third energy component (≈ 30 keV) is completely suppressed by this collimator geometry. The spots at the upper edge of the figure, encircled by a red line, result from particles which reached the scintillator through unintended narrow gap in the detector head.

Simulations performed using the HAGIS code [39] to calculate the prompt loss pattern of the NBI source number 5 with the full energy component are in agreement with the prompt loss pattern obtained experimentally during this thesis, [4]. In this case, the NBI source number 5 produces a light pattern of prompt losses on the scintillator plate at gyroradius ≈ 40 mm and $\arccos = v_{\parallel}/v \approx 75^{\circ}$ with a $B_{FIELD} \approx 1.6$ T.

In the investigations of core related losses, the first NBI box, placed toroidally opposite to the second box, was preferentially used because the blending of the desired core loss signals with the strong prompt losses, which come mostly from NBI box 2, is avoided. In addition, a very narrow optical filter for the wavelength of the scintillator emission was used during a few discharges to eliminate the possibility that the detector was measuring light coming from the plasma through the aperture.

5.2 ELM Induced Fast Ion Losses

Time resolved ELM induced fast ion losses have been directly observed for the first time in a fusion plasma device by this diagnostic. The highest fluxes of fast ion losses correlated to the D_{α} signal appear mainly due to first orbit losses from the adjacent neutral beam injector box. In this case ELM modulated ion losses are related to ions created in the limiter shadow or edge plasma directly in front of the NBI box. These high energy ionized particles follow the slightly deformed field lines by the ELMs and strike the detector head due to their large gyroradii. In a lower order of magnitude but also appreciable, ELM induced fast ion losses have been observed in discharges with only box 1 NBI heating. In this case not all sources of box 1 have been identified, because of orbit shadow effects of the in-vessel components and of the well defined toroidal localization of the NBI prompt losses away from the detector position. In addition, the occurrence of ELM modulated prompt losses from box 1 depends strongly on the shape of the plasma i.e. triangularity, suggesting that only for specific plasma shapes particle trajectories can avoid the protection and ICRH limiters hitting so the FIELD head.

In Fig.5.2, time traces of three FIELD channels in discharge 21053, representing different energies and pitch angles, are shown along with the divertor D_{α} signal, the stored energy, NBI heating and the magnetic perturbation measured by the pick-up coil close to the mid plane manipulator. The observed energy ranges lie within the injection energies of the NBI system i.e. up to 93 keV. The pitch angle of the lost ions depends directly on the NBI source, which is generating those ions, covering a wide range from deeply trapped to passing orbits. Not every ELM produces the same spikes in phase space. This means that different ELMs eject particles with different energies and pitch angles, depending most likely on their actual characteristics. Looking in more detail, one finds that a fraction of the fast ions is lost in a very short pulse immediately after the onset of the ELM turbulence seen by magnetic pick-up coils.

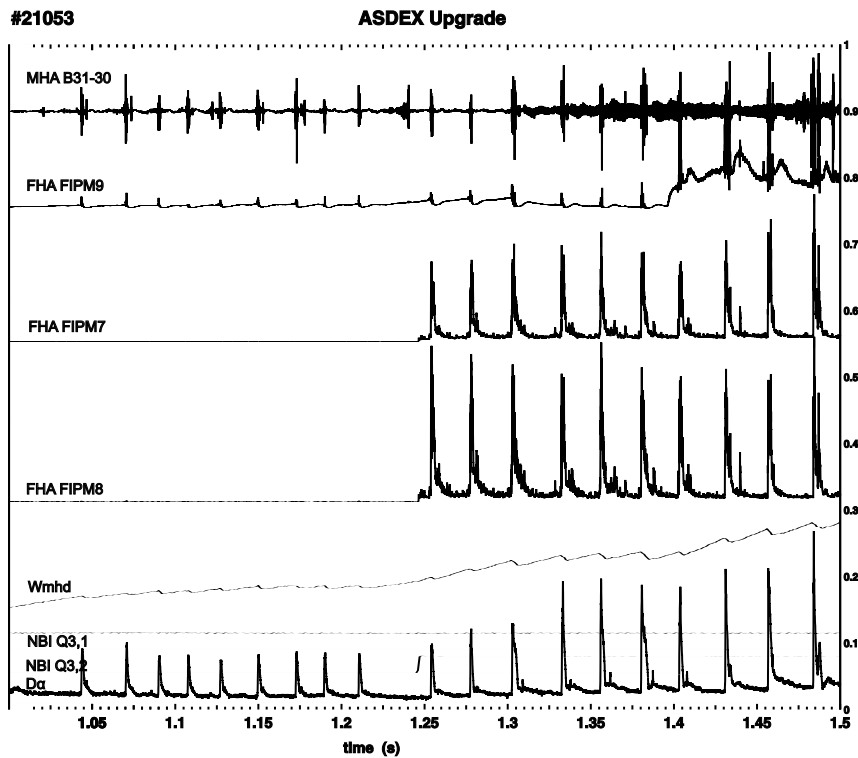


Figure 5.2: AUG Discharge 21053: Overview of ELM evolution observed by three FILD channels (FIPM7, FIPM8 and FIPM9), the divertor D_{α} signal, the magnetic perturbation (B31-30) and the stored energy (Wmhd). The NBI source Q3,1 is active during the whole time windows while the Q3,2 is switched on at $t \approx 1.24$ s.

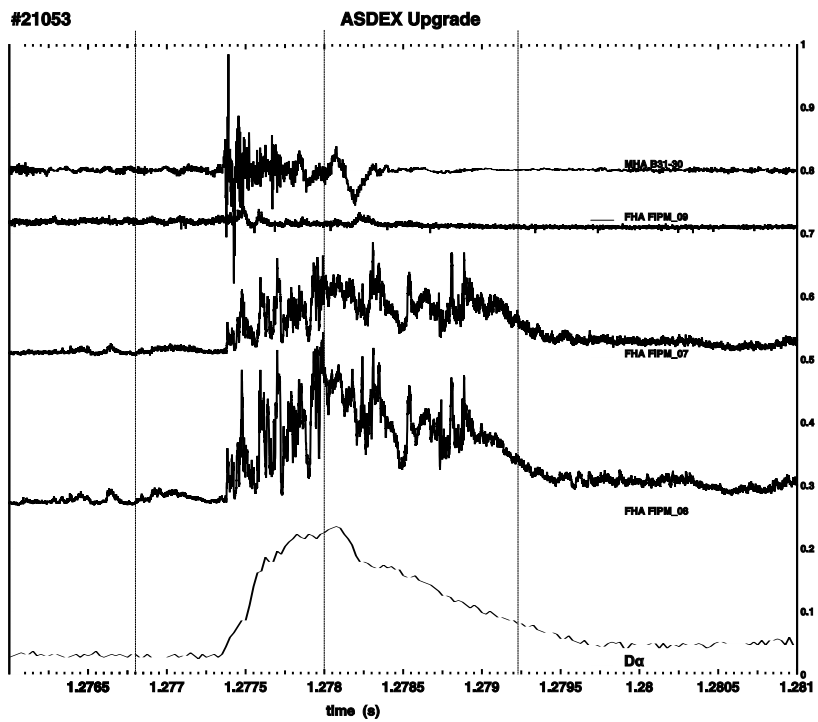


Figure 5.3: AUG Discharge 21053: FILD time resolved view inside one ELM. Three FILD channels (FIPM7, FIPM8 and FIPM9) are plotted together with the divertor D_{α} signal and the magnetic perturbation (B31-30).

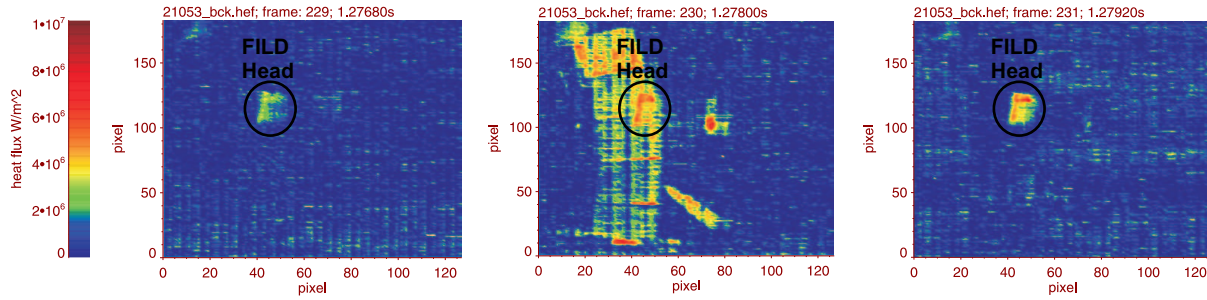


Figure 5.4: AUG Discharge 21053: Infrared view of FILD head at three different time points; before the ELM crash, in between and at the end of the ELM shown in the previous figure.

Looking within one ELM, in this case with NBI box 1 heating, Fig.5.3 shows a correlation of the complicated internal substructure of the magnetic perturbation signal from a pick-up coil located close to FILD with three FILD channels which cover various energies and pitch angles. Depending on the ELM substructure, even several spikes occur during one ELM. Fig.5.3 shows several fast ion pulses correlated with sub-structures in the magnetic signal. The divertor D_α signal plotted in addition shows that fast ion loss bursts occur not only during the magnetic turbulence phase but also during the decay phase of the D_α signal. Furthermore, the lost ion signal presents a modulation through a turbulence behavior during the whole ELM. Whether the spectral change over the fast ion loss spikes is just random or indicates a systematic trend during the ELM remains to be investigated. Although in Fig.5.2 no ELMs appear visible by FILD in the early phase with only NBI1 heating because of the high fluxes generated by NBI box 2, Fig.5.3 illustrates the effect of one ELM on the fast ion population created by the NBI1 system at $t \approx 1.2s$. In parallel, investigation of heat loads to adjacent limiters and to the probe head using an infra-red camera [A.Herrmann, EPS2005] have revealed similar time behavior of ELM induced energy losses, but without any other assertion on their energy or pitch angle than the correlation of the signal with the active NBI sources. Fig5.4 shows, for the same ELM event, the difference in heat load on the FILD head measured by the infrared camera within ELMs in comparison to phase space spectra of the lost ions measured by FILD.

5.3 NTM Induced Fast Ion Losses

A loss of fast ions was observed in specific phase space ranges in the presence of classical as well as neoclassical tearing modes (NTMs). Results obtained during (2,1) and (3,2) NTM activity in different scenarios are presented within this section. In H-mode, NBI heated discharges with NTM activity present, a loss of fast ions occurs with such a high parallel component of the velocity that they are assumed to leave the plasma on passing orbits. In improved H-Mode or in general in discharges with mixed heating, ICRH and NBI, losses appear to be more effective in the phase space region corresponding to deeply trapped ions. On the other hand, an enhancement of fast ion losses on passing orbits has been observed in NTM discharges with additional ICRH heating. ELMs have been observed to disturb the correlation

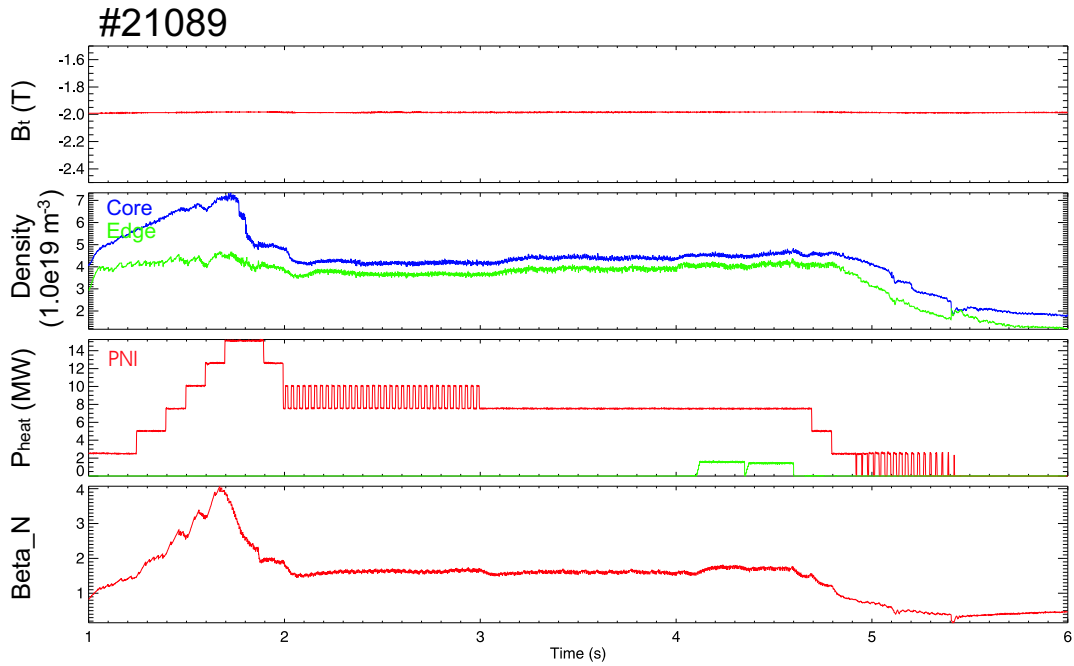


Figure 5.5: AUG Discharge 21089: Overview of the discharge. From top to bottom, the evolution of the, toroidal magnetic field, core and edge electron density, heating power and β normalized are presented.

between the NTM magnetic perturbation and the fast ion loss signal, but the low ELM frequency compared to the NTM frequency allows us to distinguish clearly between both signals.

5.3.1 (2,1) NTM Induced Fast Ion Losses

The effect of (2,1) NTMs on the fast particle population in ASDEX Upgrade has been studied in detail as one of the main issues of this thesis. In this section the results obtained from two NTM ASDEX Upgrade discharges will be presented. The main plasma parameters of the first discharge are outlined in Fig.5.5. The toroidal magnetic field was kept constant at $B_t = 2T$ with a relatively low core electron density. Six NBI sources were consecutively switched on up to a total heating power of 15 MW to trigger the NTM. After 200 ms of maximal heating power 2.5 sources were switched off to avoid possible overheating of the FILD probe due to prompt losses. Within the plateau phase, the ICRH heating was applied during 200 ms to investigate the effect of (2,1) NTMs on ICRH heated ions.

Fig.5.6 shows a CCD view of the light pattern generated by ion impacts on the scintillator plate during the (2,1) NTM phase. The NBI sources active at this time point are shown at the bottom of the picture in order to identify the spots due to prompt losses. The strike points of lost ions due to the (2,1) NTM are encircled in red. The fact that they appear outside the energy-pitch angle grid is due to the fact that they are only marginally allowed by the aperture geometry, due to their high parallel component of the velocity. Nevertheless the ions can be

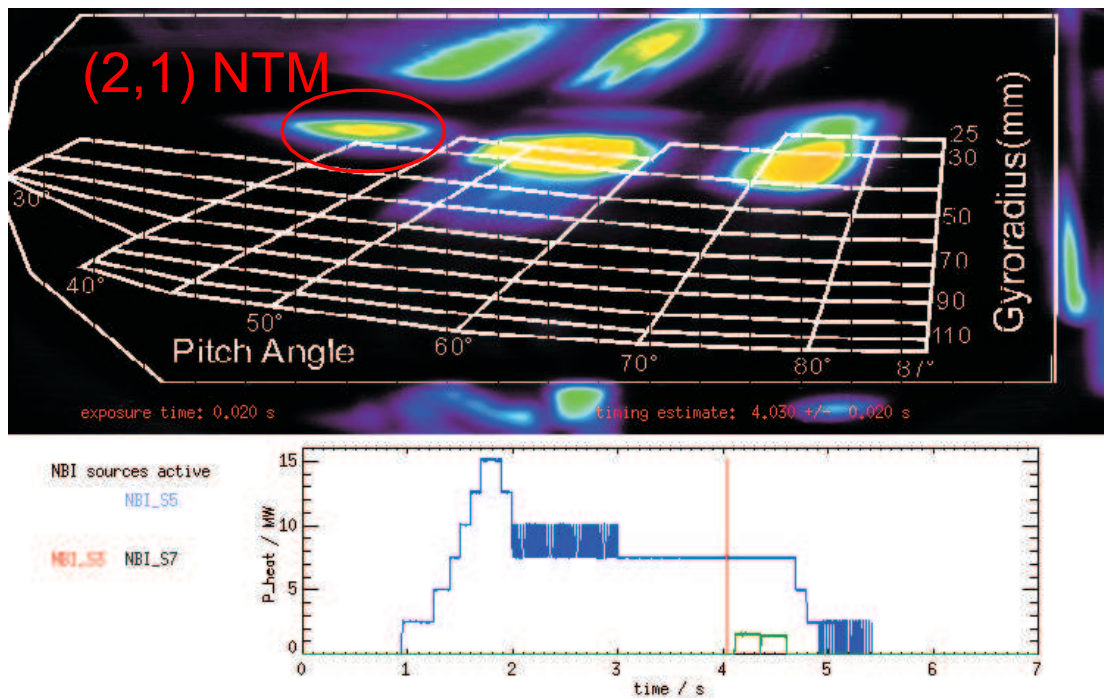


Figure 5.6: AUG Discharge 21089: CCD view showing the three spots produced by first orbit losses from NBI sources 3, 5 and 7, on the right, and (2,1) NTM induced fast ion losses, on the left. On the bottom the three active NBI sources are depicted.

identified with the full acceleration energy of the 5th and 7th NBI source and a pitch angle of around 40°. The spots further more outside the depicted scintillator plate are due to infrared emissions from the heated graphite cap.

A Fast Fourier transform (FFT) of the magnetic pick-up coil signal during a phase with pure NBI heating and a later phase with NBI and ICRH heating is shown on the left of Fig.5.7. The evolution of the width of the NTM island has been analyzed following the strength of B_{θ} (Island width $\propto \sqrt{B_{\theta}}$) with the frequency of the (2,1) NTM, on the bottom of the magnetic pick-up coil FFT. A considerable rise of about 60% in the NTM island width is appreciable when the ICRH is switched on. On the right of the figure, an FFT of the FILD channel which covers the corresponding scintillator plate area (FIPM7) is shown together with the raw signal evolution at the NTM frequency (on the bottom). An abrupt rise of the fast ion loss signal by 400% is estimated compared to the $\approx 60\%$ increase in the island width.

The dependence of the lost ion fluxes on the magnetic island width was studied in more detail in discharge number 21168 with NBI blips during a stationary phase with a (2,1) NTM. An overview of some discharge parameters is shown in Fig.5.8.

Fig.5.9 shows on the left an FFT of the magnetic pick-up coil C05-01 signal together with an amplitude analysis of the main magnetic perturbation between 10 and 5 kHz. On the right hand side, the same analysis is presented for the fast ion loss signal recorded by the FILD channel FIPM07. A clear correlation can be established between lost ion fluxes and the NBI

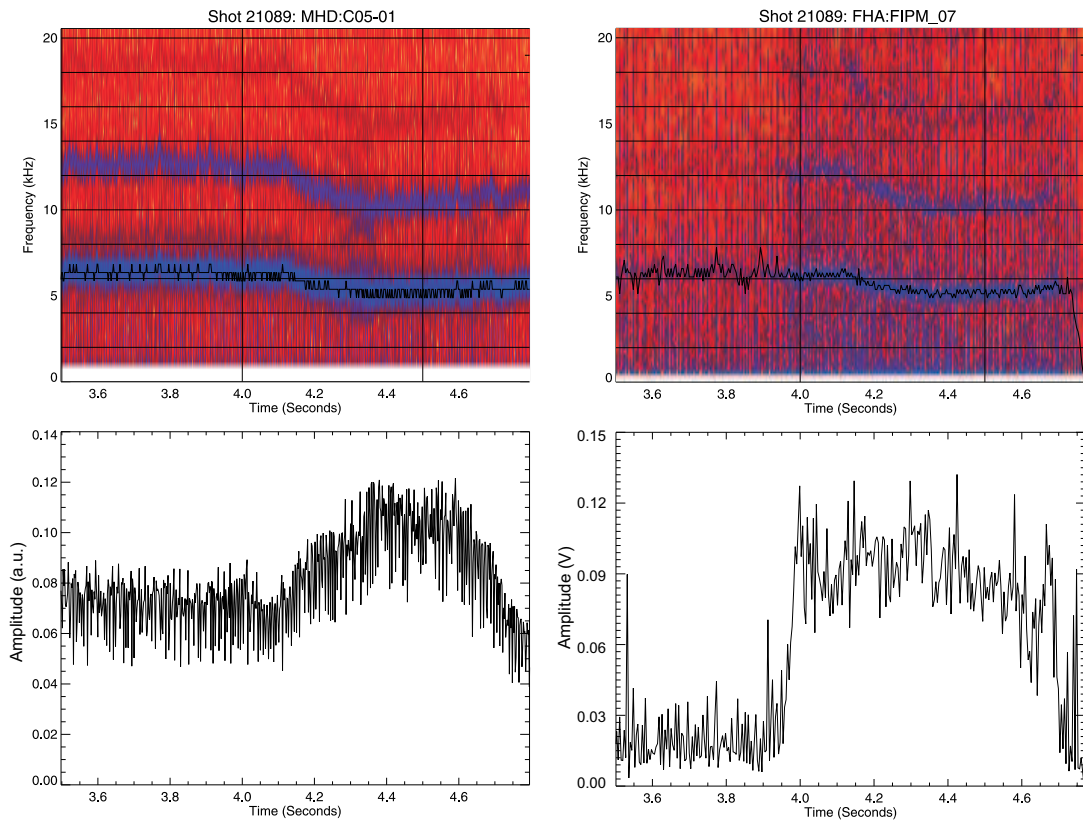


Figure 5.7: AUG discharge 21089: Amplitude analysis of the (2,1) NTM magnetic perturbation with a frequency of around 6 kHz, on the left, together with the signal evolution of the FILD channel FIPM7 at the same frequency, on the right.

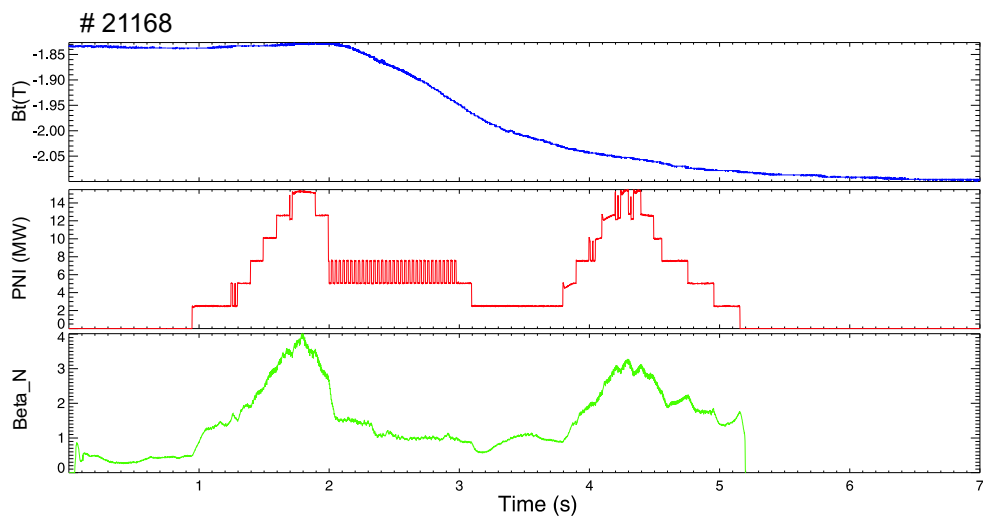


Figure 5.8: AUG discharge 21168: Overview of the discharge. From top to bottom, the evolution of the, toroidal magnetic field, NBI heating power and β -normalized are presented.

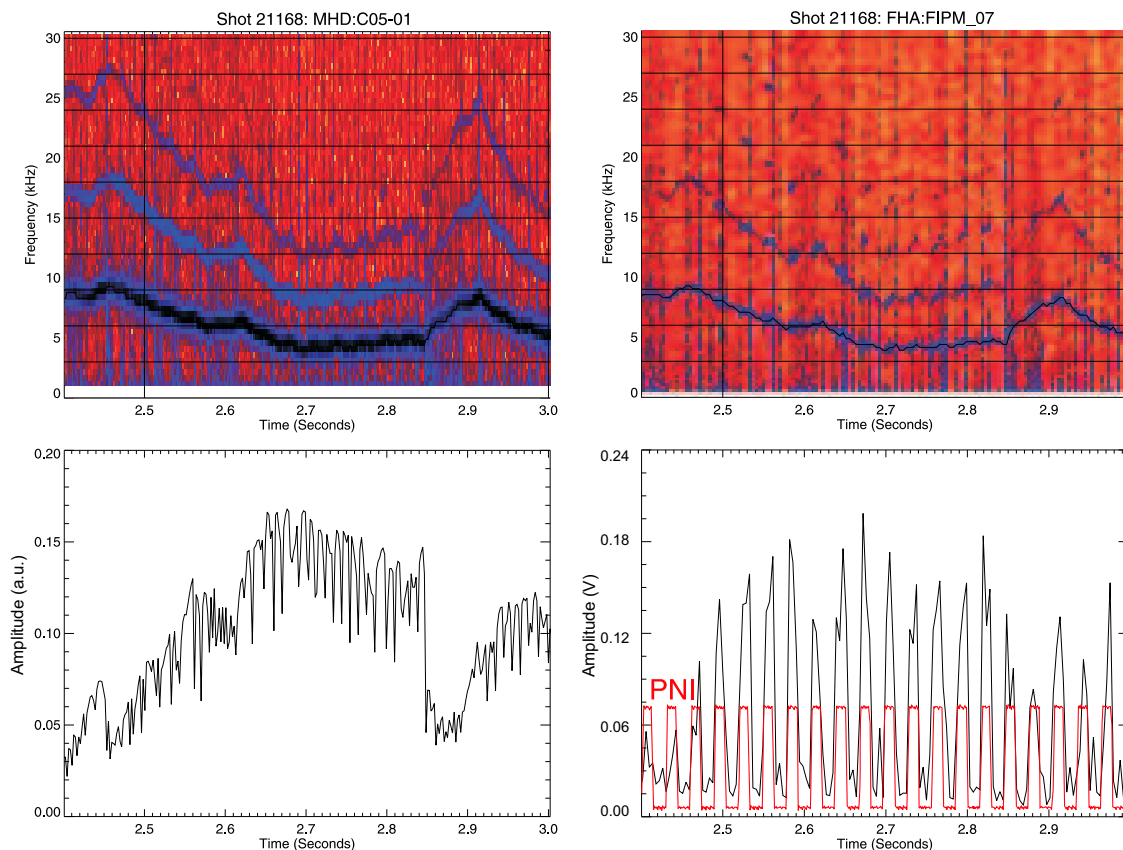


Figure 5.9: AUG discharge 21168: Amplitude analysis of the (2,1) NTM magnetic perturbation, \dot{B}_θ , with frequency between 10 and 5 kHz on the left, together with the signal evolution of the FILD channel FIPM7 at the same frequency modulated by NBI blips on the right.

blip sequence, which is superimposed in red on the same picture. The maximum flux achieved by each fast ion burst is also modulated by the island size evolution.

5.3.2 (3,2) NTM Induced Fast Ion Losses

(3,2) NTM Induced Fast Ion Losses in pure NBI Heated H-mode

Chronologically, one of the first events identified using FILD was the reproducible ejection of fast ions with high parallel components of the velocity in discharges with (3,2) NTM activity. The main results of (3,2) NTM induced fast ion losses have been taken in the early phase of FILD operation. Since the first particle collimator geometry was optimized to obtain high particle fluxes, the energy and pitch angle resolution of these measurements was not the most appropriate. Although particles on passing orbits are thought to be well confined, high fluxes of fast particles have been measured in a wide variety of (3,2) NTM discharges. Here, discharge 20528 with pure NBI heating power of up to 10 MW is presented. The main plasma parameters relevant for this section are outlined in Fig.5.10.

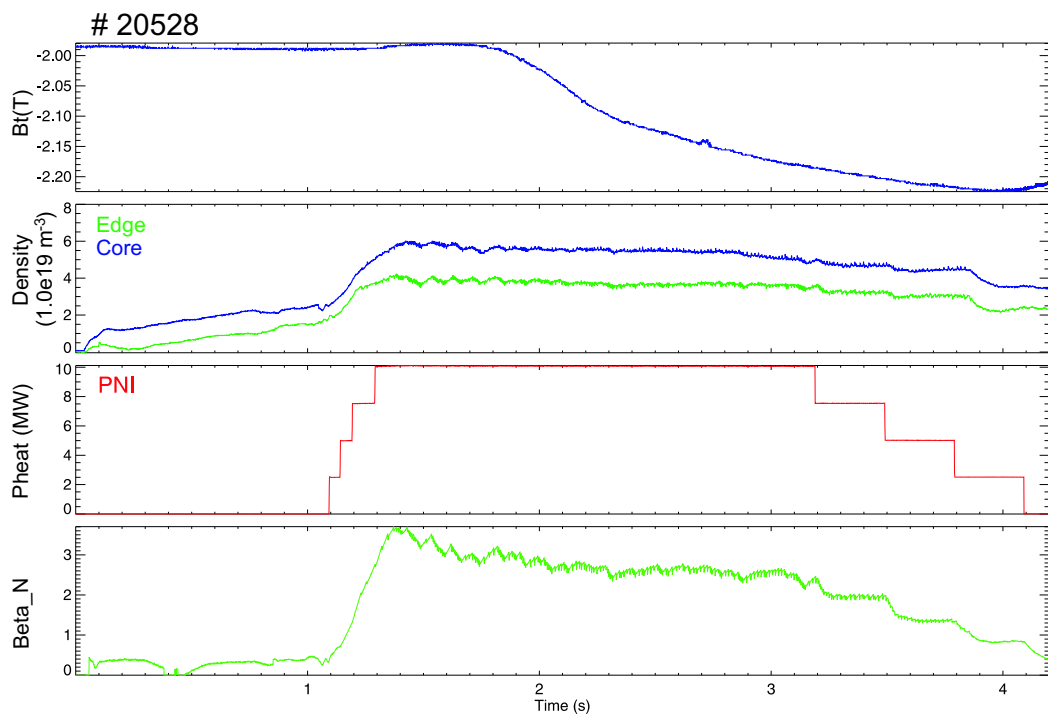


Figure 5.10: AUG Discharge 20528: Overview of the discharge. From top to bottom, the evolution of the toroidal magnetic field, edge and core electron density, NBI heating power and β -normalized are presented.

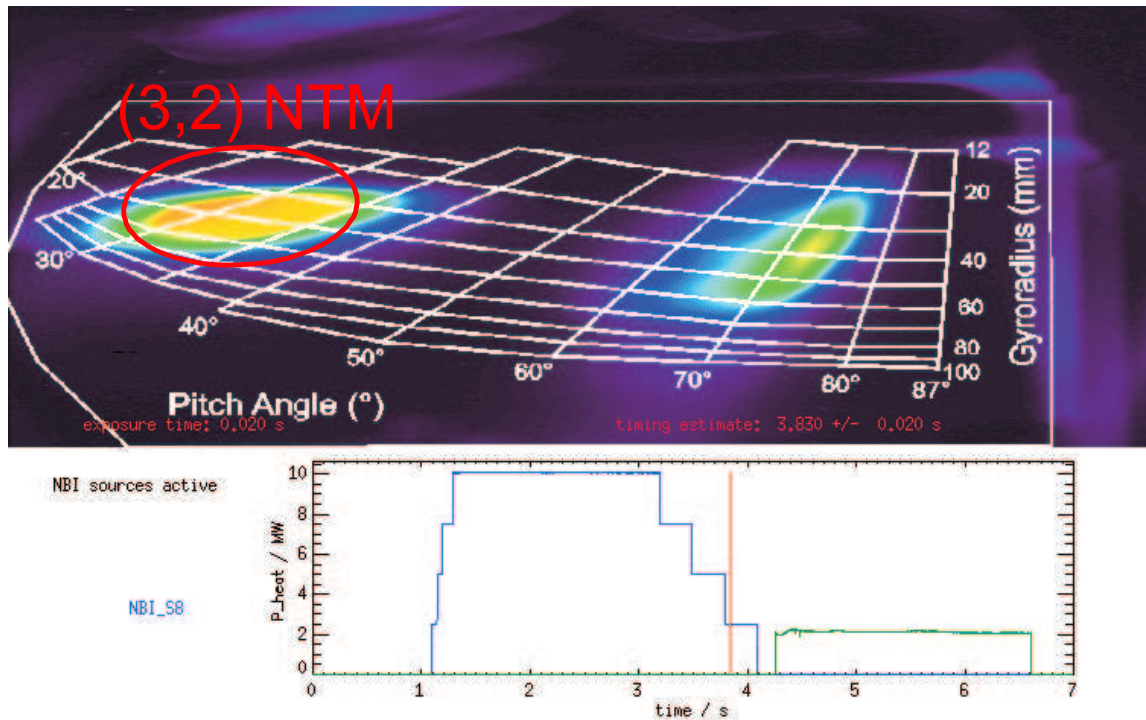


Figure 5.11: AUG Discharge 20528: CCD view. The picture shows in white the form of the scintillator together with the energy-pitch angle grid. Two spots are present; on the right first orbit losses and on the left losses observed only in discharges with (3,2) NTM activity.

(3,2) NTM induced fast ion losses can be easily identified from the CCD camera images: they appear in a phase space region well separated from the area dominated by first orbit losses. A view of the scintillator and the light pattern produced by the incident ions is shown in Fig.5.11. The lost ions correlated with the (3,2) NTM have a pitch angle of $30 - 35^\circ$ and the full energy component of the NBI source, approximately 93 keV. On the bottom of Fig.5.11, the time evolution of the active NBI sources is shown. In this case, source number 8 which is the source number 4 of NBI box 2 (radial injection direction) is indicated as active, and accordingly first orbit losses with a maximum energy of approximately 93 keV and a pitch angle of 73° are detected. Veils outside the line defining the scintillator edge are visible due to reflections of the light pattern at the cylinder walls.

In order to obtain the frequency of the losses, a Fast Fourier Transform (FFT) was applied to the magnetic pick-up coil signal as well as to the raw signal taken by the FILD-PMT (FIPM) which covers this scintillator area. The resulting spectrograms of this analysis are shown in Fig.5.12, together with the raw signal (on the bottom). On the top of the figure, the spectrogram of a magnetic pick-up coil shows the frequency evolution of the perturbation present in plasma during this time window. On the bottom of the figure, the spectrogram of FIPM7 is shown. Both spectrograms clearly show the same overall behavior, a distinct frequency, decreasing gradually from $\approx 28\text{kHz}$ to $\approx 18\text{kHz}$ with some small periodic variations superimposed.

Clearly, one can find a direct correlation of the fast ion loss frequency measured by channel

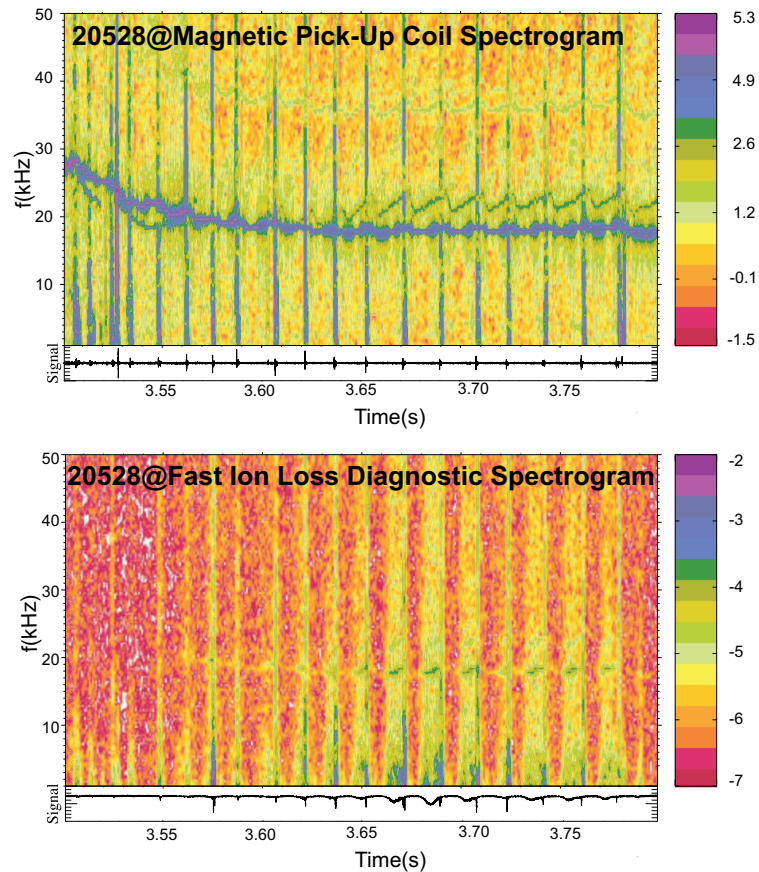


Figure 5.12: AUG Discharge 20528: Frequency analysis of the (3,2) NTM induced fast ion losses. On the top, the spectrogram of signal \dot{B}_θ , measured by one of the magnetic pick-up coils is shown. On the bottom, the spectrogram of the FILD channel FIPM7 shows a clear correlation.

FIPM7 and the magnetic perturbation frequency by comparing both spectrograms. The FIPM7 spectrogram shows a burst behavior of the fast ion losses between ELMs. All the fast ion loss bursts are terminated abruptly by ELMs as observed in the raw signal. The main magnetic perturbation with a well defined frequency of $f=28\text{kHz}$ at $t=3.5\text{s}$ was identified as a (3,2) NTM, which is responsible as well for the fast particle losses as indicated by the correlation between both signals. A secondary perturbation is visible in the magnetic pick-up coil spectrogram from $t=3.64\text{s}$ until the end of this time window, though it seems to eject nearly no fast ions.

(3,2) NTM Induced Fast Ion Losses with Mixed Heating in Improved H-Mode

The ejection of ICRH heated energetic ions due to (3,2) NTMs has been observed also in improved H-Mode discharges with mixed auxiliary heating. A discharge heated by two sources of the NBI heating system and 3 MW of ICRH is presented here as a prototype of (3,2) NTM H-mode discharge with deeply trapped ion losses. The time evolution of the toroidal magnetic

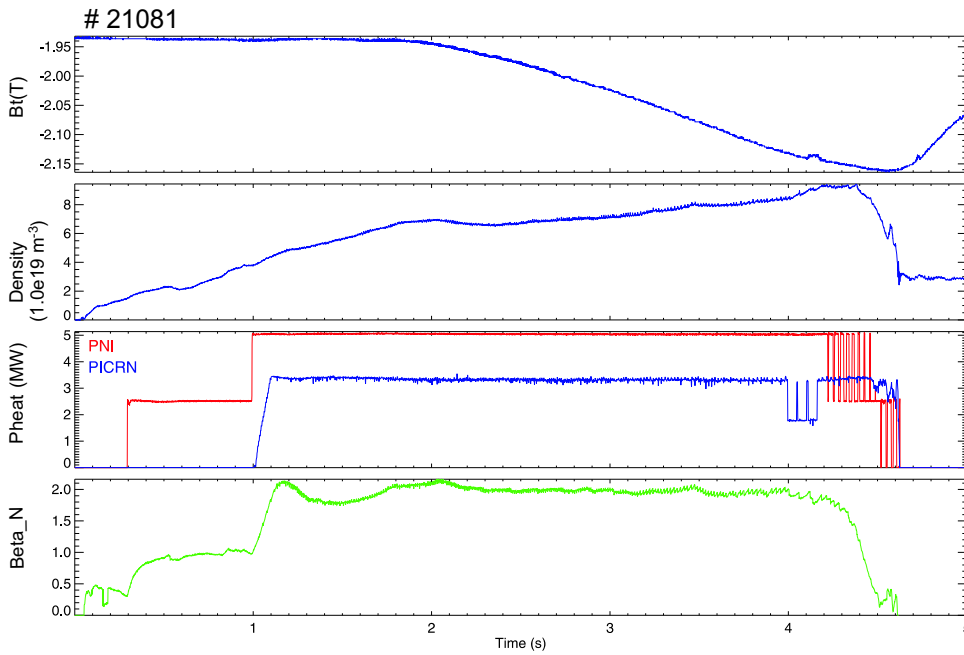


Figure 5.13: AUG discharge 21081: Overview of the discharge. From top to bottom, the evolution of the toroidal magnetic field, core electron density, heating power and β normalized are presented.

field, the core electron density, the different heating powers and the subsequently normalized β factor are outlined in Fig.5.13.

The light pattern generated on the scintillator plate due to the (3,2) NTM induced fast ion losses is shown in Fig.5.14 together with the heating power active at this time point. Prompt losses from the NBI source number 7 are easily identified by their energy (≈ 93 keV) and pitch angle ($\approx 50^\circ$). Much weaker but recognizable are the prompt losses caused by the NBI source number 3 with their lower energy (≈ 60 keV) and higher component of the lost ion velocity (pitch $\approx 75^\circ$). The other two spots at larger gyroradius and pitch angles around 65° appear simultaneously with the (3,2) NTM activity. In order to check this, a frequency analysis by means of an FFT of the magnetic pick-up coil signal as well as of one of the FILD channels, which covers the scintillator plate area illuminated by the incident ions was performed. The resulting spectrograms of the FFT analysis are presented in Fig.5.15. On the left hand side, the magnetic pick-up coil spectrogram shows the frequency evolution of the (3,2) NTM and its first harmonic together with the amplitude of the magnetic perturbation, \dot{B}_θ . On the right hand side, the same FFT analysis of the FILD channel FIPM13 shows a clear correlation in frequency with the main mode but also the effect of the first three harmonics is visible. At $t \approx 2$ s, the mode amplitude rises to three times its initial value within 300 ms. The fast ion loss signal doubles in the same time interval but falls off much earlier and steeper. This last observation implies an almost linear dependence of the losses with the amplitude of the magnetic perturbation.

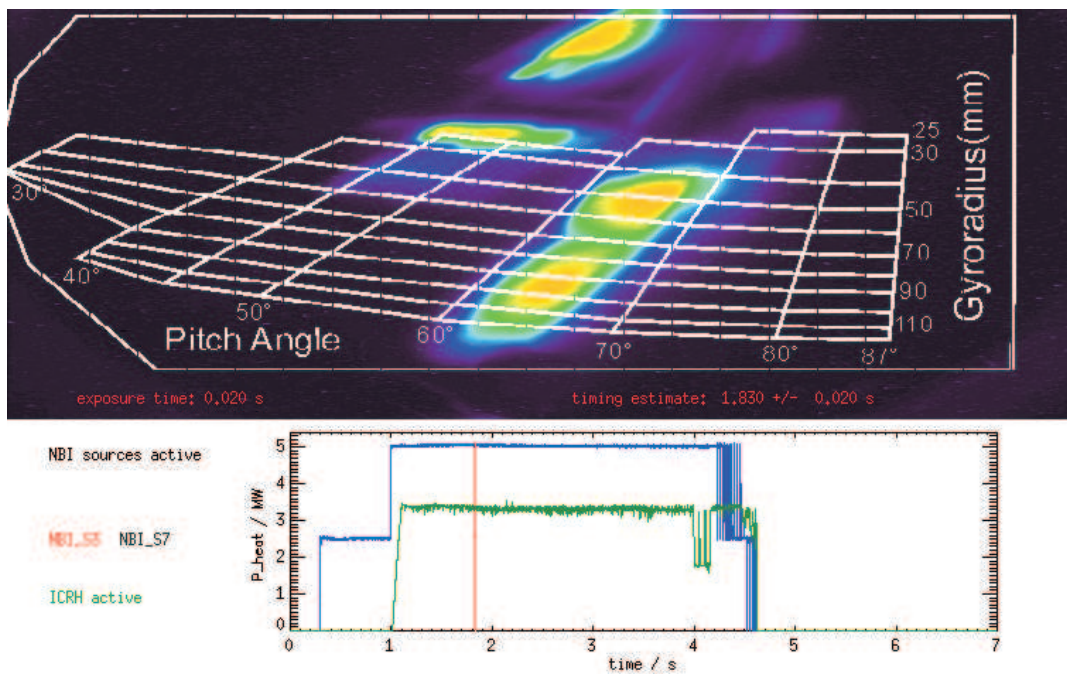


Figure 5.14: AUG Discharge 21081: CCD view of the light pattern produced by first orbit losses and the (3,2) NTM induced fast ion losses, two spots on the right with gyroradii greater than 40 mm (the maximal NBI injection energy). On the bottom the two active NBI sources and the ICRH heating power are illustrated.

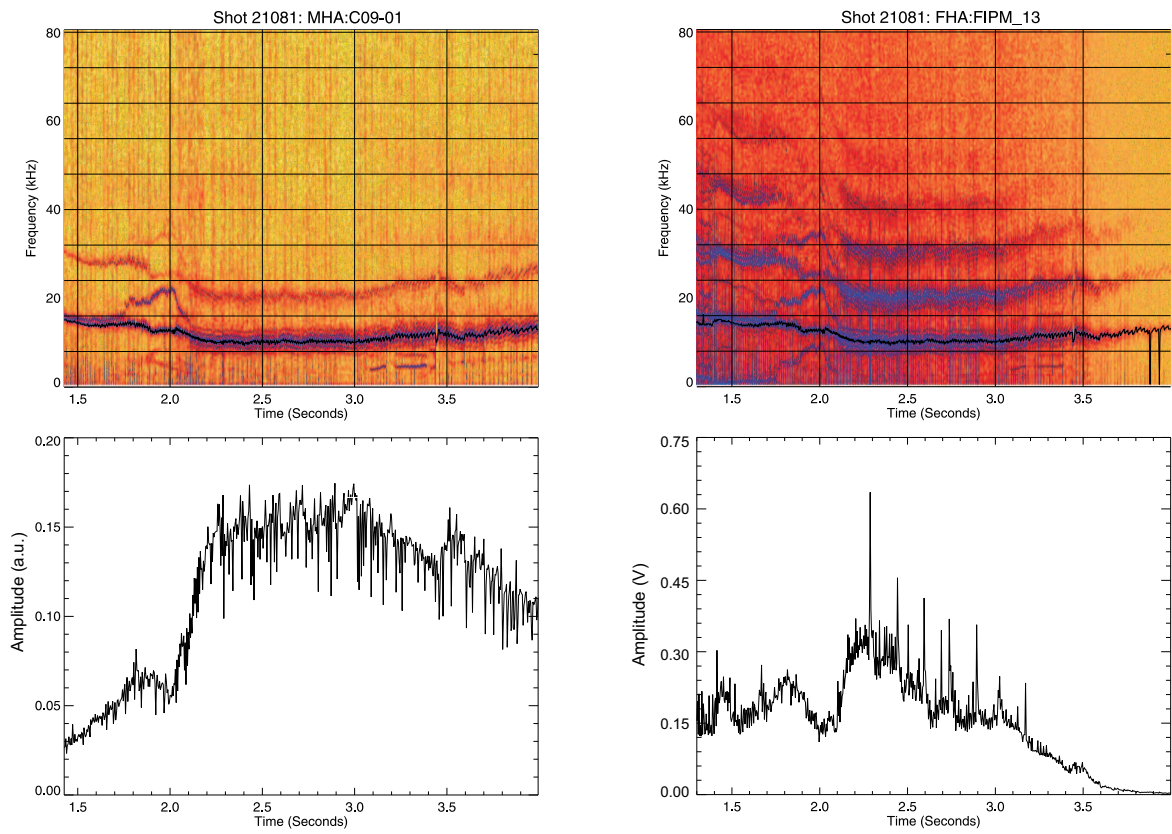


Figure 5.15: AUG Discharge 21081: Time evolution analysis of the frequency and amplitude of the (3,2) NTM magnetic perturbation, \hat{B}_θ on the left and the FILD channel FIPM7 on the right.

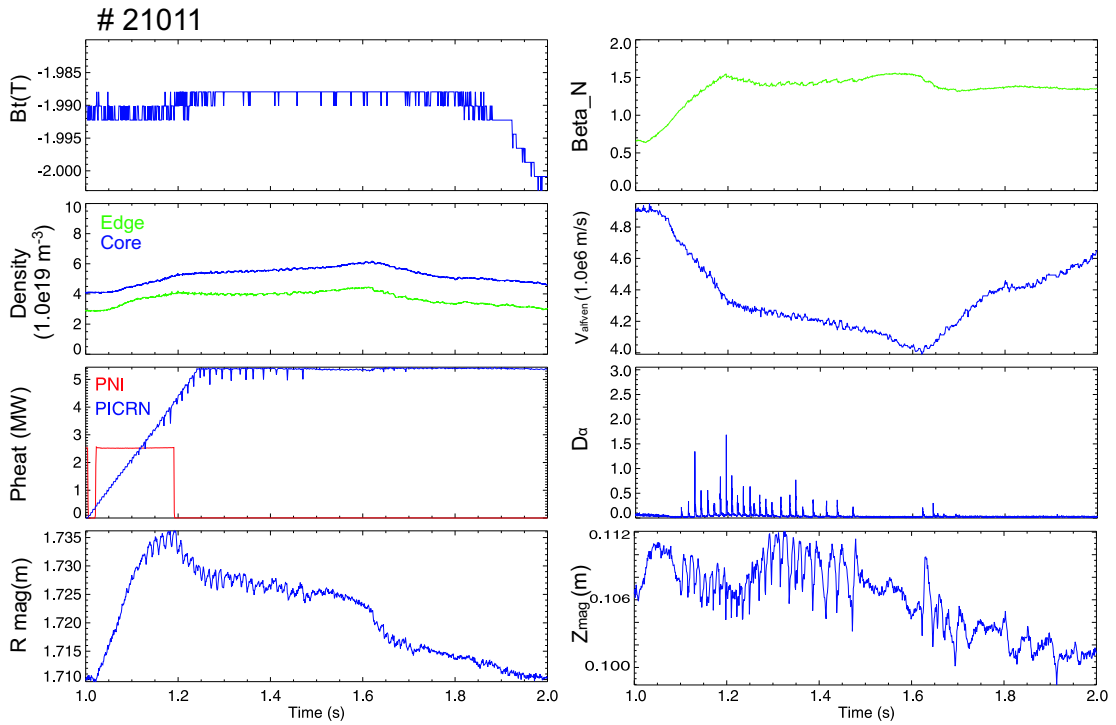


Figure 5.16: AUG discharge 21011: Overview of the main discharge parameters. From top to bottom: toroidal magnetic field, normalized β , edge and core density, Alfvén velocity, heating power, divertor D_α signal and the (R,z) position of the magnetic axis. The Alfvén velocity was calculated using the core density.

5.4 Fast Ion Losses due to High Frequency MHD Activities

The behavior of energetic ions in the presence of high frequency MHD activities has been studied in different scenarios. High frequency MHD phenomena have been excited either by ICRH heated fast ions or by beat waves formed directly in plasma by the ICRH antennas. The resulting fast ion losses due to interactions of those with Alfvén waves traveling in plasma are summarized here in two discharges.

5.4.1 Fast Particle Driven MHD Modes; TAEs and Others

AUG Discharge 21011

The discharge was designed to create a large population of fast ions inside the $q=1$ surface to stabilize the internal kink and to produce long sawtooth periods [64]. Destabilization experiments of such sawteeth have been performed in JET with ICRH heating. In all cases a rich variety of MHD activity like Monster Sawtooth, TAE or Energetic Particle Modes (EPMs) was observed.

To exploit all possibilities, the main plasma parameters have been ramped covering a wide

range. The line integrated density signal (DCN H-1) shows a ramp from 0.0 m^{-3} at $t=0.0\text{s}$ up to $6.06 \times 10^{19} \text{ m}^{-3}$ at $t=1.6\text{s}$ with some dips, then it falls off to $4.13 \times 10^{19} \text{ m}^{-3}$ at $t=2.5\text{s}$. The ICRH system was ramped up to its maximum, 5.3 MW, from $t=1.0\text{s}$ to $t=1.2\text{s}$ and remains constant for the rest of the discharge. In order to achieve the H-Mode the source number 8 of the NBI heating system was modulated from $t=0.0\text{s}$ up to $t=1.0\text{s}$, staying then stable at 2.5 MW until its switching off at $t=1.2\text{s}$. A B_t ramp was performed to make a radial scan of the ICRH resonance layer, covering in addition a wide frequency range of Alfvén gap, thereby exploiting the maximal possibilities to excite TAEs.

On the top of Fig.5.17, the magnetic Pick-Up coil spectrogram shows a large variety of MHD activity between $t=1.2\text{s}$ and $t=2\text{s}$. At the very beginning a strong TAE activity appears during density development, once the density reaches its maximum value, the TAE remains in plasma but, as expected, much weaker. During the first stationary TAE phase, from $t=1.4\text{s}$ to $t=1.6\text{s}$ three TAE modes are observed with toroidal modes $n=4$, $n=5$ and $n=6$ and an increasing frequency of $f=149\text{kHz}$, $f=154\text{kHz}$ and $f=159\text{kHz}$ respectively. Sawtooth crashes are present with a period of 60 ms ejecting fast ions from the $q=1$ surface and consequently interrupting the TAEs due to a lack of driving force. During the whole H-Mode phase, as expected, the magnetic signal is strongly affected by ELM bursts. In addition, $n=m=1$ fishbones are easy to identify in the spectrogram due to their characteristic form. Finally, from $t=1.6\text{s}$ till the end of the phase, Washboard modes [65] are present in a broad frequency range of 30 kHz, between 70 and 100 kHz.

On the bottom of Fig.5.17, the frequency analysis (spectrogram) of one of the PMTs shows a rich variety of strong, coherent and not-coherent particle losses. In this case, the chosen PMT, covers an area defined by a pitch angle of around 70° and a gyroradius of around 90 mm. During the early phase between $t=1.2\text{s}$ and $t=1.5\text{s}$, in H-mode, different TAE modes appear ejecting resonant fast ions with the same frequency of the $n=4$, $n=5$ and $n=6$ modes. Although the magnetics show the TAEs clearly also in L-mode, the fast ion loss signal decreases as soon as the discharge goes to L-mode, having a phase between $t=1.55\text{s}$ and $t=1.65\text{s}$ without any footprints of any coherent fast ion loss. In a later L-mode phase between $t=1.7\text{s}$ and $t=2.0\text{s}$ with stronger TAE activity, coherent fast ion losses appear again clearly correlated with the magnetics. The TAE induced ion loss signal is in the early phase clearly interrupted by three sawtooth crashes observed at $t=1.24$, $t=1.31\text{s}$ and $t=1.43\text{s}$. The sawtooth crashes expel ions in a wide frequency range of up to 40 kHz, covering the whole TAE frequency range (TAE gap). The first crash shows a broader frequency range while the third one shows its signal maximum more localized in frequency. As described previously, in H-mode the fast ion loss signals are always modulated by ELMs.

A new coherent MHD activity has been observed ejecting fast ions from $t=1.2\text{s}$ to $t=1.48\text{s}$ which does not leave any footprints in the Mirnov Pick-Up coils. As Fig.5.17 shows, the mode is not visible in the Mirnov Pick-Up coil spectrogram however it seems to be very effective ejecting fast particles. The FILD spectrogram shows a weak coherent fast ion loss signal starting at 1.2s at a frequency of around 110 kHz decreasing in frequency up to 80 kHz by $t=1.28\text{s}$. Then, the losses appear much stronger oscillating in frequency around $80 \text{ kHz} \pm 10 \text{ kHz}$. It is important to remark that although the losses are coherent, they are present in a much

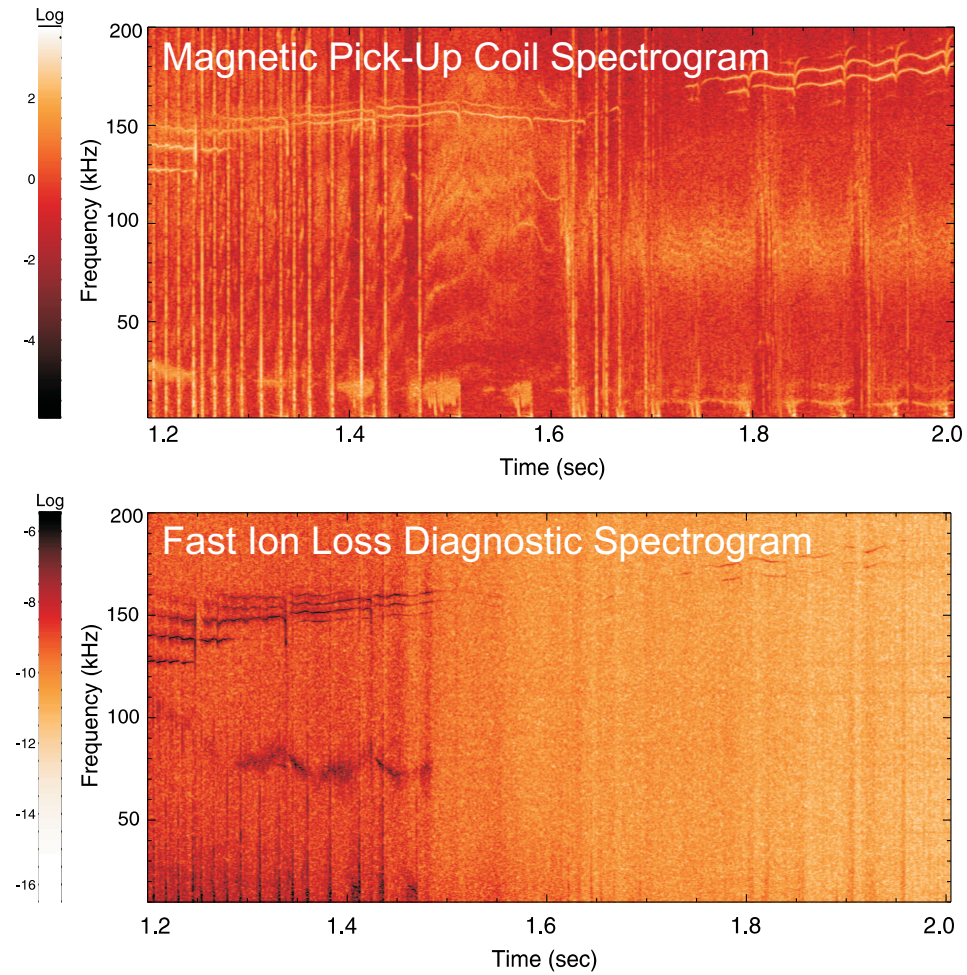


Figure 5.17: AUG discharge 21011: On the top, frequency analysis of the magnetic pick-up coils showing TAEs, Sawtooth crashes, ELMs, Fishbones and Washboard modes. On the bottom, the spectrogram of the FILD PMT number 12 which shows ion losses correlated with various types of MHD activities; TAEs, Sawtooth crashes, ELMs and an unidentified mode not visible in the Mirnov coils.

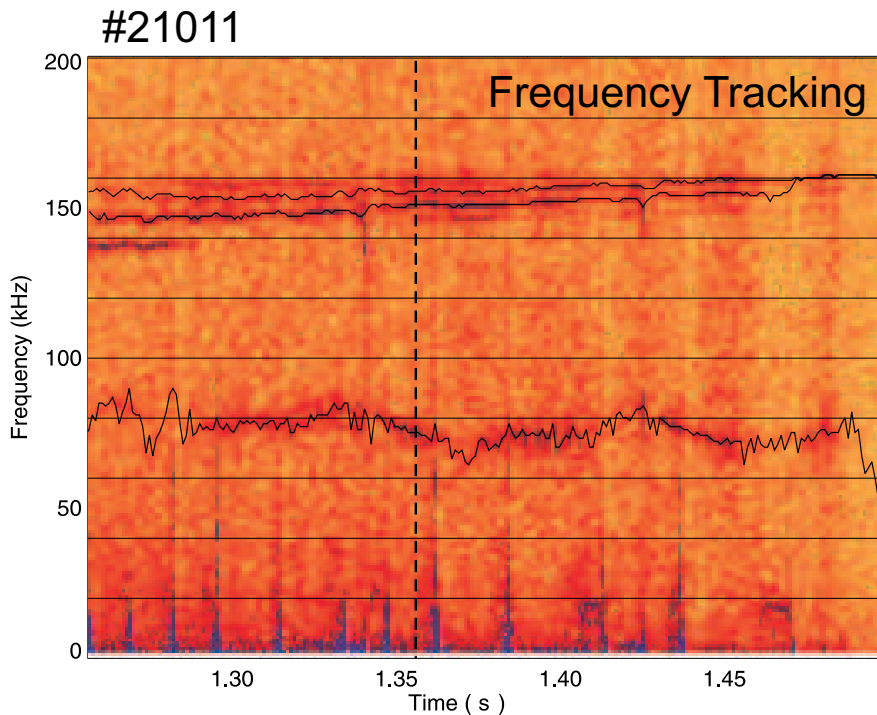


Figure 5.18: Frequency Tracking of Fast Ion Losses Induced by different TAE modes and the Sierpes Mode.

broader frequency range with, in some phases, comparable signal peaks to those ejected by the TAEs. Therefore a detailed analysis of the lost ion fluxes due to single TAEs and the new mode is mandatory. Due to the hidden nature of this new mode within the magnetic signals together with the snake-like footprints left in the FILD spectrogram, the mode will be called *Sierpes Mode* (snake in spanish).

Fig.5.18 shows the tracking of the coherent ion losses induced by two TAEs and the Sierpes mode.

Following the amplitude, Fig.5.19, of the signal measured by FILD at these three frequencies ($\approx 80, 149$ and 154 kHz) one can find that this new mode is much more effective ejecting fast ions than the single TAEs during the whole time window. Nevertheless, a similar time evolution of the three signals can be established, finding some correlations in the occurrence of the spikes. This suggests a kind of coupling between either modes or between the loss mechanisms.

Fig.5.20 may help to understand the higher fluxes of lost ions due to the 80 kHz mode. The figure shows the frequency distribution of lost ions at $t=1.355$ s. The contribution of the 4 TAEs is clearly visible at frequencies around 160 kHz, with a very narrow distribution of ion losses around the main frequency of each single TAE. Not only a stronger spike at around 80 kHz than each of the TAE spikes, but also a decaying but strong signal at 10 kHz around the main frequency is observed. An integration of the ion loss signal around the main frequency leads to the stronger contribution of the 80 kHz mode due to frequency blur.

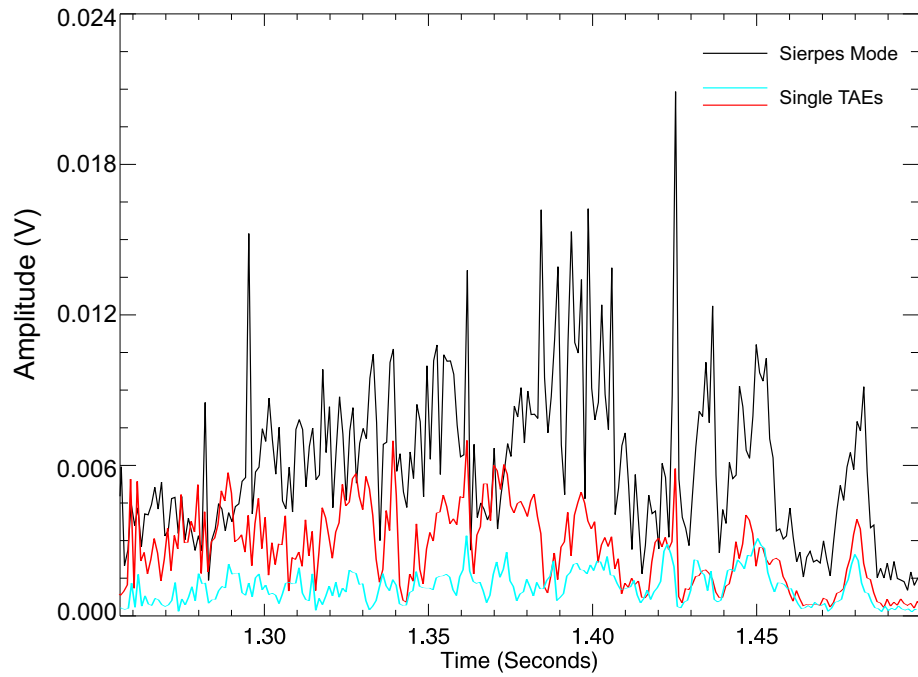


Figure 5.19: Fast ion loss rates due to single TAEs, red and blue traces, and the Sierpes mode in black. A correlation between loss rates is clear.

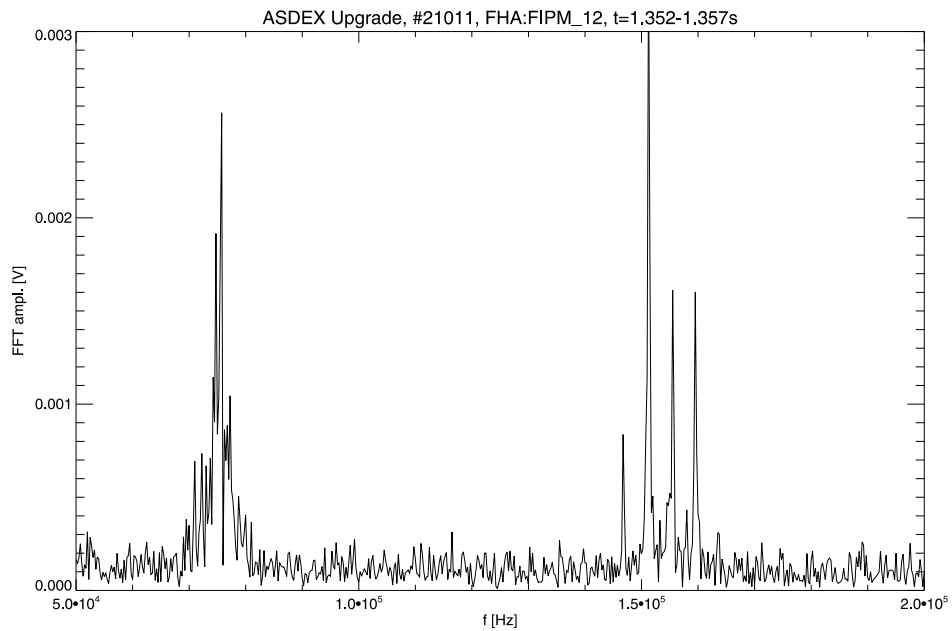


Figure 5.20: Fourier spectrum obtained from the FILD channel FIPM12. 1 Frame of the FFT time evolution. Sierpes mode (≈ 80 kHz) and single TAEs (≈ 150 kHz) are plotted.

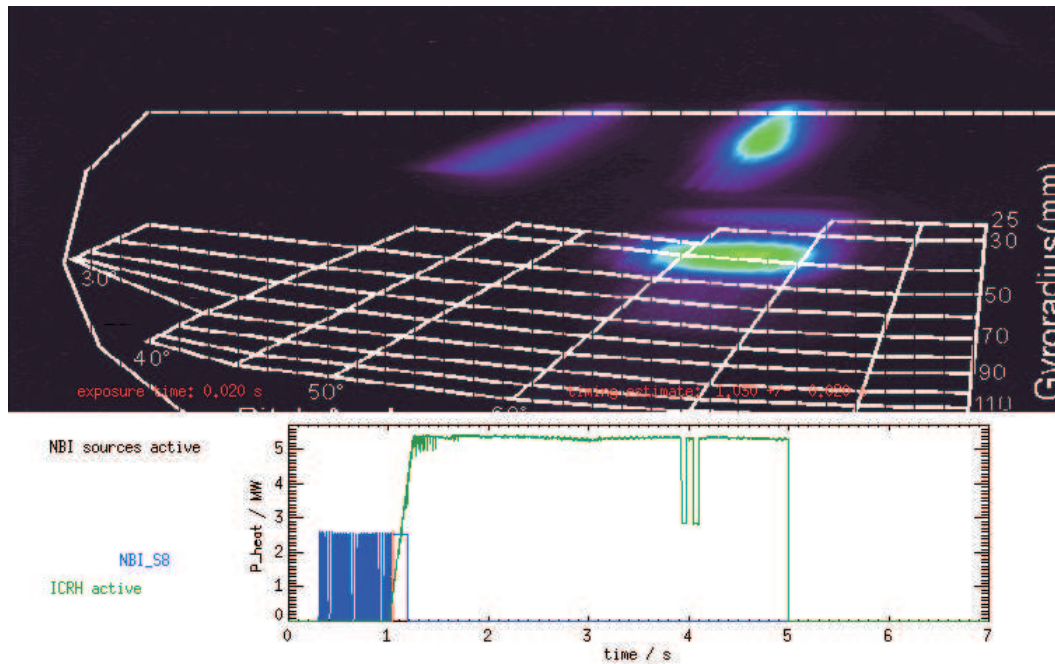


Figure 5.21: AUG Discharge 21011: CCD view of the light pattern produced by first orbit losses, injected in plasma by the NBI source number 8.

After a completed time evolution analysis of the ion losses in frequency as well as in amplitude, a study using the camera data to find out the energy and pitch angle of the lost ions with more accuracy than that given by the wide areas covered by each PMT was undertaken. In the following, a sequence of 4 frames is presented to understand the complicated light pattern introduced in a discharge with such a rich variety of MHD activity and simultaneously ICRH and NBI heating. The first frame, Fig.5.21, taken at the very beginning of the discharge with pure NBI heating shows the prompt losses from the NBI source number 8, (gyroradius ≈ 40 mm, $\arccos(v_{\parallel}/v) \approx 65^{\circ}$). This picture is already well understood, as it was described in detail at the beginning of this chapter, and it is presented here just as a reference for the next three frames. The ICRH is shown in green as active but still without significant power deposition.

The second frame, Fig.5.22, taken at $t \approx 1.15$ s shows the double effect of the ICRH heating (≈ 3 MW heating power) and the presence of the first TAEs on the fast ion population. Three different spots can be distinguished now. The first and better established one corresponds to the prompt losses due to the NBI source number 8. The second one contributes to the deformation of this first prompt loss light spot at higher pitch angles ($> 70^{\circ}$) and almost the same gyroradius (between 30 and 40 mm). A third spot with stronger amplitude and broader distribution in energy and pitch angle appear in the region defined by a gyroradius between 60 and 110 mm and a pitch angle around 67° . The following two frames help to understand this picture.

The third frame, Fig.5.23, was taken right after the switch off of the NBI heating (it still appears as active in the figure). As a consequence, the light spot due to prompt losses starts to

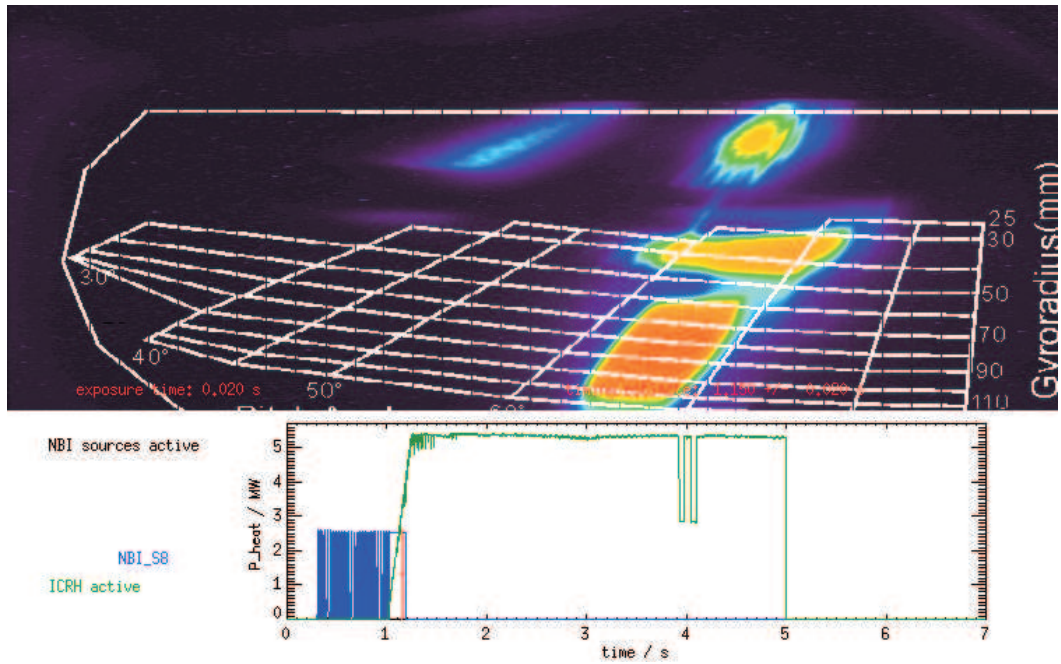


Figure 5.22: AUG Discharge 21011: CCD view of the light pattern produced by first orbit losses, injected in plasma by the NBI source number 8 together with the losses induced by the high frequency modes. Two species are ejected; hydrogen and deuterium ions.

disappear, changing the light pattern of the smaller gyroradius spot. At this time point the contribution of the ICRH at small gyroradius and pitch angles of 67° remains almost unperturbed by the switching off of NBI. The same happens with the light spot at larger gyroradius.

The last frame, Fig.5.24, of the sequence was taken 230 ms after the NBI switching off so that no more prompt losses are appreciable. Nevertheless two spots remain on the scintillator which are thought to be independent of the NBI heating.

In order to understand this light pattern, complicated by the presence of high frequency MHD activities and mixed heating systems, the fluxes of deuterium and hydrogen neutrals measured by the CX diagnostic were integrated for the time windows corresponding to the different frames presented previously. Fig.5.25 shows for the first frame a high flux of deuterium neutrals with energies up to 90 keV. The hydrogen fluxes and the last point of the deuterium fluxes at 120 keV are too low to be significant and therefore are not taken into account. For the second CCD frame, with simultaneous NBI and low power ICRH heating, a high deuterium flux with energies up to 120 keV (maximal detectable energy for deuterium) is observed, while a hydrogen flux up to 70 keV starts to be appreciable. In the third frame, with already $\approx 3MW$ of ICRH and one source of NBI heating, intense fluxes of both species are present (up to 120 keV for deuterium and 240 for hydrogen). 230 ms after the NBI switches off, deuterium fluxes with energies up to 120 keV are still important while hydrogen fluxes are now higher at higher energies. This study of the hydrogen and deuterium neutral fluxes will allow to distinguish between fast deuterium and hydrogen ion losses during the discussion chapter.

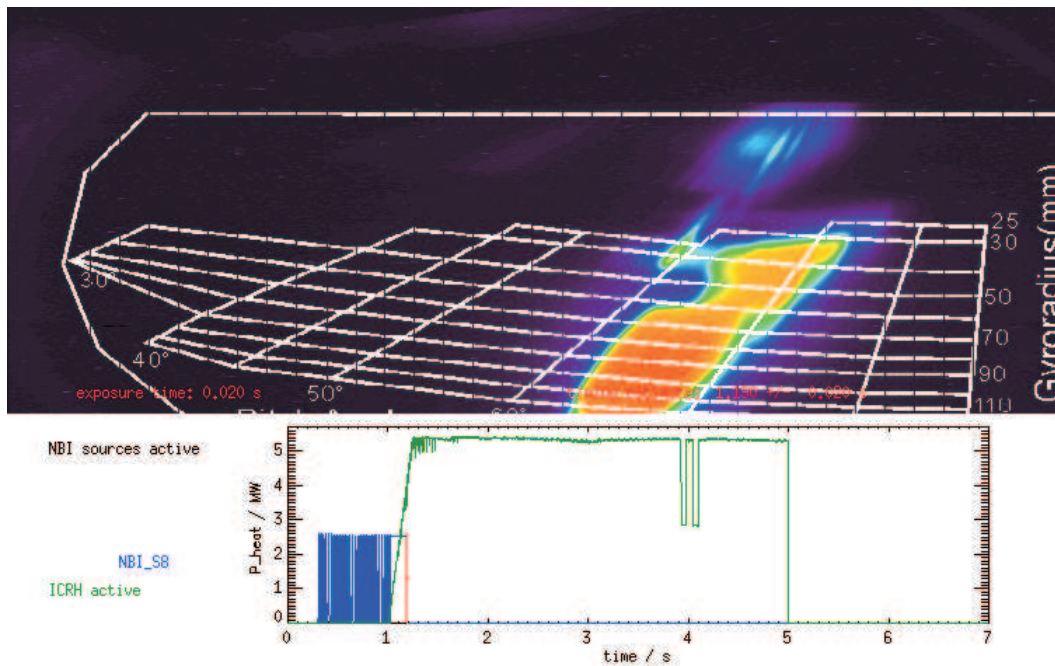


Figure 5.23: AUG Discharge 21011: CCD view of the light pattern produced by the incident ions ejected due to interactions with the high frequency modes. Two species are ejected; hydrogen and deuterium ions.

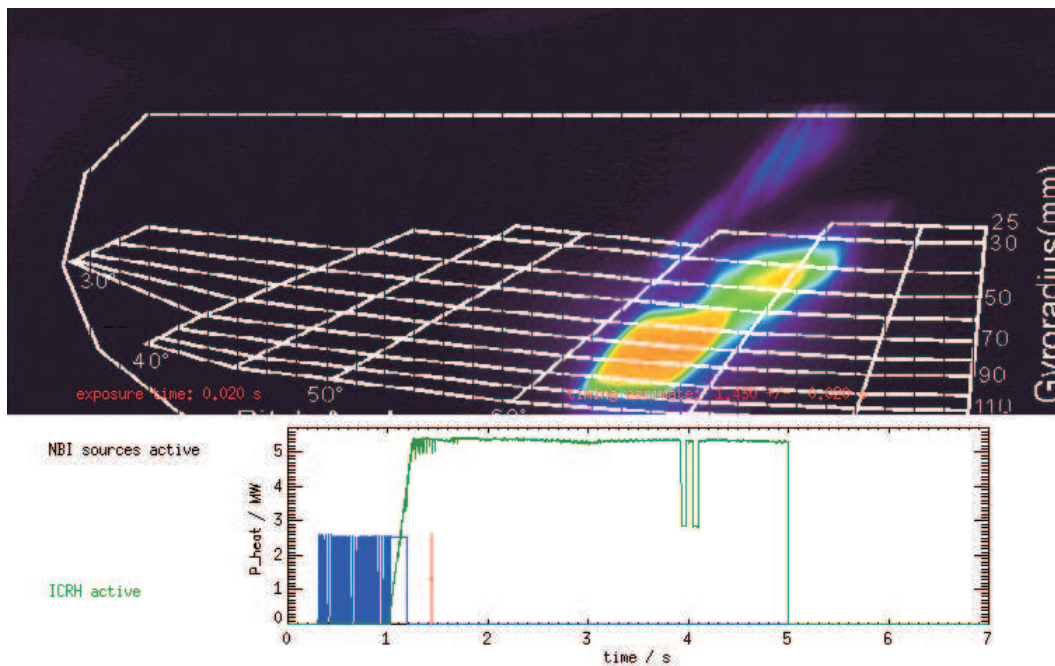


Figure 5.24: AUG Discharge 21011: CCD view of the light pattern produced by the incident ions ejected due to interactions with the high frequency modes. Two species are ejected; hydrogen and deuterium ions.

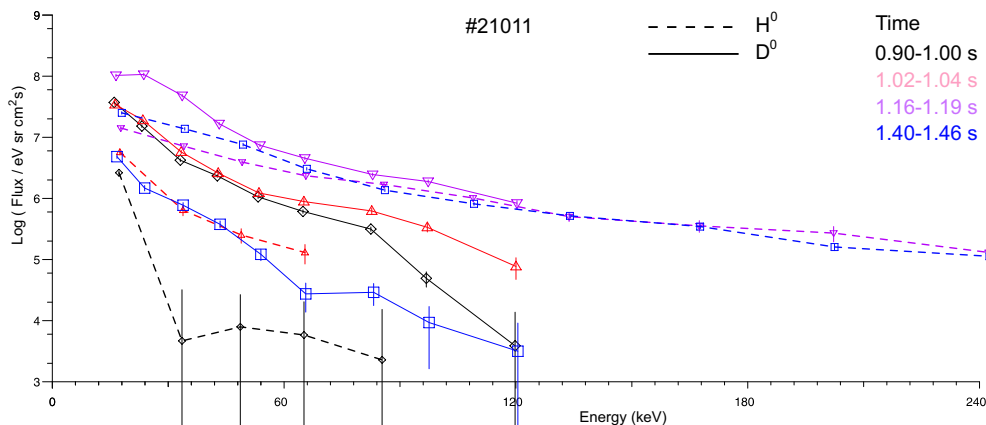


Figure 5.25: AUG Discharge 21011: Fluxes of deuterium and hydrogen neutrals measured by the CX diagnostic during four different intervals.

Discharge 21083

Discharge 21011 was repeated with slight differences to check the reproducibility of such results. Discharge 21083 was performed with very similar plasma parameters, obtaining almost the same MHD activity during the ICRH phase. Some operation parameters are outlined in Fig.5.26. The toroidal magnetic field was kept constant at $B_t = -1.94T$ to maintain the ICRH resonance layer mainly inside the $q=1$ magnetic surface thus increasing the fast ion population within this surface, enabling the excitation of MHD activity within this surface through fast ion driving mechanisms. The discharge was heated with up to 6 MW of ICRH at relative low electron densities.

The MHD activity observed by the magnetic pick-up coil is shown in the first spectrogram of Fig.5.27. A pattern similar as from discharge 21011 is obtained but now the blurred 80 kHz signal is present also on the magnetic coils. On the bottom of the figure, the spectrogram of the FILD channel FIPM13 shows again a similar pattern to the 21011 discharge. At frequencies around 80 kHz, *coherent* fast ion losses due to the Sierpes mode are clearly visible during a time window longer than the presence of the TAE activity. The similarity in the frequency evolution of the losses suggests that the ion losses are induced by the same activity, the Sierpes mode, in both cases. In this discharge, all the 6 TAEs visible in the magnetic coils eject fast ions during the whole time that they are in plasma.

5.4.2 Beat Waves Driven TAEs

In ASDEX Upgrade an important emphasis has been placed during the last campaign on the excitation of TAEs via Beat Waves. The Beat Wave is a standing wave formed in plasma launching waves by means of the ICRF antennas with a frequency difference, $f_1 - f_2$, of the Beat Wave frequency, $f_{BeatWave} = f_1 - f_2$. Two possibilities have been exploited to get the TAE excitation via Beat Waves; the first one consists of forming a Beat Wave with a constant frequency close to the frequency of a typical TAE Alfvén gap in an ASDEX Upgrade plasma

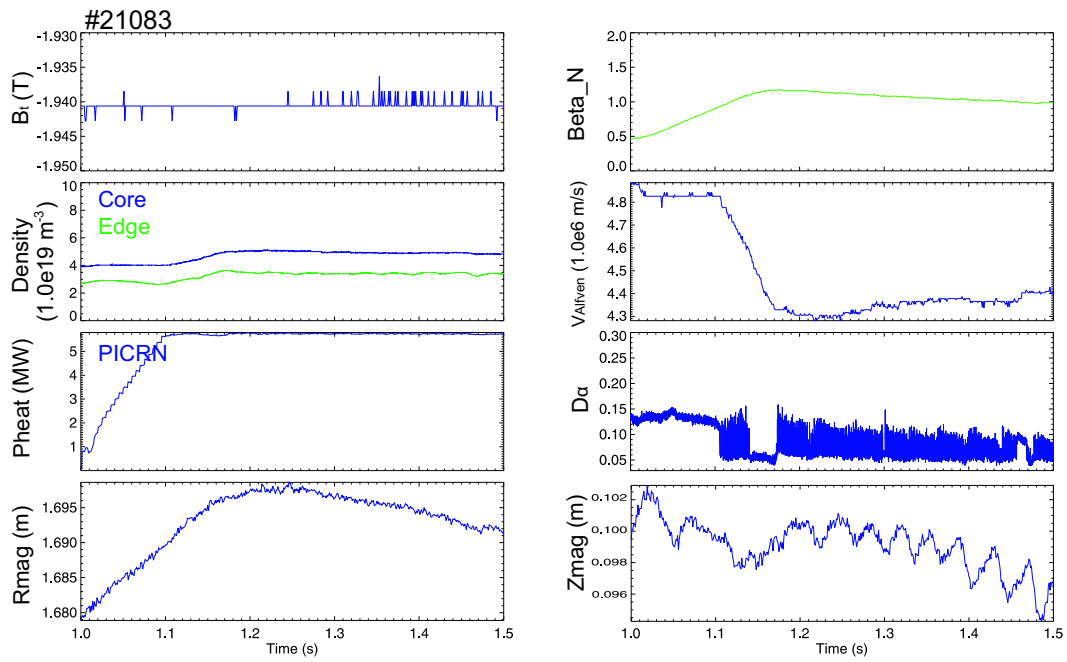


Figure 5.26: AUG Discharge 21083: Overview of the main discharge parameters. From top to bottom: toroidal magnetic field, normalized β , edge and core density, Alfvén velocity, heating power, divertor D_α signal and the (R,z) position of the magnetic axis. The Alfvén velocity was calculated using the core density.

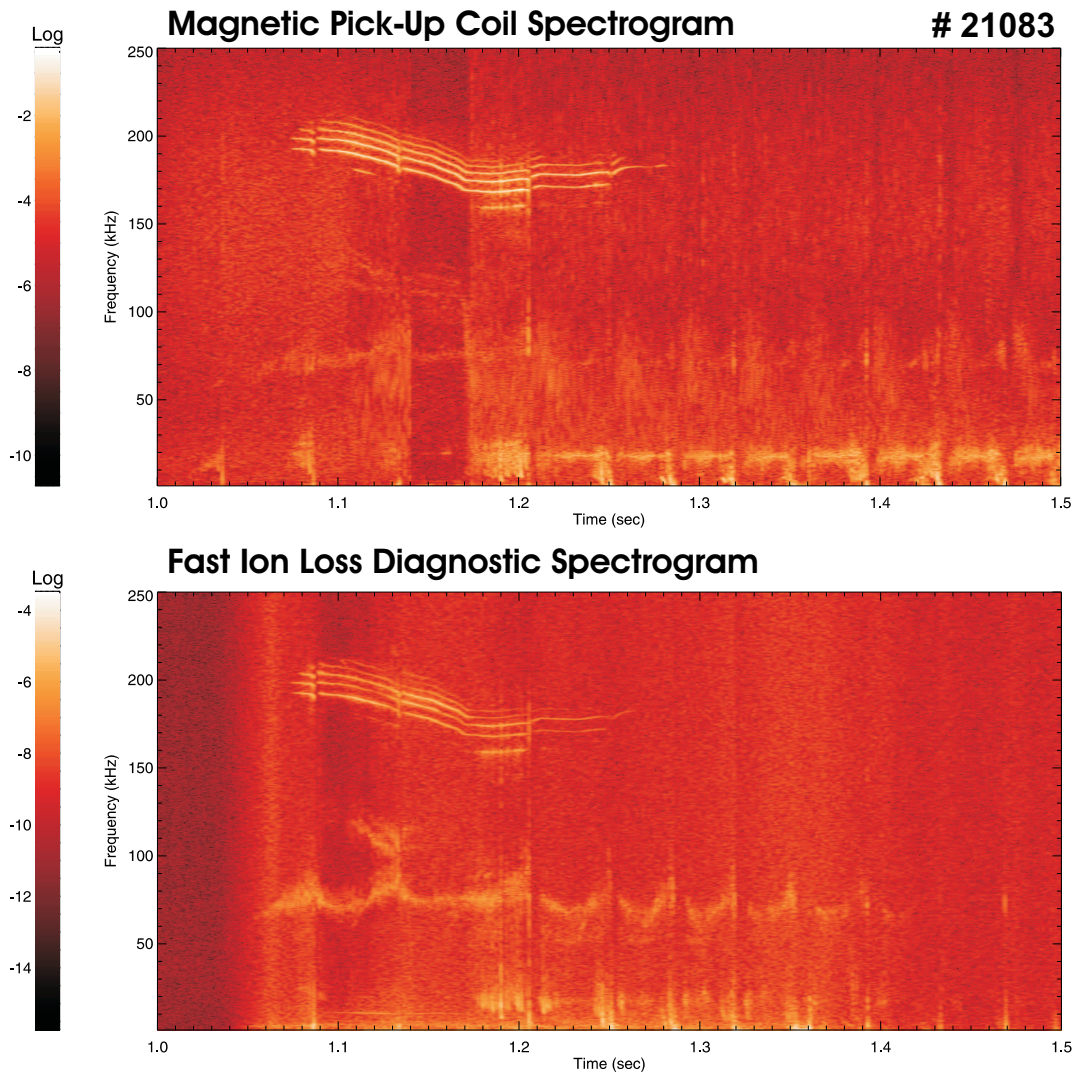


Figure 5.27: AUG discharge 21083: On the top, frequency analysis of the magnetic pick-up coils showing TAEs, Sawtooth crashes and Fishbone modes. The Sierpes mode at frequencies around 80 kHz is also visible. On the bottom, the spectrogram of the FILD channel FIPM13 shows ion losses correlated with various types of MHD activities; TAEs, Sawtooth crashes, Fishbone modes and the Sierpes mode.

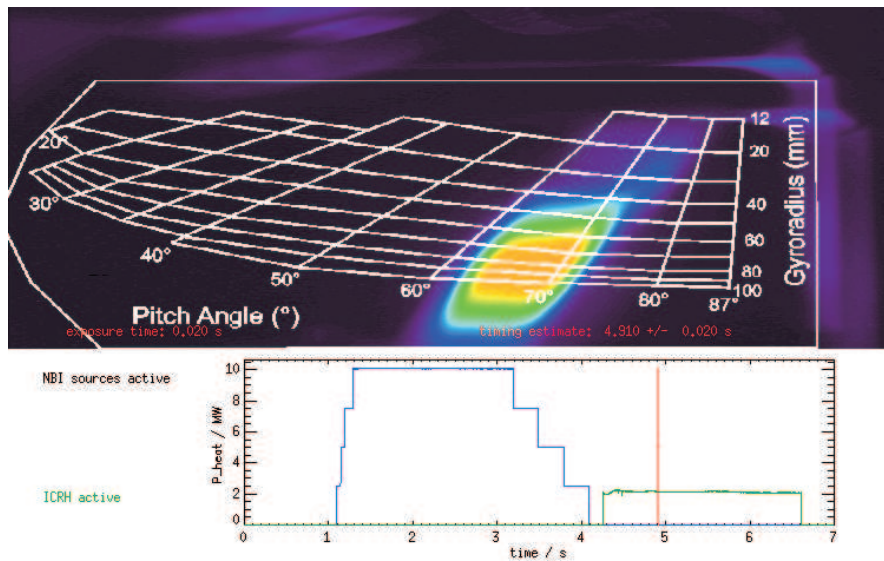


Figure 5.28: AUG Discharge 20528: CCD view of the light pattern produced directly by the Beat Wave or by the Beat Wave driven TAE induced fast ion losses. On the bottom the ICRH heating power is depicted.

with a B_t ramp to cover the entire Alfvén gap, the other possibility consists of making a Beat Wave frequency sweeping maintaining constant B_t [66]. The flux of lost ions measured by FILD in a discharge with a fixed $f_{BeatWave}$ and a B_t ramp is shown in Fig.5.28. Only 2 MW of central ICRH heating are sufficient to achieve a similar ion loss light pattern as in discharge 21011 or 21083. In this case, the first aperture was used so that the energy and pitch angle resolution are not the optimal and therefore only one large light spot is visible.

Ion losses have been detected as well in a discharge with a constant B_t and a Beat Wave frequency sweeping of $\delta f = 180$ kHz. An overview of the discharge parameters in the studied phase is presented in Fig.5.29

Fig.5.30 shows on the top, the frequency sweeping of the Beat Wave observed in the magnetic pick-up coil spectrogram. In an early phase a coupling between the Beat Wave and a low frequency mode is visible. On the bottom of the figure, the spectrogram of the FILD channel FIPM13 shows a clear correlation between the frequency of the lost ions and the Beat Wave.

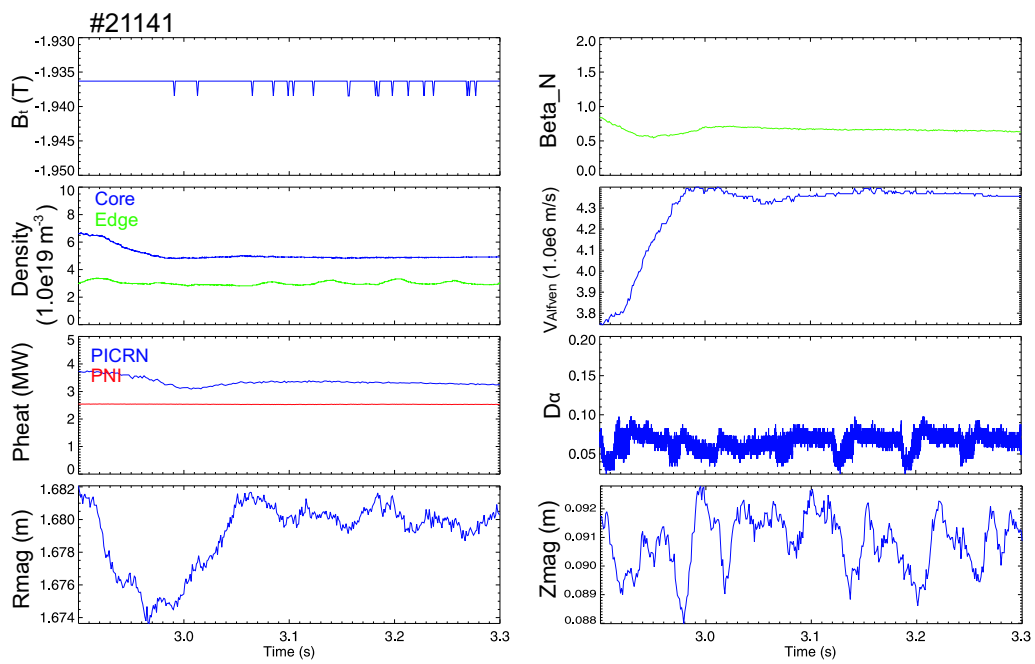


Figure 5.29: AUG discharge 21141: Overview of the discharge parameters. From the top to the bottom: toroidal magnetic field, normalized β , edge and core density, Alfvén velocity, heating power, divertor D_α signal and the (R,z) position of the magnetic axis. The Alfvén velocity was calculated using the core density.

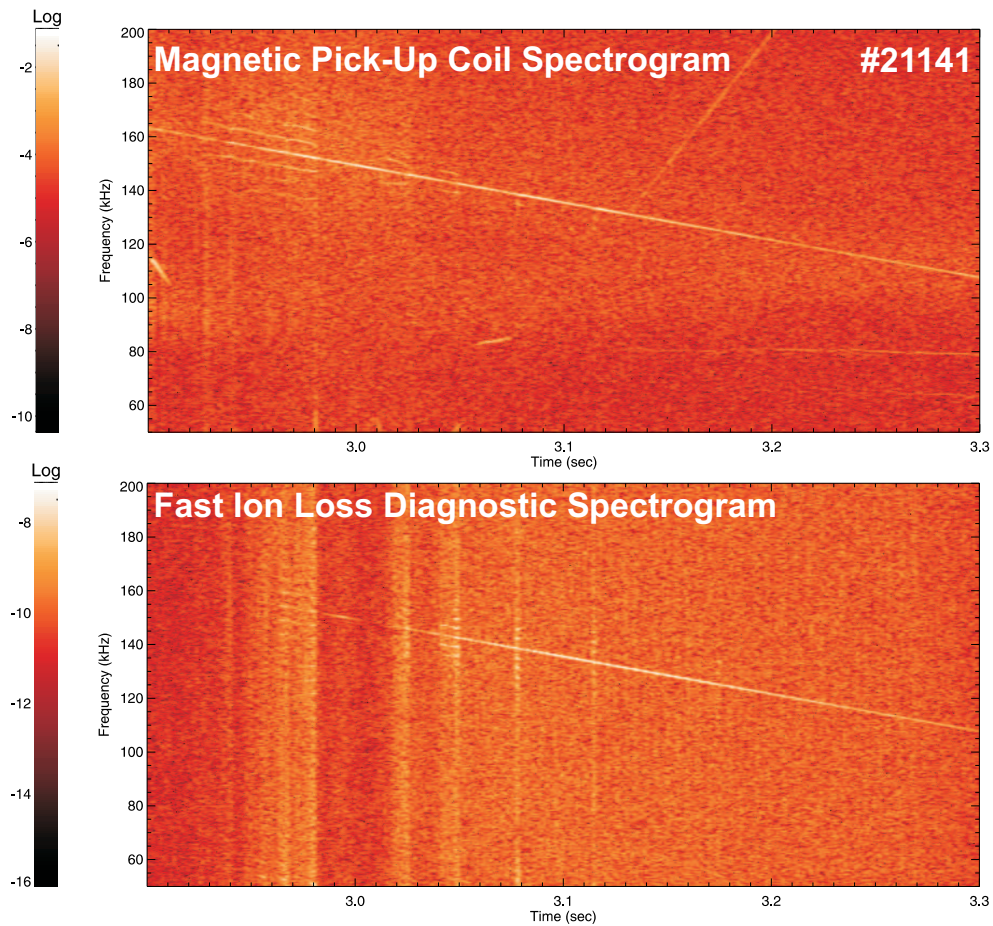


Figure 5.30: AUG Discharge 21141: Spectrograms of magnetic pick-up coils and channel FIPM13 of FILD. A clear correlation is visible between the sweeping frequency of the Beat Wave formed in Plasma and the fast ion losses measured by FIPM13.

Chapter 6

Discussion

Despite the limited time allocated to FILD exposure on the mid plane manipulator in the past experimental campaigns, a large amount of surprisingly rich information on fast ion losses driven by a zoo of MHD modes has been accumulated as described in the previous section. A detailed discussion and interpretation of all these results is far beyond the scope of this work and must be left for future analyses. Nevertheless, the responsible processes for the expulsion of fast ions in discharges with ELMs, NTMs and TAEs have been studied and are discussed here. The following sections are structured as follows: First, the results obtained by FILD are connected to previous work, identifying the lack of information existing in each field and giving the contributions of the FILD measurements to these issues. Second, a detailed explanation of the conclusions derived from the FILD results is presented. And finally, further work is proposed based on the main conclusions given in the corresponding section together with the limitations of our study in case there are.

6.1 ELM Induced Fast Ion Losses

FILD measurements in H-Mode plasmas are significantly perturbed, whenever ELMs appear, specially in case of the large type-I ELMs. In fact, ELMs have been observed modulating the ejection of fast ion losses in a wide variety of scenarios. The influence of ELMs on escaping fast particles is appreciable in the whole lost particle phase space. From particles which leave the plasma on deeply trapped orbits to those which do it on passing orbits, the signal modulation due to ELMs shows a strong character, in general, independent of the fast ion source. Fast ion losses have been indirectly observed also by other diagnostics. Heat fluxes at in-vessel components of ASDEX Upgrade in H-mode discharges have been analyzed in a previous work by A. Herrmann et al [67]. NBI created prompt losses, ICRH heated fast ions and ELM energy bursts from the plasma edge have been reported as the main contributions to the limiters. The ELM heat flux to in-vessel components can reach up to tens of MW/m^2 . Furthermore, from the nonaxisymmetric energy deposition pattern on ASDEX Upgrade divertor target plates, the ELM mode structure was derived leading to mode numbers of 8-24, [68].

As it is well known, the ELM affected area extends from over a range δr from the plasma edge

pedestal well inside the separatrix out to the scrape off layer (SOL) and limiters. Fast ions penetrate this δr feeling the effect of the perturbed magnetic field and due to the stochastic ELM behavior and their large gyroradius, eventually leave the plasma. The ELM modulation of the lost ion signal has been observed in prompt losses created by the NBI system, mainly trapped ions, as well as in NTM induced fast ion losses, purely passing orbits. Both regions of the lost particle phase space are influenced by the ELM modulation in the same proportion. The dependence of the fast ion losses with ELM mode numbers still has to be established. Furthermore, a correlation between the complicated internal substructure shown by each single ELM in the magnetic pick-up coils and the signal shown by each FILD channel will give important hints toward a better understanding of the ELM substructure.

In addition to this ELM induced fast ions transport, there is some fast ion loss contribution related to ions created in the edge and reaching the detector on their first transit without any further transport mechanism. In fact, ELMs expel some plasma in a bursty fashion into the SOL, modulating in this way the ionization of the neutrals injected by the NBI box 2.

6.2 NTM Induced Fast Ion Losses in NBI Heated H-Modes

Low frequency MHD perturbations e.g. Fishbone Modes or NTMs have been observed to affect the trajectories of fast particles causing their losses. Lost ion fluxes due to (3,2) and (2,1) NTMs comparable to those due to NBI prompt losses have been measured in discharges with pure NBI heating as well as in discharges with mixed heating, ICRH and NBI. In this section, the resulting lost ion pattern due to (2,1) NTMs in pure NBI heated discharges will be studied and connected to previous works. Losses of deuterium ions in these scenarios have been detected in the phase space areas corresponding to passing orbits which normally are thought to be well confined. Previous works suggest orbit stochasticity as the main responsible mechanism for the losses of the, in principle, well confined passing particles in the presence of low frequency magnetic perturbations. Even though this transport mechanism is theoretically feasible, as described in Chapter 2, and is suspected to have caused or enhanced fast ion losses in tokamaks during a variety of experiments [69], detailed experimental verification that orbit stochasticity causes fast ion losses is sparse. α particle losses on TFTR have been measured by Zweben et al [14], suggesting orbit stochasticity as the responsible loss mechanism. Problems in categorizing the MHD activity as well as modeling the vacuum and the perturbation field allowed only a qualitative agreement. Furthermore, the effect of externally imposed helical fields on fusion product orbit stochasticity on DIII-D has been studied by Heidbrink et al [70], reporting no impact on fusion product confinement, as predicted by theoretical estimates. A similar study on the effects of externally applied rotating magnetic perturbations on ion drift orbits was carried out by Pritchard et al [71] in the Compact Auburn Torsatron. Carolipio et al [29] reported the most detailed experimental verification of orbit stochasticity as a mechanism for beam ion loss up to date. They compared numerical simulations of orbit stochasticity with data obtained at DIII-D in experiments with large, stationary MHD modes and simultaneous reductions in both the 2.5 MeV neutron production ($\leq 65\%$) and the central noninductive current ($\leq 55\%$). Nevertheless, an important lack of information on the lost ion population

features (temporal and phase space information) makes impossible an exhaustive study of the orbit stochasticity influence on ion transport due to low frequency magnetic perturbations.

6.2.1 Fast Ion Loss Rate due to NTMs

After the first observations of NTM induced fast ion losses in ASDEX Upgrade, special emphasis has been placed on fast ion related NTM experiments to clarify the relationship between the fast ion loss rate and the magnetic perturbation amplitude as well as to identify the phase space region covered by the ejected ions. In the previous chapter, the lost ion patterns measured by FILD during (3,2) and (2,1) NTM experiments in ASDEX Upgrade were presented. A significant difference in the lost ion population from plasmas with (3,2) and (2,1) NTMs was observed. In phase space, ions ejected by (3,2) NTMs appear with higher parallel components of the velocity ($\arccos(v_{\parallel}/v) \approx 30^\circ$) than those expelled from plasmas with (2,1) NTM activity ($\arccos(v_{\parallel}/v) \approx 40^\circ$). In both cases measurements show the lost ions with a gyroradius corresponding to the first energy component of the NBI2 system (≈ 93 keV). The fast ion loss rate has been analyzed in detail for the (2,1) NTM case as Fig.5.7 and Fig.5.9 show. In discharge 21089, a (2,1) NTM was triggered applying a high NBI power (15 MW) for a short time interval. During a *stationary* (2,1) NTM phase a short ICRH blip was applied to investigate the influence of ICRH heating (acceleration in the perpendicular component of the velocity) on the (2,1) NTM induced fast ion loss rate. Although ICRH accelerates only the perpendicular component of the ion velocity, a considerable increase of the lost fast ion fluxes in the phase space region which corresponds to passing ions was observed. These additional losses were identified as (2,1) NTM induced fast ion losses, indicating that ICRH increases the fast ion population susceptible to get lost in (2,1) NTM scenarios. This can be explained as the ICRH heating transfers a population of passing fast ions with $\arccos(v_{\parallel}/v) < 30 - 40^\circ$ to a region of the phase space in which the (2,1) NTM transport mechanism is effective and therefore increases the losses of passing fast ions. Another experiment was performed to investigate the relationship of the NTM amplitude, the NBI heating and the subsequent fast ion losses. Fig.5.9 shows a twofold correlation of the fast ion loss rate with NBI blips as well as with the (2,1) NTM amplitude. The time scale of the additional NTM induced ion losses ($\approx \mu\text{s}$) due to NBI blips appears much shorter than the time the NBI source needs to achieve its maximum heating power of 2.5 MW (≈ 2 ms). A relationship between the fast ion loss rate and the (2,1) magnetic perturbation can be established only in *quiescent* (2,1) NTM discharges without interferences in the NTM growth phase e.g. ELMs. Fig.6.1.a shows in green the (2,1) NTM magnetic perturbation amplitude (B_θ) together with its corresponding fast ion losses, in blue, versus time during the growth phase of the perturbation. In order to eliminate the interferences introduced by e.g. ELMs or prompt losses the signals were filtered, obtaining the smoothed curves superimposed in the same figure. Fig.6.1.b shows the resulting relationship between both smoothed curves with clear quadratic dependence ($FIL \propto \delta B^2$). This quadratic behavior arises due to a diffusive process where non-resonant particles receive randomly phased perturbations of their orbits as they cross over the mode. This is in agreement with the suggested loss mechanism, orbit stochasticity. Moreover, here one has to note that the spikes of fast ion losses due to prompt losses induced by orbit stochasticity itself or ELMs have been eliminated

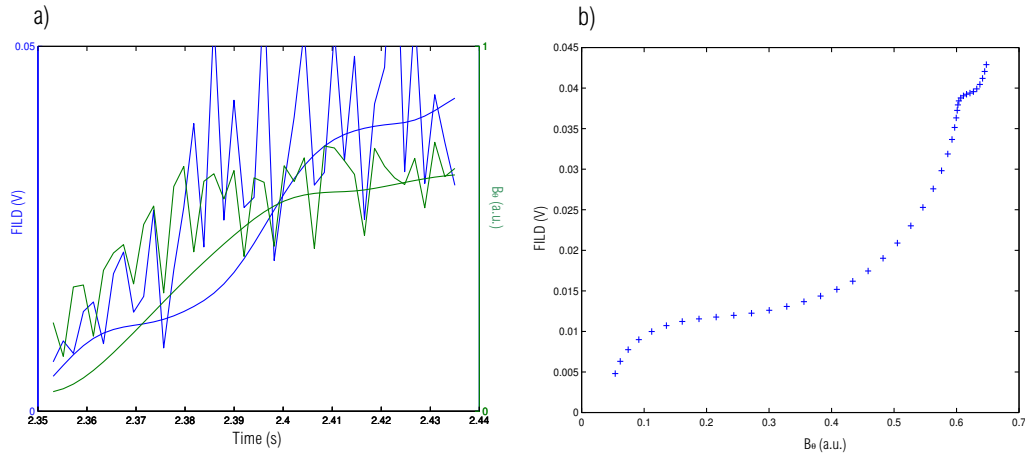


Figure 6.1: AUG Discharge 21118: Analysis of the relationship between magnetic perturbation (B_θ) and the fast ion loss rate (FILD). (a) Raw signals at the (2,1) NTM frequency together with their filtered curve. Note that they have different scales. (b) Fast ion loss rate versus magnetic perturbation amplitude.

by filtering the signal.

Experiments with (2,1) NTMs have revealed valuable information on the lost fast ion population, giving some hints towards a better understanding of the underlying loss mechanisms. Although energetic ion losses in NBI heated discharges with (3,2) NTMs present were identified, they could not be studied experimentally in detail during this work due to the ion collimator used. Ions with $E \leq 93$ keV and $\arccos(v_{\parallel}/v) \approx 30^\circ$ were not permitted by the collimator geometry. Further experiments will focus on this issue.

6.2.2 Numerical Simulations with ORBIT

The viability of orbit stochasticity as the transport mechanism responsible for fast ion losses in ASDEX Upgrade NTM discharges is discussed here. A brief introduction including the contributions of previous works was presented in the beginning of this section. The Hamiltonian guiding center code ORBIT [72] has been used to follow NBI ion trajectories in a magnetic equilibrium with (2,1) and (3,2) NTM magnetic perturbations [73]. In this section, the results obtained with a (2,1) NTM magnetic perturbation are introduced. The final goal of the simulations is to obtain a similar lost ion pattern to the one obtained in the experiments using realistic parameters. Since a complete numerical simulation is beyond the scope of this thesis, only the preliminary results, confirming the validity of orbit stochasticity as the transport mechanism for these ion losses are presented here. The simulations were performed using a magnetic equilibrium with circular cross section of the ASDEX Upgrade size. A birth population of fast ions with a single energy of 100 keV and pitch angles of $\frac{v_{\parallel}}{v} = 1$ is created and started on the high field side (HFS), being radially localized $\psi_p \in (0.009, 0.018)$ similar to a short beam pulse or blip. ORBIT is then used to follow fast ion trajectories without collisional effects in

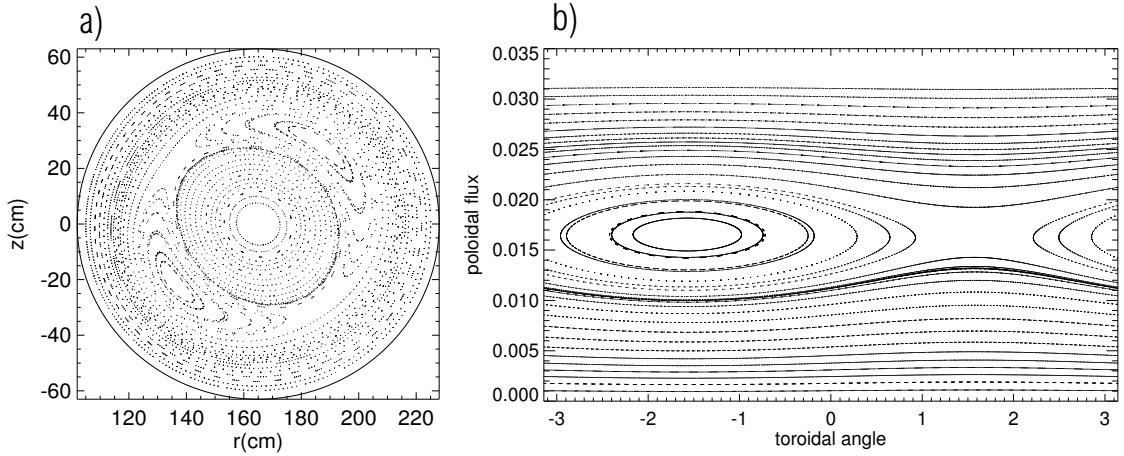


Figure 6.2: (2,1) NTM Poincare plot for ions with $E=0.0001$ keV. $R=165$ cm, $a=63$ cm, $\delta B_r/B = 1.3 \times 10^{-3}$ and $B_0 = 2$ T. (a) Poloidal projection. (b) Along the toroidal direction.

a perturbed magnetic field equilibrium. A simple analytical expression is used to model a non rotating (2,1) NTM. The non rotating perturbation simplified model is a reasonable approach since NTM magnetic islands appear frozen to the passing fast ions ($E = 100$ keV) due to their low rotation frequency ($\approx 10 - 30$ kHz). In the Hamiltonian formulation of guiding center motion a magnetic perturbation $\delta \mathbf{B}$ is introduced through a vector potential, $\delta \mathbf{B} = \nabla \times \delta \mathbf{A}$ with $\delta \mathbf{A} = \alpha \mathbf{B}$, where \mathbf{B} is the equilibrium field and $\alpha(x, \theta, \zeta)$ is a scalar function of position with $x=r/a$ as the radial variable and θ and ζ the poloidal and toroidal coordinates respectively. Here r is the minor radius along the outer mid plane ($r \approx \sqrt{2\psi_p/B}$). A simple model of a single MHD mode is assuming α to have a single helical component

$$\alpha(x, \theta, \zeta) = \alpha_0 \left(\frac{x}{x_0} \right)^m \left(\frac{1-x}{1-x_0} \right)^p \sin(n\zeta - m\theta) \quad (6.1)$$

where, x_0 is the radial coordinate at which the mode peaks, $q(x_0) = m/n$. However, as shown in the previous chapter and predicted by Mynick et al, additional helicities increase significantly the losses of fast ions.

The simulation presented here has been performed with a magnetic perturbation of $\delta B_r/B = 8 \times 10^{-4}$. The island width corresponding to this perturbation strength can be estimated directly by taking a Poincare puncture plot of low energy ions with $v_{\parallel}/v = 1$ which simply follow field lines. Fig.6.2 shows a poloidal and toroidal projection of the Poincare puncture plot for the magnetic field itself. A clear $m=2$ island is visible around the $q=2$ surface of a comparable size to a real one.

A Poincare puncture plot obtained following energetic ions ($E = 100$ keV) with pitch angles $v_{\parallel}/v = 1$ in the perturbed magnetic field is shown in Fig.6.3 along the toroidal direction on the High Field Side (HFS). Comparing this with Fig.6.2, one can note an important difference arising when the drifts are turned on. The appearance of an additional drift structure around the $q=3$ surface, predicted by the theory given in Chapter 2, overlaps with the (2,1) magnetic

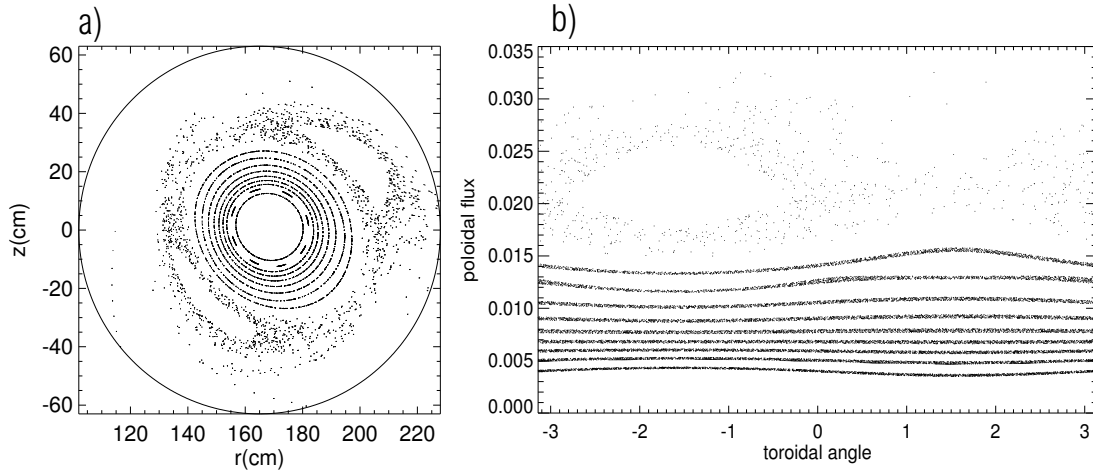


Figure 6.3: (2,1) NTM Poincare plot for passing ions with $E=100\text{keV}$. $R=165\text{cm}$, $a=63\text{cm}$, $\delta B_r/B = 1.2 \times 10^{-3}$ and $B_0 = 2\text{T}$. a) Poloidal projection. b) Projection at the Low Field Side (LFS) along the toroidal direction.

island, creating a stochastic region in the phase space. Additional substructures in phase space are generated by the drift orbits and the stochasticity itself. It is important to remark that the perturbation strength is strong enough to induce orbit stochasticity but not to induce magnetic stochasticity in the plasma core. Thus, such perturbation can produce a loss of energetic ions at perturbations at a fraction of the size needed to induce loss of the bulk plasma, as has been seen experimentally.

The initial fast ion spatial distribution was taken as a (ψ_p, θ) strip with a fixed theta and $\psi_p \in (0.009, 0.018)$ and along the whole ζ . The ions were started in the High Field Side (HFS) according to the most unfavorable scenario with fast ion losses observed in the presence of (2,1) NTMs. A significant loss of fast passing ions were observed in discharges heated by NBI sources with radial injection directions. In Chapter 4, the geometry of the AUG NBI2 sources was described, showing that radial sources produce mainly ions on trapped orbits but a fraction of them is always deposited in the HFS on passing orbits.

The distribution of loss times has been analyzed and is shown in Fig.6.4. It shows the lost particle probability density (dp/dt) as a function of the loss time due to a (2,1) NTM like perturbation. The lower x axis shows the loss time normalized to the toroidal transit time.

Integrating the lost particle probability density presented in Fig.6.4, one obtains the integral lost particle probability distribution, shown in Fig.6.5 as a function of the loss time for different mode phases. As expected for a non rotating (2,1) mode, the loss time distribution is independent of the mode phase. For a given value of loss time, the corresponding point of the curve provides the percentage of lost particles, which have been lost until that time. Obviously after a long enough run time all particles are lost, but it is important to note that about 50% of the particles are lost only after 0.1 ms. In order to have a better understanding of the process involved in the ejection of fast ions, single fast ions have been followed. Without perturbation it is trivial to understand that low energetic ions ($E \approx 0.001\text{keV}$) are tied to the field lines so that

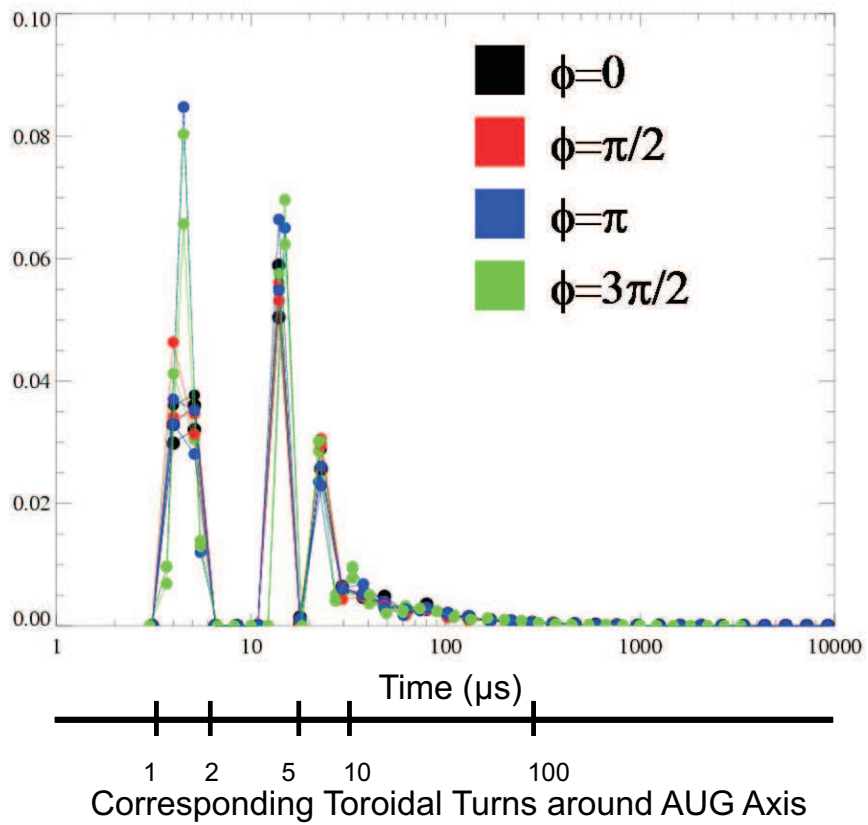


Figure 6.4: Lost particle probability density vs loss time for a NTM magnetic perturbation of $\delta B_r/B = 1.2 \times 10^{-3}$ and various mode phases. The x axis is drawn in logarithmic scale.

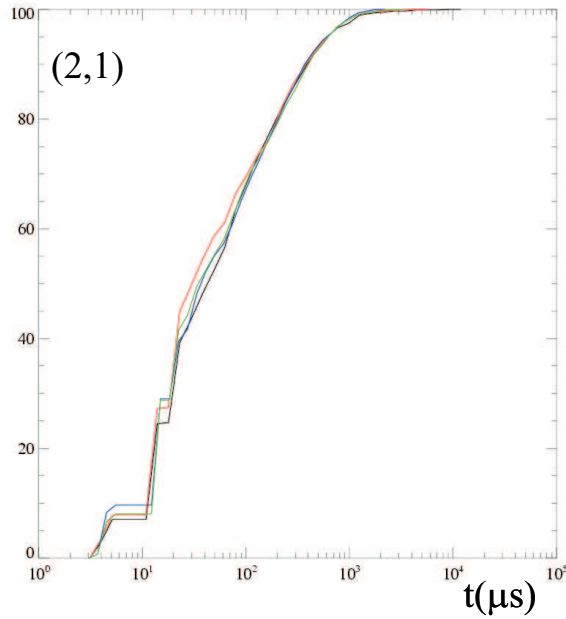


Figure 6.5: Integral probability distribution vs loss time for a $\delta B_r/B = 1.2 \times 10^{-3}$ (2,1) NTM magnetic perturbation and various mode phases. The x axis is drawn in logarithmic scale.

their trajectories describe the magnetic field equilibrium. High energetic ions ($E = 100\text{keV}$) follow the field lines but they are not tied to them anymore. Their large gyroradius gives rise to orbits shifted from the flux surfaces.

In the presence of a (2,1) NTM with a strength above the orbit stochasticity threshold, energetic passing ions due to their drift orbits follow a stochastic behavior as Fig.6.6 and Fig.6.7 show for two lost particles with different loss times. The first one, Fig.6.6, leaves the plasma in a straightforward loss stochastic drift orbit, while the second one, Fig.6.7, shows a stronger stochastic behavior, drifting randomly inwards and outwards until it leaves the plasma. These two lost ion trajectories represent the two characteristic times of the orbit stochasticity as loss mechanism. Therefore, orbit stochasticity is in a longer time scale a diffusive process ($\propto \delta B^2$) while it contributes as well to prompt losses.

The validity of orbit stochasticity as a loss mechanism of fast ions due to NTMs have been proven numerically using the ORBIT code in a circular ASDEX Upgrade magnetic equilibrium. Further work is required to compare in absolute values the (2,1) and (3,2) NTM induced fast ion losses with their respective measurements. For these upgraded simulations, a real ASDEX Upgrade magnetic equilibrium is necessary as well as the implementation in code of a simplified ASDEX Upgrade vessel geometry. In addition, a more accurate NBI deposition pattern should be used as an initial particle distribution function.

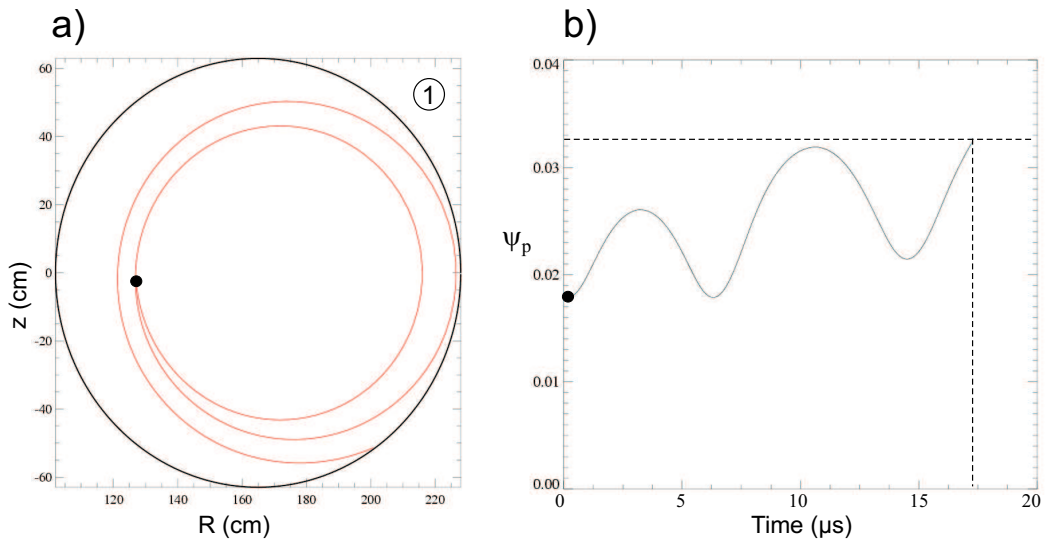


Figure 6.6: (a) Poloidal projection of the perturbed fast ion trajectory due to the orbit stochasticity induced by the (2,1) NTM magnetic island and the (1,0) fast ion drift orbit. (b) Radial drift versus time illustrating the prompt loss.

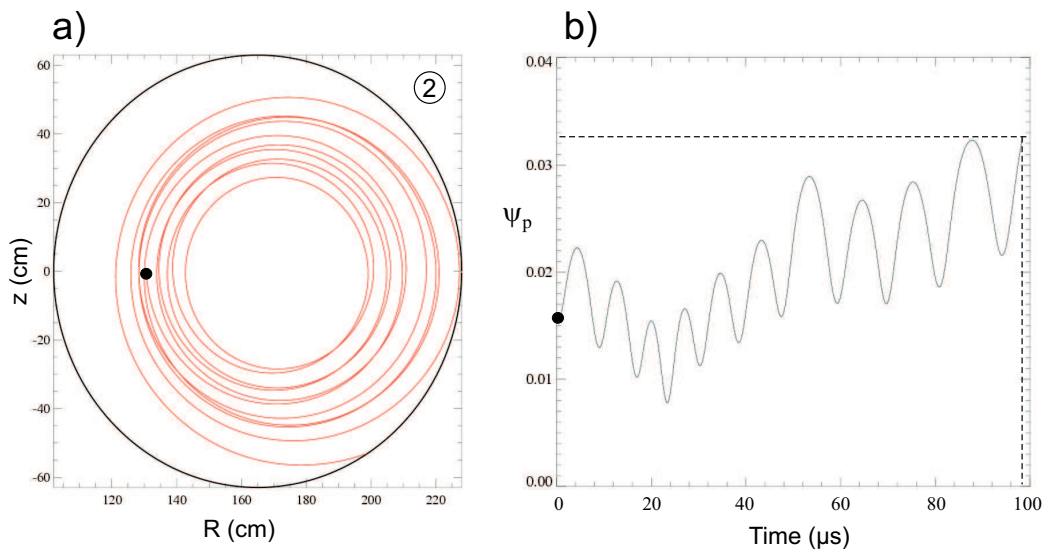


Figure 6.7: (a) Poloidal projection of the perturbed fast ion trajectory due to the orbit stochasticity induced by the (2,1) NTM magnetic island and the (1,0) fast ion drift orbit, particle 2. (b) Radial drift versus time, illustrating the diffusive character of orbit stochasticity.

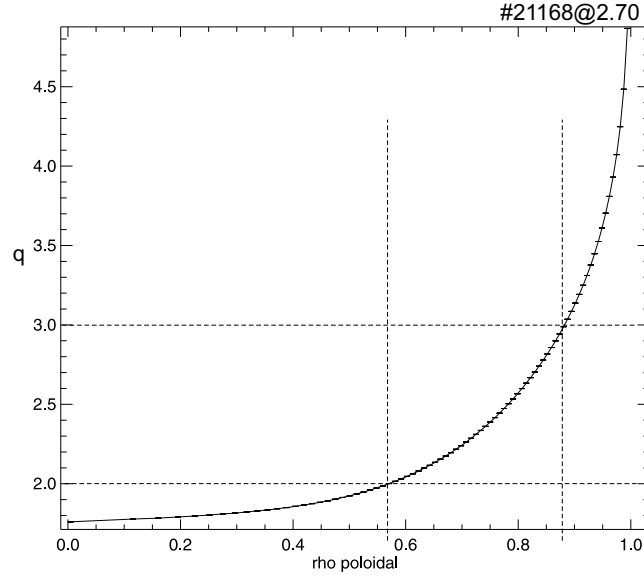


Figure 6.8: Radial q -profile of discharge 21168 at $t=2.7s$ calculated using the EQI magnetic field reconstruction produced by the CLISTE code. The radial locations of $q=2$ and $q=3$ are depicted by vertical dashed lines.

6.2.3 Island Overlap Estimation

The Chirikov criteria, [29] has been applied to various NTM discharges in order to estimate analytically the island overlap in phase space. The goal was to test the criteria itself, since the strong effect of orbit stochasticity ejecting fast ions has already been confirmed in the previous section.

An AUG typical (2,1) NTM magnetic island width of 100 mm has been considered for these calculations together with the specific q -profile of the studied discharges. The resulting estimation for discharge 21168 is shown here as a reference. Fig.6.8 shows the q -profile for discharge 21168 at $t=2.7s$. As shown in the previous chapter at this time point the observed fast ion losses due to a present (2,1) NTM magnetic island were very strong.

The theory, introduced in Chapter 2, predicts in addition to the primary island at the $q=2$ surface, two rings of drift islands of symmetry $m=1$ and $m=3$ around the $q=1$ and $q=3$ flux surface respectively in the particle phase space. The width of these drift islands, $\delta\rho_l$, in the particle phase space are connected to the magnetic island widths through

$$\delta\rho_l \approx \delta\rho \sqrt{|G_l(E, \varepsilon)|}, \quad (6.2)$$

where l denotes the island harmonic label ($l=0$ is the primary island, $l=\pm 1, \pm 2, \dots$, are sidebands) while G_l is the coupling coefficient defined by Mynick et al [49] and already introduced in the second chapter of this thesis. In particular, $G_0 \approx 0.95$, $G_1 \approx 0.25$ and $G_{-1} \approx -0.01$ for the case of $E \approx 93keV$ deuterium ions in a large aspect ratio tokamak. An overlapping between the primary and the sideband islands in the particle phase space is allowed by the criteria if

the drift island half-widths is greater than the distance between the centers of the drift islands. Since $q > 1$ for this discharge, only the $q=3$ drift islands are considered. The (2,1) NTM magnetic island is centered on the $q=2$ flux surface corresponding to a radial position in the discharge of $\rho(q=2) = 0.57$ with the typical AUG (2,1) NTM island width of $\delta\rho \approx 0.2$. The Chirikov island overlap criterion becomes for the $q=2$ and $q=3$ islands,

$$\frac{1}{2}\delta\rho \left(\sqrt{|G_0|} + \sqrt{|G_1|} \right) \geq |\rho(q=2) - \rho(q=3)|. \quad (6.3)$$

Considering the (3,1) drift islands, the sum of the drift island half-widths comes out to ≈ 0.15 , while the distance between flux surfaces gives $\rho(q=3) - \rho(q=2) \approx 0.31$. This means, the overlap criteria between both islands is not satisfied for 93 keV passing deuterium ions. This simple calculation indicates together with the measurements and the numerical simulations that the Chirikov criteria is not applicable for typical NTM discharges in ASDEX Upgrade.

6.3 TAE and Sierpes Induced Fast Ion Losses

Strong losses of fast ions have been observed correlated with high frequency MHD perturbations. The escaping fast ions have been measured in ICRH heated discharges with a minority heating scheme. Blips of NBI heating have been applied to investigate the changes in the fast ion loss pattern during H-L-mode transitions. As expected, in ICRH heated discharges, the main losses have been detected with high pitch angles ($\arccos(v_{\parallel}/v)$) and energies compared to the NBI system injection energies. Ions with such pitch angles are thought to be deeply trapped. Previous works on fast ion confinement, especially, α particle physics experiments in TFTR with DT discharges have revealed insights into the alpha particle confinement and wave-particle interactions [15]. MHD induced α loss have been observed in TFTR in the presence of various high frequency MHD activities like, kinetic ballooning modes (KBMs), sawtooth crashes and minor and major disruptions. However, a better understanding of the fast ion physics can be gained by studying the behavior of NBI or ICRH heated fast ions. The main advantage of the studies with externally heated fast ions against α particle experiments is the better control of fast ion distributions in plasma. Through the application of NBI and ICRH power, one introduces in plasma new anisotropies and inhomogeneities, as described in Chapter 4. These can, when the fast ion density is sufficient drive new instabilities and consequently lead to new sources of fast ion losses. The drive can come from $\partial f_f / \partial \psi$ (where f_f is the fast ion distribution function) and $\partial f_f / \partial E$. Where E is the particle energy and ψ is the radial (poloidal flux) coordinate. In the following sections, the results presented in the previous chapter are discussed, placing emphasis on issues that have not been well established in previous work up to now.

6.3.1 Identification of Fast Hydrogen and Deuterium Ion Losses

The identification of the lost species in discharges with ICRH heating is not a trivial issue being, in addition, of crucial importance to understand the underlying loss mechanisms, hence

it is discussed here in detail. Studies on JET have attributed the losses of fast ions in ICRH heated discharges to losses of ICRH accelerated hydrogen ions with high energies [74]. In the same way, experiments on TFTR [75] have reported losses of fast ions in ICRH minority heating discharges with TAE and Alfvén frequency mode (AFM) activity without giving any information on the lost fast ion species. As shown in Chapter 4, the ICRH minority heating schema accelerates at the fundamental harmonic mainly hydrogen ions, but it heats as well deuterium ions at the first harmonics, especially if the discharge presents already a high population of fast deuterium ions thanks to extra NBI heating. Two ICRH minority heated discharges have been presented in the previous chapter as reference for high frequency MHD induced fast ion losses, one of them with an additional short NBI phase. Both present two well, in gyroradius, separated spots at pitch angles $\arccos(v_{\parallel}/v) \approx 65^\circ$. The CCD sequence of discharge 21011 presented together with the deuterium and hydrogen neutral fluxes measured by the CX diagnostic certifies that both these spots correspond not to deuterium ions with two different energies but to hydrogen and deuterium ions with similar energies. At toroidal magnetic field $B_t = 1.57T$ on the probe location, the energy of a deuterium ion with a gyroradius of 70 mm is the same as the one of a hydrogen ion with a gyroradius of 50 mm, $E_D(R_L = 70mm) = E_H(R_L = 50mm) \approx 300keV$. The fact that the hydrogen pattern appears always weaker and more localized in phase space than the deuterium one can be explained in a first approach by the better energy resolution of the ion collimator at smaller gyroradius and by the larger banana width of deuterium ion orbits. Ions on wider banana orbits need shorter outwards radial transitions to leave the plasma. Once, the origin of two spots at almost the same pitch angles has been clarified, the study of the loss mechanisms can begin with a more accurate information. In principle, the loss mechanism does not have to be the same for hydrogen and for deuterium ions. The next step to explain the corresponding ion loss mechanisms is to discover which magnetic perturbations lie behind each kind of losses. A Fast Fourier Transform (FFT) has been applied to the channels corresponding to the hydrogen and deuterium lost ions.

The sliding FFT of the 13 FILD channel which covers the spot at larger gyroradius, as shown in the previous chapter, reveals the contribution of two dominant magnetic perturbations in different frequency ranges to the fast deuterium ion losses. On the other hand, an FFT analysis of the 9 FILD channel which covers the area corresponding to lost energetic hydrogen ions (smaller gyroradius), shows only the upper frequencies. Both frequency spectrograms are shown in Fig.6.9

The signals at higher frequencies can be easily identified as TAEs, comparing their behavior in the frequency spectrogram with the Alfvén velocity evolution and the Mirnov Pick-Up coil spectrogram. Both, the Mirnov spectrogram and the Alfvén velocity evolution of each fast MHD discharge are plotted in the previous chapter. In addition to this, channel 13 shows a new frequency ($\approx 80kHz$) which has been attributed to a new magnetic perturbation, called *Sierpes mode* in the previous chapter. Fast ion losses at this frequency have been detected in FILD with an even stronger contribution to the losses than the TAEs. This new magnetic perturbation is rather not visible in the Mirnov coil signal for discharge 21011 and visible but very weak and blurred during discharge 21083. From the fact that this new frequency is rather not visible by the Mirnov coils but very clear in the FILD signals one can postulate that the Sierpes mode

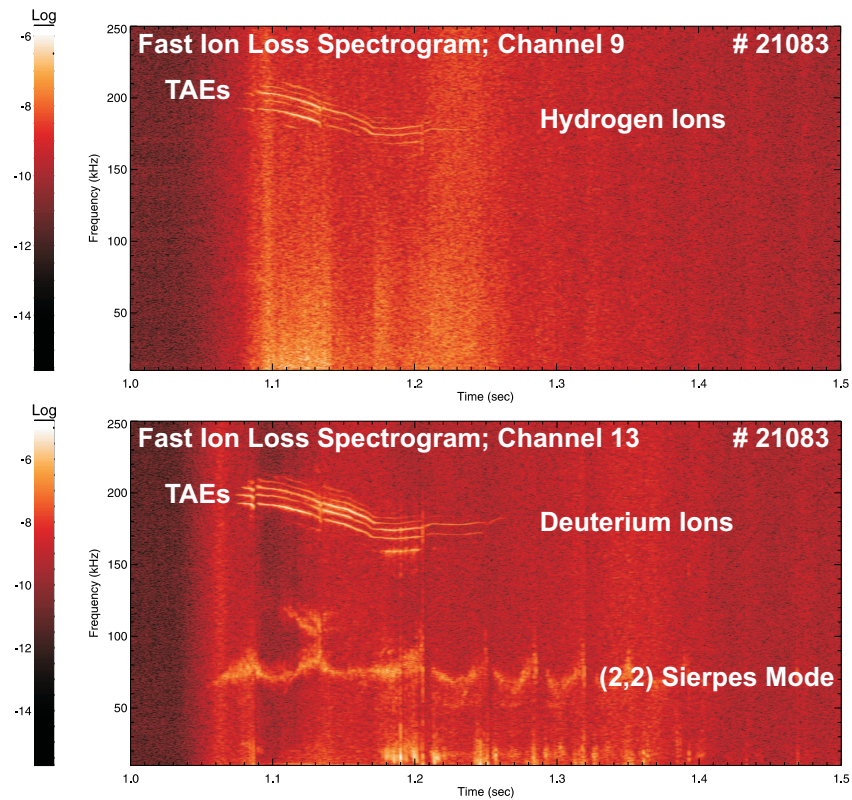


Figure 6.9: AUG Discharge 21083: Frequency analysis of the FILD channels 9 and 13. Each channel covers one of the spots shown for the discharge 21011 in the previous chapter. Channel 9 covers the hydrogen spot while channel 13 corresponds to the deuterium spot.

HAGIS Equilibrium

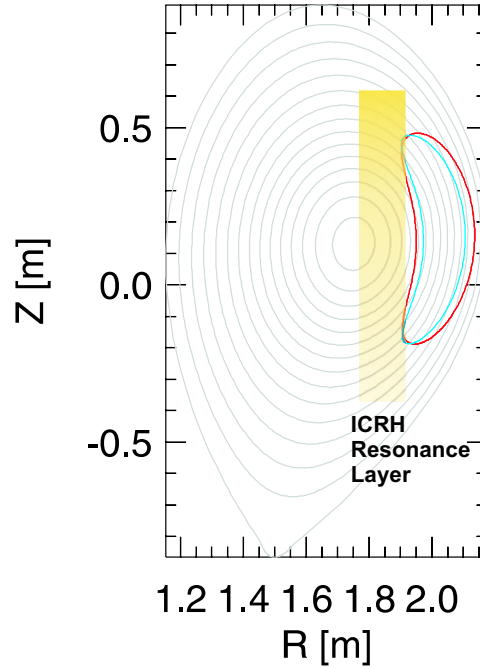


Figure 6.10: Numerical simulation. Poloidal projection of two fast ion banana orbits with the same energy, $E = 500keV$, and pitch angle, $\arccos(v_{\parallel}/v) = 79^{\circ}$, but different mass: hydrogen in blue and deuterium in red.

is an MHD perturbation localized deep in the plasma core. However, this is not the case for deeply trapped energetic ions which suffer from the interaction with the perturbation on such a width banana orbit that they get lost preserving the frequency information due to the relative small AUG plasma radius (comparable to the banana orbit widths). As a consequence of this, only energetic deuterium ions on wide banana orbits can interact with the mode during the whole outwards radial drift leaving so the plasma. The banana wide of trapped hydrogen ions is a factor of $\sqrt{2}$ smaller than the deuterium ion ones with the same energy and pitch angles and therefore higher fluxes of lost deuterium ions are expected, see Fig.6.10.

In particular, in the presented discharges, hydrogen ions are ejected from the plasma due to interactions only with TAEs. Since TAEs are localized radially more outside ($q \approx 1.5$) than the Sierpes mode ($q \approx 1$) they can interact with hydrogen ions of $E \approx 300keV$ and pitch angles of $\arccos(v_{\parallel}/v) \approx 65^{\circ}$ during the whole ion transit along the minor radius to FILD. Hydrogen ions are heated by the ICRH system up to high energies ($E \approx 300keV$) while they pass through the ICRH resonance layer. Well inside the plasma core they can interact with the Sierpes mode, but as soon as they start to drift outwards due to the Sierpes mode they leave completely the influence area of the magnetic perturbation, the $q=1$ magnetic surface. The radial transport due to the Sierpes mode disappears, but the amount of energetic hydrogen ions outside the $q=1$ surface has been increased drastically. A huge amount of energetic hydrogen ions is then available outside the $q=1$ surface as a driving force to trigger and maintain the TAEs. At the

same time a part of these energetic hydrogen ions, well outside the $q=1$, can leave the plasma due to interactions with the existent global TAE modes.

Deuterium ions have been observed leaving the plasma with two dominant frequencies, the Sierpes and the TAE frequencies but also due to fishbones and sawtooth. The wide banana width of the measured lost deuterons with energies between 300 and 600 keV and pitch angles of $\arccos(v_{\parallel}/v) \approx 65^{\circ}$ enables their interaction with all the magnetic perturbations in plasma, from the deep core to the edge. Therefore, the Sierpes mode contributes strongly to the ejection of fast deuterium ions though it is far away from FILD. As a consequence of the global radial presence of TAEs, high fast ion fluxes are expected. However, higher fluxes of deuterium ions have been measured at the Sierpes frequency than at the single TAE frequencies indicating the strong deleterious character of the Sierpes mode in fusion devices with relative small distance between the $q=1$ surface and the vacuum vessel wall compared to the large banana width of the energetic deuterium ions. This could be extrapolated to fusion reactors and the expected large banana widths of tritium ions and α particles, however further works are necessary to evaluate this issue.

6.3.2 Fast Ion Loss Rate due to TAEs and Sierpes

A linear relationship between the TAE amplitude and the fast ion loss rate has been reported in various works from the DIII-D and the JET tokamaks, [23], [25] and [76] suggesting that the loss is due to a process that is coherent in nature, rather than diffusive. In order to make an assertion on the relationship between the TAE amplitude and the fast ion loss rate, one has to know the origin of the fast ions not only from the area of influence of the TAE, but also before the ions enter into this area. This section tries to establish a relationship between the observed fast deuterium and hydrogen ion loss rate and the amplitudes of the TAEs and the Sierpes mode. In general, TAE induced fast ion losses are independent of the TAE mode numbers but as expected strongly dependent of the TAE amplitude, see Fig.6.12 and Fig.6.13. However, a direct relation between the single TAE magnetic perturbation amplitude and the corresponding fast ion loss signal cannot be easily established due to the strong contribution of the Sierpes mode. Fig.6.11 summarizes the measurements obtained in discharges with TAEs and Sierpes modes present. The simultaneous presence of TAEs and Sierpes induced fast ion losses is the most common scenario observed in the performed discharges e.g. Fig.5.17 or Fig.5.27. In these scenarios, TAEs have always been observed in the Mirnov coil signals. However, the presence of TAEs detected by the Mirnov coils does not imply the ejection of fast ions at least while the Sierpes mode does not appear in FILD. In fact, very weak fluxes of fast ions have been detected by FILD in discharges without Sierpes activity, see Fig.5.17 at $t=1.8s$. The Sierpes mode presence detected by FILD in discharges with TAE magnetic perturbations implies the expulsion of fast ions by the single TAEs during the whole TAE *stationary* phase. Obviously, no TAE induced fast ion losses have been observed without identifying the TAEs in Mirnov coil signals. However and as a consequence of the mode location, Sierpes induced fast ion losses have been observed without detecting any magnetic perturbation with this frequency at the Mirnov coils, Fig.5.17. Finally, Fig.6.11 shows the trivial case in which no MHD activity

TAEs in Mirnov	TAEs in FILD	Sierpes in FILD	Comments
✓	✓	✓	Most common
✓	✓	✗	Without Sierpes, TAEs marginal in FILD
✓	✗	✗	Observed
✓	✗	✓	Not Observed
✗	✓	✓/✗	Not Observed
✗	✗	✓	Observed
✗	✗	✗	Quiescent Plasmas

Figure 6.11: Measurement overview. Presence of TAEs and Sierpes in both Mirnov coils and FILD.

is observed neither by FILD nor by the Mirnov coils.

According to this complicated scheme, TAE induced fast ion fluxes appear always connected to those due to the Sierpes mode and therefore a relation between TAE magnetic perturbation strength and their corresponding fast ion loss rate can not be established. Fig.6.12 shows the amplitude analysis of a single TAE magnetic perturbation, on the left, and its corresponding fast ion loss fluxes in a discharge with a weak Sierpes effect on the right. Although, Sierpes induced fast ion losses appear weakly in FILD, the amount of fast ion losses due to the single TAE appears always strongly related to the Sierpes effect, Fig.5.19. As a consequence, despite the fast ion losses shown on the right are obviously due to their interactions with the TAE, a direct correlation with the magnetic perturbation strength is not possible.

Fig.6.13 confirms this critical assertion, following the maximums presented by the magnetic perturbation and the fast ion loss signal. For instance, the TAE magnetic perturbation shows a *weak* maximum between $t=1.07s$ and $t=1.09s$ which corresponds also with a maximum in FILD but much more pronounced due to the Sierpes effect, which is feeding the TAE with fast ions.

In order to identify the loss mechanisms involved in the ejection of fast ion losses due to TAEs and Sierpes, one has to note that no threshold in the magnetic perturbation strength has been detected for the fast ion expulsion.

Finally, it is important to remark that although the studied discharges were performed with ICRH minority heating, stronger fluxes of high lost energetic deuterium ions have been observed. This is an evidence, first of the high sensitivity of FILD and second of the efficiency of ICRH harmonic heating which as described in Chapter 4 is the main responsible for the fast deuterium ions in a minority heating scheme.

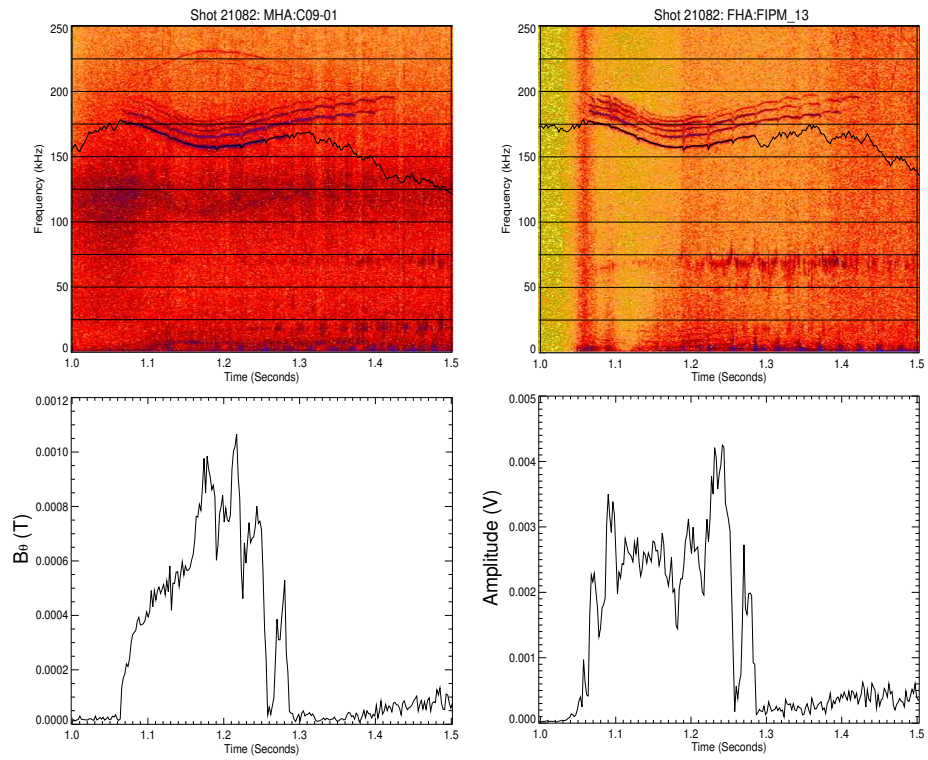


Figure 6.12: AUG Discharge 21082: Amplitude analysis of both TAE magnetic perturbations, left, and TAE induced fast deuterium ion losses, right.

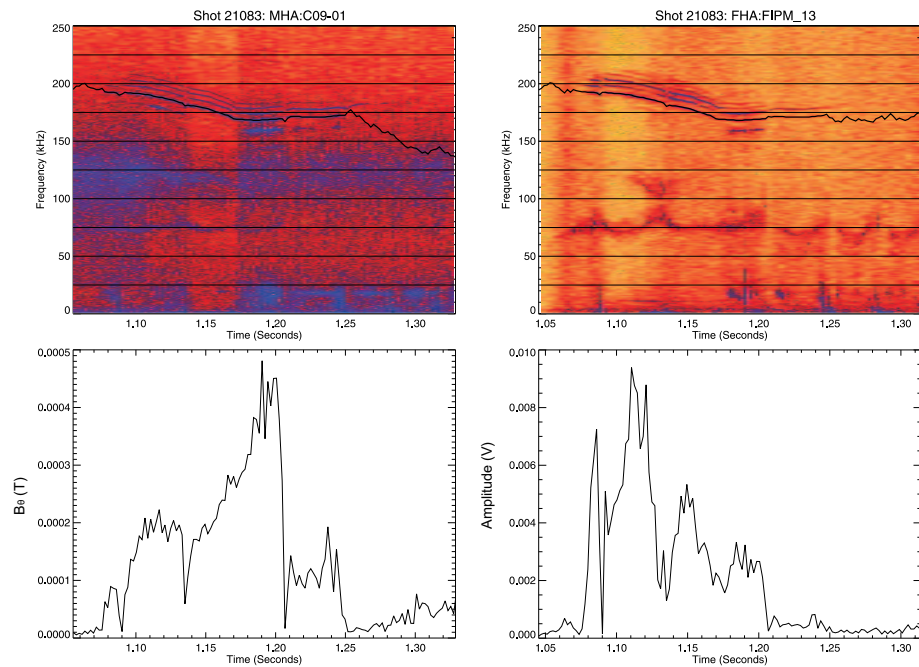


Figure 6.13: AUG Discharge 21083: Amplitude analysis of both TAE magnetic perturbations, left, and TAE induced fast deuterium ion losses, right.

6.3.3 The Sierpes Mode

The combined effect of TAEs and $q=1$ Energetic Particle Modes (EPMs) on fast ion confinement towards sawtooth stabilization has been studied in DIII-D [77]. A detailed measurement of the q profile with the MSE diagnostic in DIII-D enabled the identification of a chirping Alfvén instability observed during ICRH heating as EPMs. The EPMs were shown to be the leading cause of the monster sawtooth crash. It was also shown that TAEs are excited either directly or indirectly by the EPMs causing significant losses of fast ions. A coupling between the EPMs and the TAEs was proven, showing the same toroidal mode numbers, n , and similar frequencies for both modes, but always without frequency coupling. A similar MHD scenario is presented here with the appearance of a new mode, the Sierpes mode, which as shown before correlates clearly with TAEs and their subsequent MHD induced fast ion losses. The Sierpes mode appears to originate near the center of the discharge where the fast ion tail is formed by the ICRH system and it is seen only extremely weak by the Mirnov coils while localized in the core. As the mode grows up towards the edge, it carries with itself more fast ions and as a consequence it appears stronger in the FILD signals and eventually it is detected clearly by the Mirnov coils. Such MHD perturbation is particularly deleterious because it transports fast ions towards the edge and as it was shown in the previous chapter with a more virulent behavior than single TAEs.

A measurement of AUG density shows a weak correlation with the mode frequency behavior. However a direct and clear correlation cannot be presented due to limited accuracy of the density measurements at the $q=1$ surface, see Fig.6.14. Suggesting the location of the Sierpes mode at the $q=1$ surface is that it disappears right after the Sawtooth crashes, $n=m=1$ mode, until the fast ion tail has enough time to reform and exceed the threshold to trigger again the Sierpes mode. This can be seen by looking at the frequency evolution between Sawtooth crashes together with the T_e measurement close to the $q=1$, see Fig.6.14. Immediately after the crash the mode disappears, appearing again around 50 ms later with a similar frequency but decreasing in frequency rapidly due to density peaking. At this point it is important to remark that the Sawtooth crash coincides always with the frequency rise interruption of the Sierpes mode.

In order to localize the mode, to get an idea of its eigenfunction and to understand the hidden character of the mode within the magnetic pick-up coils, various channels of the Soft X-Ray (SXR) diagnostic were checked. The resulting radial position of the mode leads to a core localized mode at the $q=1$ surface. The spectrogram of one of the most core localized SXR channel in ASDEX Upgrade, SXB:J49, is shown in Fig.6.14. As expected, TAEs are rather not visible so deep in the plasma core whereas a clear activity is observed on the SX channels around 80 kHz, getting interrupted by sawtooth crashes.

The analysis of the m mode numbers was performed studying the amplitude of all the core SXR sight lines with appreciable signal at the dominant frequencies [78]. The structures shown in Fig.6.15 correspond to two (1,1) modes at relative low frequencies, 26 and 43 kHz while the Sierpes mode shows a structure typical of an $m=2$ mode. The n mode numbers were inferred from the orientation of the SXR sight lines (inside $q=1$) and the relation, $q=m/n$. The $m=2$ structure of the Sierpes mode was particularly difficult to obtain because of its frequency

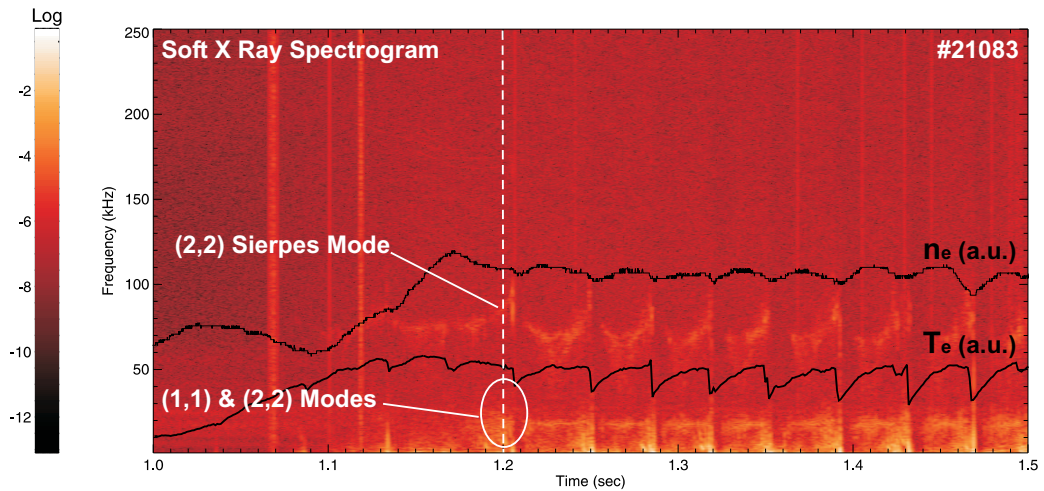


Figure 6.14: AUG discharge 21083: Frequency analysis of the SXR channel J49. In white the present magnetic perturbations are depicted. The vertical dashed line indicates the time point at which the mode structure analysis was done. The electron density and core electron temperature (AUG ECE 54 channel) are also superimposed.

spread.

Assuming the $q=1$ surface as the Sierpes mode location, a growth of the magnetic surface due to a change in the q -profile explains the TAE vanishment while the Sierpes mode persists. Discharge 21083 presents the simultaneous activity of TAEs and Sierpes from $t=1.07s$ until $t=1.26s$ while in a later phase, until $t=1.4s$, only the Sierpes mode remains in plasma. As a consequence of the change in the q -profile, the $q=1$ surface lies closer to the q_{TAE} causing a depletion of the TAE driving force, fast ions, by the Sierpes magnetic perturbation. The relationship of the Sierpes mode frequency and amplitude with RF power will be investigated in future work.

6.3.4 Loss Mechanisms and HAGIS Numerical Simulations

The mechanisms responsible for the radial transport and loss of fast ions due to TAEs have been investigated in the last years. In the early 80s, R.White et al [27] introduced already with his theory of fishbone mode induced beam particle loss, the resonant wave-particle mechanism most widely accepted up to now for trapped ion losses.

The HAGIS [39] code was used to model the effect of TAEs on the confinement of ICRH heated ions in ASDEX Upgrade. It can handle AUG magnetic equilibria as well as non-axisymmetric magnetic field perturbations following fast ion guiding centre orbits calculating the effect MHD modes have on the energetic ion trajectory. For realistic simulations, an EQI numerical equilibrium was employed together with an MHD activity model based on experimental observations. In ASDEX Upgrade, a high variety of (m,n) TAEs has been observed in discharges with high fluxes of fast ion losses. A single $(m,n)=(5,3)$ TAE mode has been implemented in Hagis. The vector of the perturbed magnetic field is described by the formula

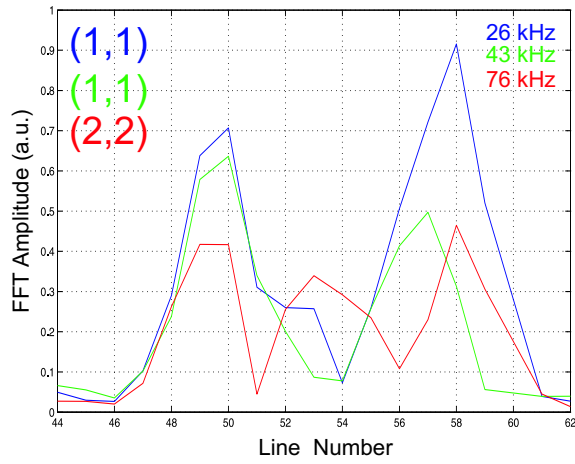


Figure 6.15: AUG discharge 21083: Mode structure study using the I Soft X Ray system of AUG at t=1.2s.

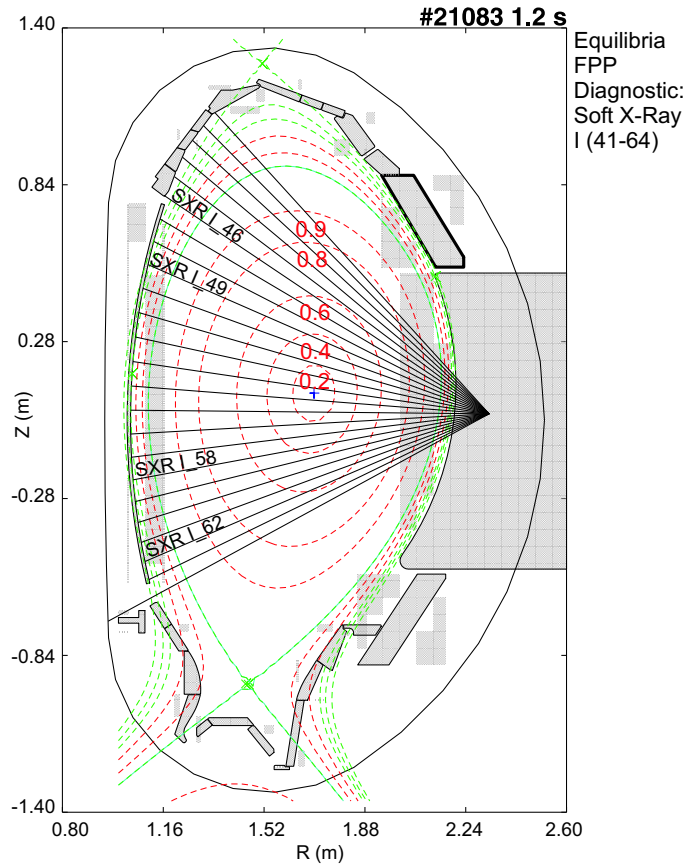


Figure 6.16: AUG discharge 21083: Sight lines of the Soft X Ray System, I Channels. The $\rho_{poloidal}$ surfaces are indicated together with some SXR channels as reference.

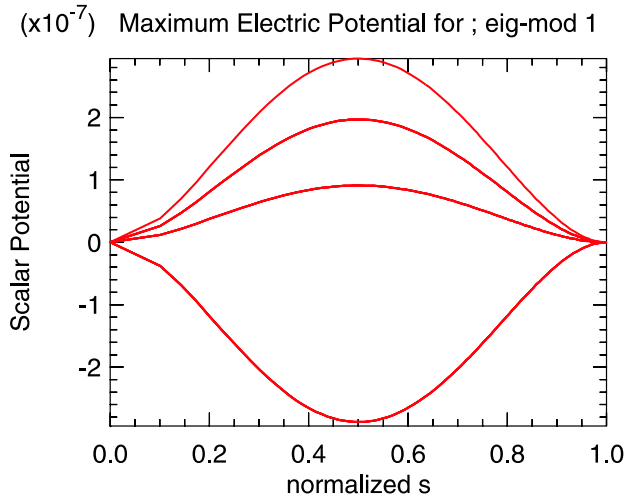


Figure 6.17: Radial Eigenfunction calculated analytically given for the (5,3) TAE mode at different poloidal angles.

$\delta\mathbf{B} = \nabla \times \alpha\mathbf{B}$, where the scalar function α is approximated in a simple manner consistent with the TAE mode radial profile, see Fig.6.17. The figure shows the radial eigenfunction taken to model the global character of typical TAEs evaluated at various poloidal angles.

A magnetic perturbation amplitude of $\delta B/B \approx 10^{-3}$ was chosen, according to experimental observations using the Mirnov coils. As shown in the previous chapter, usual TAEs are observed in ASDEX Upgrade with frequencies of $f_{TAE} \approx 150 - 200 kHz$. The (5,3) TAE model was implemented in Hags with a frequency of $f = 167 kHz$. The simulation was performed following fast deuterium ion trajectories with the parameters $(E, \arccos(v_{\parallel}/v))$ measured by FILD. A slight correction on the ion pitch angles has been performed to take into account that the pitch angle measured by FILD is not exactly the same as the ion pitch angle well inside the plasma since $E_{\perp} \approx \mu B \approx 1/2mv_{\perp}^2$ and $B \propto \frac{1}{R}$. To determine the initial fast ion population, first of all one has to study the effect of the ICRH system heating bulk deuterium ions. Fig.6.18 shows the trajectory changes of a deuterium ion while it is accelerated by the ICRH system. In the beginning, a passing bulk ion ($E= 5 keV, \arccos(v_{\parallel}/v) = 10^{\circ}$) is accelerated in the perpendicular component of the velocity. As a consequence, the passing ion gains perpendicular energy becoming trapped. The second trajectory plotted in Fig.6.18 shows the next stage of the ICRH acceleration process, a barely trapped deuterium ion with ($E= 30 keV, \arccos(v_{\parallel}/v) = 63^{\circ}$). The arrows on the banana tips show the direction in which the ICRH system pushes the whole banana orbit during the heating process. This is illustrated in the following two ion trajectories; trapped ions with ($E= 200 keV, \arccos(v_{\parallel}/v) = 75^{\circ}$) and ($E= 300 keV, \arccos(v_{\parallel}/v) = 79^{\circ}$). As the ion gains energy, its banana orbit gets broader but simultaneously is pushed radially outwards by ICRH heating. This process leads to an enhancement of the TAE induced fast ion losses since the ICRH heating has created a huge population of deuterium ions on wide trapped orbits with their banana tips close to the q_{TAE} .

The trajectories of trapped ions with ($E= 300-500 keV, \arccos(v_{\parallel}/v) = 65 - 80^{\circ}$), have been studied with and without the (5,3) TAE magnetic perturbation for some ion turns around AS-

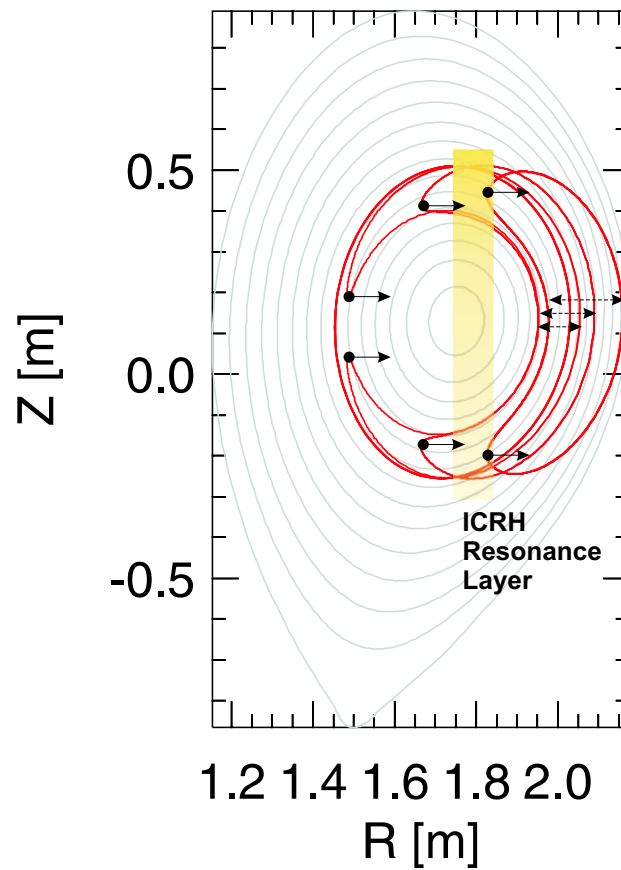


Figure 6.18: Enhancement of fast ion losses due to ICRH heating. The ICRH heating of a passing orbit converts it into a barely trapped ion. A continuous perpendicular heating of the ion on a banana orbit pushes its banana tips radially outwards and thus is contributing to the losses.

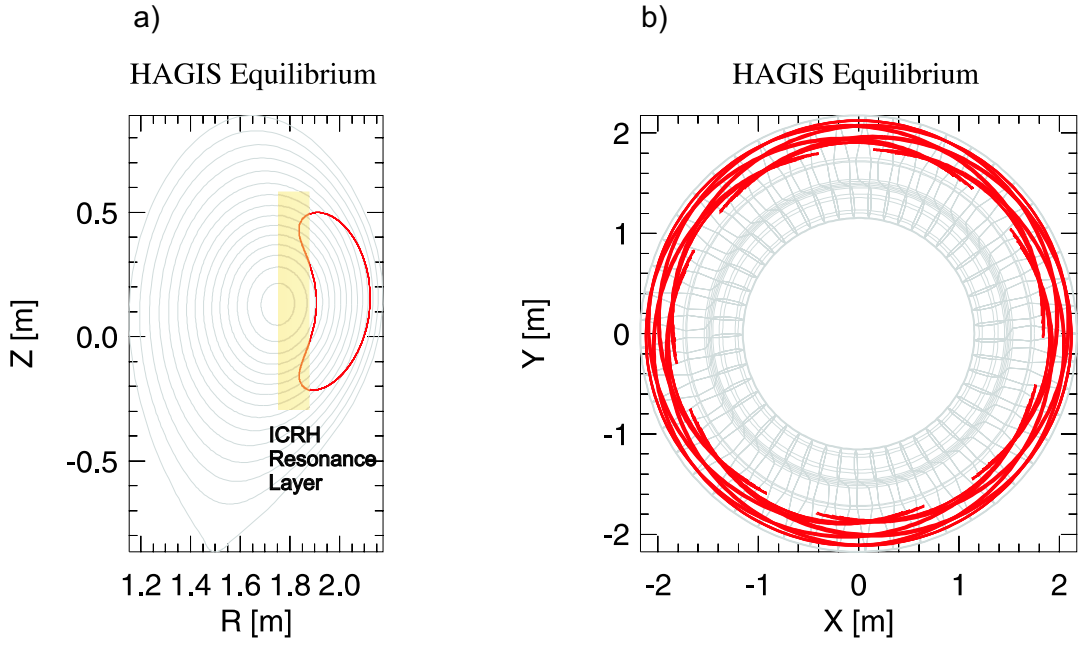


Figure 6.19: Numerical simulation: (a) Poloidal projection of the unperturbed ICRH heated fast ion orbit. Fast ion with 500 keV and a pitch angle, $\arccos(v_{\parallel}/v) = 79^{\circ}$. The ICRH resonance layer is depicted in yellow. (b) Toroidal projection of the unperturbed orbit.

DEX Upgrade. The resulting trajectory without magnetic perturbation is presented in Fig.6.19 for a deuterium ion with ($E= 500$ keV, $\arccos(v_{\parallel}/v) = 79^{\circ}$). As expected an unperturbed ICRH heated ion orbit will always remain in plasma. Fig.6.19 shows on the left, a poloidal projection of the ion orbit with its banana tips in the ICRH resonance layer. On the right, a toroidal projection of the ion orbit is shown.

As soon as the (5,3) TAE magnetic perturbation is switched on, the deuterium ion starts to drift outwards on its banana orbit. Fig.6.20 shows on the left the poloidal projection of the banana orbit during its outwards drift until it leaves the plasma after 1.5×10^{-4} s on its outer banana leg. On the right, a toroidal projection of this escaping deuterium ion is shown. The perturbation $\delta B/B$ and A_{\parallel} seen by the deuterium ion during the resonance time with the magnetic perturbation is outlined in Fig.6.21. It is clear that the effective perturbation seen by the ion depends on the banana leg in which the ion is at each time point as well as on the phase shift between ion and mode, being the perturbation sometimes positive or negative. It is important to place an extra emphasis on this last point since the change in the angular momentum of the resonant ions has to be always positive as Fig.6.22.a shows to have an effective ion ejection. Only in this case the outwards radial drift of the banana orbit will be always positive.

Fig.6.22.b shows the radial drift of the resonant ions versus the time spent in resonance with the perturbation to leave the plasma.

The total change in resonant particle angular momentum depends strongly on the magnetic perturbation strength, but also on the phase shift between ion and perturbation. In general, the wave-particle resonance condition in the plasma frame can be written as [74]

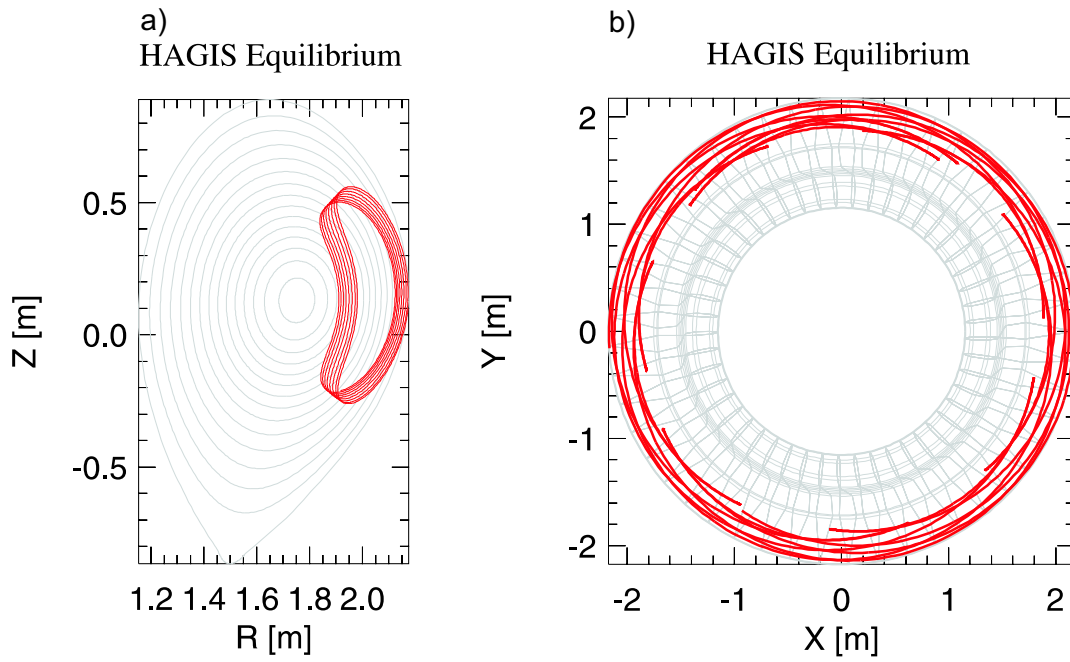


Figure 6.20: Numerical simulation: (a) Poloidal projection of the resonant orbit. (b) Toroidal projection of the resonant orbit.

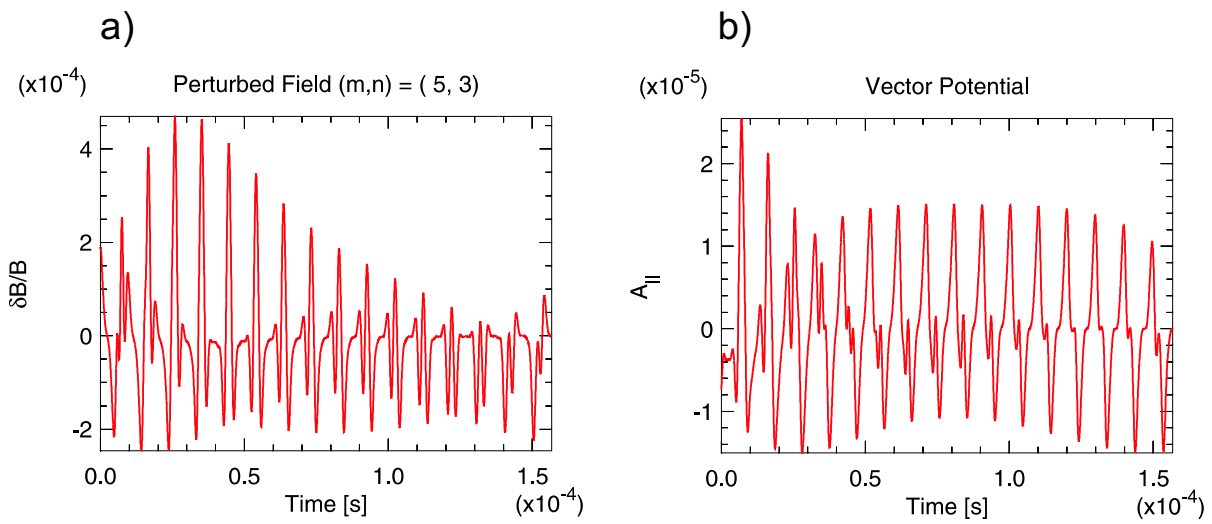


Figure 6.21: Numerical simulation: (a) Magnetic perturbation seen by the resonant ions during the escaping time. (b) Vector potential $A_{||}$ seen by the ion.

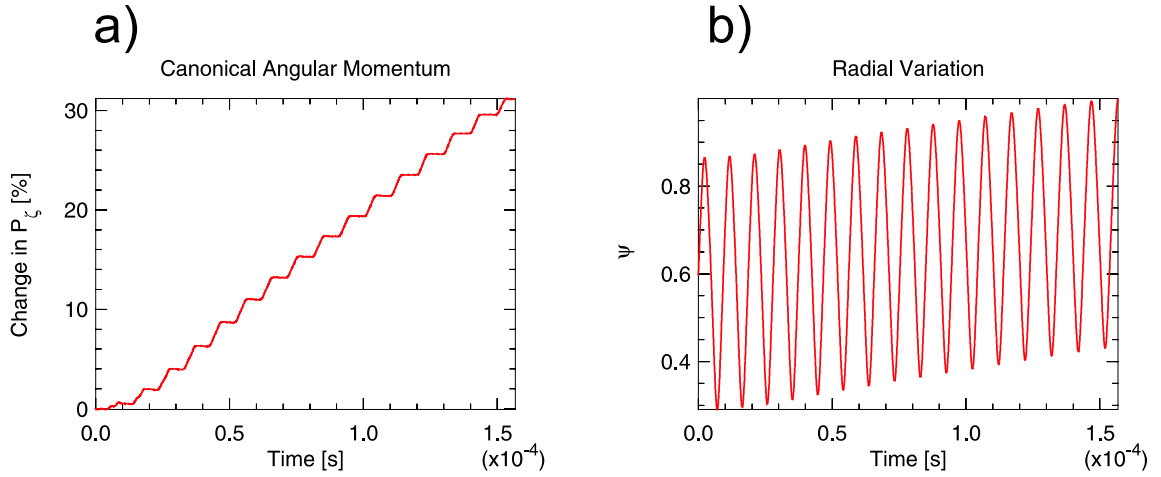


Figure 6.22: Numerical simulation: (a) Change in particle canonical momentum during resonance time. (b) Outwards radial drift of the resonant particle.

$$\Omega_{np} = n f_{prec} - p f_{bounce} - f_{MHD} \approx 0 \quad (6.4)$$

where n is the toroidal mode number, p is the bounce harmonic, f_{prec} the precession frequency of the trapped orbit, f_{bounce} the bounce frequency, and f_{MHD} the wave frequency. The simulations presented here results in a simplification of this resonance condition for the lost fast ion and TAE parameters obtained experimentally during a set of AUG discharges e.g. 21011 or 21083. The precession frequency of the ion shown in Fig.6.20 is $f_{prec} \approx 58kHz$ with a bounce frequency $f_{bounce} \approx 105kHz$. Since the (5,3) TAE mode was taken with an $f_{TAE} \approx 167kHz$, the resonance condition becomes $\Omega_{3,0} = 3 \cdot 58 - 0 \cdot 105 - 167 \approx 7kHz$. This means, the dominant resonance in this loss mechanism occurs at the main bounce harmonic ($p=0$). Simplifying the previous resonance condition, it becomes

$$n \cdot f_{prec} \approx f_{TAE}. \quad (6.5)$$

The frequency mismatching of $\Omega_{3,0} = 7kHz$ is inside the resonance width predicted by S.-D. Pinches et al [74]. A mismatch in wave-particle frequencies broader than the actual resonance width makes possible the change in canonical momentum in both directions, positive and negative, so that the banana orbit makes shorter radial drifts sometimes outwards and sometimes inwards, depending on the perturbed fields that the ion is feeling, but without leaving the plasma.

An important consequence that can be inferred from this resonance condition and the experimental results shown in the previous chapter with externally imposed magnetic perturbations like beat waves is the application of such controllable magnetic perturbations to remove a desired fast ion population from a location in plasma or eventually even totally from plasma e.g. Helium ashes.

Chapter 7

Summary

The development of a new diagnostic for the study of fast particle-wave interactions in ASDEX Upgrade as well as the interpretation of the first measurements have been the aim of this thesis. The results obtained during the first operation campaigns have provided new insights and challenges in the physics concerning charged particle-wave interactions. In general, the interpretation of the data is a complicated issue due to ion orbit shadow effects of in-vessel components and the high variety of MHD events present in the studied plasmas. In this section the main findings achieved during this work are summarized.

- The first goal of this thesis was the development of a scintillator based detector for MHD induced fast ion losses. The detector head was designed for the detection of fast ions with a gyroradius between 20 and 120 mm and pitch angles ($\arccos(v_{\parallel}/v)$) between 20° (passing orbits) and 87° (deeply trapped orbits). The main discovery of this phase of the work was the scintillator material used for the ion detection. This ultra fast scintillator material presents a decay time of $\approx 500\text{ns}$ with a very high luminous efficiency compared to other scintillator materials already utilized in fusion applications.
- The very short decay time of the scintillator together with the optimized ion collimator energy and pitch angle resolution have allowed the identification of fast ion losses due to a high variety of MHD phenomena during the first operation campaigns. A list of the main fast ion-MHD mode interactions observed in ASDEX Upgrade is shown in Table 7.1 ordered in terms of their characteristic frequencies. FIL due to harmonics of the main magnetic perturbation e.g. NTMs were measured even when these harmonics were not detected by the Mirnov coils.
- A new MHD perturbation, called *Sierpes* mode, has been observed for the first time during this thesis by means of its strong influence on the energetic deuterium ion population, see Table 7.1. This mode is localized in plasma core and dominates the transport of fast ions in ICRH heated discharges. Fast hydrogen ions are redistributed from the core toward the edge while deuterium ions are directly ejected to the wall due to their larger banana width.

Interactions	Frequency Range (kHz)	Ion Loss Pattern
Disruptions	$\ll 1$	whole phase space
Locked modes	$\ll 1$	passing D ions
ELMs	1	whole phase space
(2,1) NTMs in NBI heated discharges	5-15	passing D ions
(3,2) NTMs in NBI heated discharges	10-35	passing D ions
(3,2) NTMs in NBI+ICRH heated discharges	10-35	trapped H and D ions
Fishbones	5-25	trapped D ions
Sawtooth	15-25 + crashes	trapped H and D ions
Sierpes	70-80	trapped D ions
TAEs	150-200	trapped H and D ions
ICRH Beat Waves	10-250	trapped H and D ions

Table 7.1: Main types of fast ion-MHD mode interactions observed in ASDEX Upgrade.

- Strong fluxes of lost fast ions have been observed in discharges due to externally imposed magnetic perturbations like ICRF beat waves. As expected from ICRH heated discharges, fast ion fluxes have been detected in the trapped orbit region of the particle phase space.
- The selective character of the MHD activities ejecting hydrogen and/or deuterium ions has been established, playing in this case the larger banana width of trapped deuterium ions the crucial role. Lost hydrogen ions have been identified only in the presence of TAE modes while deuterium ions can be ejected by a wide variety of MHD activities.
- Orbit stochasticity has been suggested to be a good candidate to explain the losses of fast ions in pure NBI heated discharges with NTM activity. Numerical simulations with the ORBIT code show the orbit stochasticity generated by the overlap in particle phase space of the magnetic perturbation island and the drift islands. According to this, a quadratic dependence of FIL on the NTM magnetic perturbation strength was found experimentally, confirming the diffusive character of this transport mechanism.
- The mechanisms responsible for FIL on trapped orbits due to interactions with TAEs have been well identified and described. Fast trapped ions leave the plasma due to a two-step process. Firstly, an outwards radial drift of the banana tips takes place during ICRH heating. At the maximal ICRH heating energies, the banana tips of trapped ions lie already in the area of influence of a global mode like the TAE. In this region a resonant interaction between the energetic ions and the magnetic perturbation leads to a loss of the trapped ions in a few banana orbits. The wave-particle resonance condition in the plasma frame has been studied using the HAGIS code, leading to a strong loss of particles which fulfill the condition $n \cdot f_{prec} \approx f_{MHD}$. Here, n is the toroidal mode number, f_{prec} , the precession frequency of the lost trapped ions and f_{MHD} the frequency of the MHD activity.

- A possible application of externally imposed magnetic perturbations like the, in frequency and power, controllable beat waves is to remove a particular fast ion population from a certain location in plasma or eventually even totally from plasma through resonant interactions. This technique could be applied for example to remove the Helium ashes from the plasma.

The results obtained during this thesis with the Fast Ion Loss Detector for ASDEX Upgrade revealed the high diagnostic potential of this method. For major fusion devices like ITER, fast ion loss detectors will be of special interest since they can provide unique information of the plasma core through the large banana orbit widths. Lost ions on wide banana orbits carry with themselves information on plasma core, a region which is inaccessible up to now for other diagnostics.

Bibliography

- [1] J. A. Wesson. *Tokamaks*. Clarendon Press, Oxford, 1997.
- [2] H. P. Furth. *Nucl. Fusion*, 30:1799, 1990.
- [3] A. Werner, A. Weller. *Rev. Sci. Instrum.*, 72(1):780, 2001.
- [4] Manuel Garcia-Munoz. Modelling of fast ion losses in tokamaks. Technical report, Max-Planck-Institut fuer Plasmaphysik, 2003.
- [5] H.S. Bosch. *Diagnostik geladener Fusionreaktionprodukte in ASDEX*. PhD thesis, T.U.Muenchen, 1987.
- [6] G. Kallne, J. Gorini. *Physica Scripta*, 16, 1987.
- [7] W.W. Duong, H.H. Heidbrink. *Rev. of Sci. Instruments*, 61(10):3137, 1990.
- [8] S.J. Boivin, R.L. Zweben. *Nucl. Fusion*, 33, 1993.
- [9] G Bonheure. *Development of a fast ion detector for the textor-94 tokamak and application to the spectroscopy of 3 MeV fusion protons*. PhD thesis, l'Universite de Mons-Hainaut, March 2000.
- [10] A. Kallenbach. *Plasma Phys. Control. Fusion*, 47:207, 2005.
- [11] P. Lauber. *Linear Gyrokinetic Description of Fast Particle Effects on the MHD Stability in Tokamaks*. PhD thesis, Technische Universitat Munchen, 2003.
- [12] Z. Chang. *Phys. Rev. Lett.*, 76:1071, 1996.
- [13] T. Kondo. *Nucl. Fusion*, 40:1575, 2000.
- [14] S.J. Zweben. *Nucl. Fusion*, 39:1097, 1999.
- [15] S.J. Zweben. *Nucl. Fusion*, 40:91, 2000.
- [16] S.J. Zweben. *Nucl. Fusion*, 35:893, 1995.
- [17] R.J. Goldston. *Phys. Rev. Lett.*, 47:647, 1981.

- [18] T. Kurki-Suonio. *Private Communication*.
- [19] W.W. Duong, H.H. Heidbrink. *Nucl. Fusion*, 33(2):211, 1993.
- [20] D.S. Darrow. *Plasma Physics*, 16C, 1992.
- [21] P. H. Rosenbluth, M. N. Rutherford. *Phys. Rev. Lett.*, 34:1428, 1975.
- [22] D.J. Sigmar. *Phys. Fluids B*, 4(6):1506, 1992.
- [23] W.W. Duong, H.H. Heidbrink. *Nucl. Fusion*, 33(5):749, 1993.
- [24] K.L. Wong. *Phys. Rev. Lett.*, 66:1874, 1991.
- [25] W.W. Heidbrink. *Nucl. Fusion*, 31:1635, 1991.
- [26] R.B. White. *Phys. Plasmas*, 1995.
- [27] R.B. White. *Phys. Fluids*, 26(10):2958, 1983.
- [28] H.E. Mynick. *Phys. Fluids B*, 5:2460, 1993.
- [29] E.M. Carolipio. *Nucl. Fusion*, 42:853, 2002.
- [30] D.S. Darrow. *Nucl. Fusion*, 36:1, 1996.
- [31] Y. Ikeda. *Nucl. Fusion*, 36:759, 1996.
- [32] K. H. Finken. *Phys. Rev. Lett.*, 73:436, 1994.
- [33] A. Peeters. *High power RF heating and nonthermal distributions in tokamak plasmas*. PhD thesis, Technische Universiteit Eindhoven, 1994.
- [34] K. McGuire. *Phys. Rev. Lett.*, 50:891, 1983.
- [35] S. Gunter. *Nucl. Fusion*, 39:1535, 1999.
- [36] T. Kass. *Nucl. Fusion*, 38:807, 1998.
- [37] L. Chen. *Phys. Rev. Lett.*, 52:1122, 1984.
- [38] B. Coppi. *Phys. Rev. Lett.*, 57:2272, 1986.
- [39] S.-D. Pinches. *Nonlinear Interaction of Fast Particles with Alfvén Waves in Tokamaks*. PhD thesis, University of Nottingham, 1996.
- [40] C.Z. Cheng. *Phys. Fluids*, 29:3695, 1986.
- [41] G. Y. Fu and J. W. Van Dam. *Phys. Fluids B*, 10:1949, 1989.
- [42] H. Zohm. *Phys. Plasmas*, 41(2):197–202, 2001.

- [43] F. Wagner. *Phys. Rev. Lett.*, 49(19):1408–1412, 1982.
- [44] Keilhacker et al. *Plasma Phys. Control. Fusion*, 26, 1984.
- [45] W. Suttrop. *Plasma Phys. Control. Fusion*, 42, 2000.
- [46] H. Reimerdes. *Europhysics Conference Abstracts, Proc. 24 EPS Conf. on Controlled Fusion and Plasma Physics*, 21A:335, 1997.
- [47] W. Suttrop. *Plasma Phys. Control. Fusion*, 38:1407, 1996.
- [48] K. Nagashima. *Nucl. Fusion*, 36:335, 1996.
- [49] H.E. Mynick. *Phys. Fluids B*, 5:1471, 1993.
- [50] D.S. Darrow. *Rev. Sci. Instrum.*, 66:476, 1995.
- [51] S. Baeumel. *Rev. Sci. Instrum.*, 75:3563, 2004.
- [52] C. Gourdon. *Programme optimise de calculs numeriques dans les configurations magnetiques*. Centre d’etudes nucleaires de Fontenay aux Roses, 1970.
- [53] D. Spemann. PhD thesis, Universitaet Leipzig, 1998.
- [54] A. S. Marfunin. *Spectroscopy, Luminescence, and Radiation Centers in Minerals*. Springer, Berlin, 1979.
- [55] S. Yang. *Appl. Phys. Lett.*, 72:158, 1998.
- [56] M. Moszinski. *Nuc. Instrum. and Meth. A*, 404:157–165, 1997.
- [57] K.J. McCarthy. *J. Nucl. Mater.*, 340:291–298, 2005.
- [58] K. Kajiwara. *J. Vac. Sci. Technol. B*, 21:1622, 2000.
- [59] J. M. Ziegler. <http://www.srim.org/>.
- [60] J. Garcia-Lopez. *Nuc. Instrum. and Meth. B*, 161-163:1137, 2000.
- [61] K.J. McCarthy. *J. Nucl. Mater.*, 321:78, 2003.
- [62] G. G. Lister. A fully 3-d neutral beam injection code using monte carlo methods. Technical report, Max-Planck-Institut Fuer Plasmaphysik, 1985.
- [63] M. Brambilla. *Plasma Phys. Control. Fusion*, 41:1, 1999.
- [64] F. Porcelli. *Plasma Phys. Control. Fusion*, 38:2163, 1996.
- [65] C. P. Perez. *Plasma Phys. Control. Fusion*, 46:61, 2004.
- [66] A. Fasoli. *Nucl. Fusion*, 36:258, 1996.

- [67] A. Herrmann. *J. Nucl. Mater.*, 337:697–701, 2005.
- [68] T. Eich. *Phys. Rev. Lett.*, 91(19), 2003.
- [69] W.W. Heidbrink. *Nucl. Fusion*, 34:535, 1994.
- [70] W.W. Heidbrink. *Nucl. Fusion*, 40:935, 2000.
- [71] D.C. Pritchard. *Phys. Plasmas*, 4(1):162, 1997.
- [72] R.B. White. *Phys. Fluids*, 27:2455, 1984.
- [73] P. Martin. *Private Communication*.
- [74] S.-D. Pinches. Observation and modeling of fast ion loss. *9th IAEA Technical Meeting on Energetic Particles, Japan, 2005*.
- [75] D.S. Darrow. *Nucl. Fusion*, 37:939, 1997.
- [76] E.J. Strait. *Nucl. Fusion*, 33:1849, 1993.
- [77] S. Bernabei. *Nucl. Fusion*, 41:513, 2001.
- [78] V. Igochine. *Private Communication*.

Acknowledgments

In the three years of this research work, I benefited from the knowledge, encouragement and support of several people. At this stage, I would like to express my gratitude.

- First of all, I would like to thank **Prof. Dr. H. Zohm**, Head of the Experimental Division II. He gave me the opportunity to perform this challenging work under his supervision. I thank him for the consistent support allowing me the opportunity to find my own preferences and priorities.
- I do not have words to express my gratitude to **Dr. H.-U. Fahrbach**. I want to thank him for the outstanding support of my work, which would not have been possible without his personal and professional advice. He has invested a tremendous amount of time in introducing me into the fascinating world of experimental physics. I am very grateful to him for helping me to solve my daily problems.
- I am especially grateful to **Dr. J. Neuhauser** for the interest he always showed not only in my work but also on a personal level. I want to thank him for proofreading all my texts and encouraging me with his widespread knowledge in physics.
- I want to thank the *Fast Particle Hunter Team*, especially **Prof. Dr. P. Martin** and **Prof. Dr. S. Günter** for our fruitful discussions. Their enthusiasm for fast particle physics was always a motivation for me. I am very grateful to **Prof. Dr. P. Martin** for the ORBIT code simulations.
- I want to thank **Dr. M. Maraschek** for his permanent support on MHD perturbation physics as well as on programming.
- I am thankful to **Dr. M. Brambilla** and **Dr. R. Bilato** for introducing me into the amazing world of the ICRH and for providing ICRH fast particle distributions.
- I thank **Dr. A. Bergmann** for his advices and help to run the HAGIS code.
- I thank **Dr. A. Stäbler** for running the FAFNER code to calculate NBI fast particle distributions.
- I want to thank **Dr. V. Rohde** for his practical support on the mid plane manipulator.

- I would like to thank **H. Scholz**, **P. Leitenstern** and **J. Banhierl** for their unlimited patience, work on technical equipment and the practical support on the construction of the diagnostic.
- I thank **J. Harhausen** for his help with IDL programming.
- I want to thank **Dr. J. Schirmer** for correcting my english by proofreading all my texts.
- I am grateful to my room colleagues, **C. Tröster**, **L. Urso**, **E. Quigley** and **A. Schmidt** as well as to our neighbors, **K. Sassenberg** and **A. Flaws** for the interesting discussions and the positive atmosphere.
- Thanks a lot to **Dr. T. Pütterich** for the support on our challenging Task as Ph.D. representative.
- This thesis would surely not have been possible without the entire **ASDEX Upgrade Team**. I benefited greatly from the numerous colleagues and friends which make up this team.
- I want to thank **Dr. B. Zurro**, **Dr. J. García Lopez** and **D. Jimenez Rey** for making possible the experiments at the CNA (Centro Nacional de Aceleradores) in Spain.
- I am very grateful to **Dr. W. Parak** for his professional advice as well as for correcting my English.
- Thanks a lot to the spanish connection, **Pablo**, **Almu**, **Maite**, **Eric**, **Marta...** for their supporting friendship during these years.
- I would like to thank specially **María de los Ángeles** for her support, loving patience on the telephone and for keeping my spirits up.
- I am incredibly fortunate to have such a supportive family. I would like to thank my **father** and **María Jesus** for making possible my physics studies and therefore this work. I also thank my **mother** for her calls, which made me feel at home and **J.J.** for his reports. Here, I would like to thank my sister **Paloma** for her support and interesting stories.